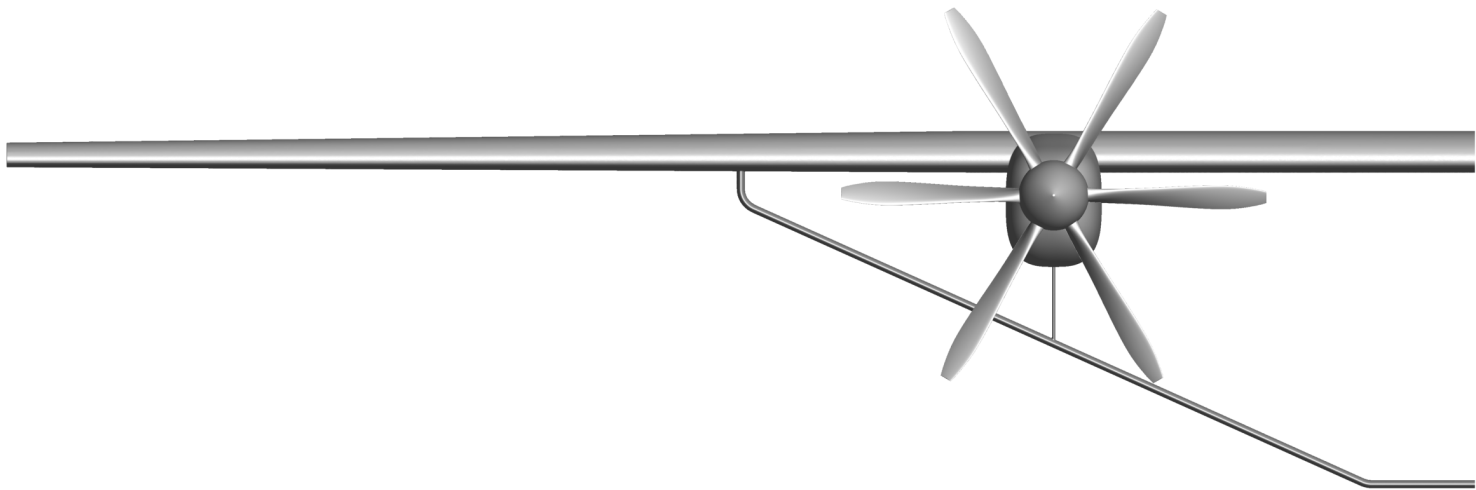


# Aerodynamic Analysis of a Propeller-Powered Strut-Braced Wing

Egon E. A. Beyne

Technische Universiteit Delft





# AERODYNAMIC ANALYSIS OF A PROPELLER-POWERED STRUT-BRACED WING

by

**Egon E. A. Beyne**

to obtain the degree of

**Master of Science**

in Aerospace Engineering

at the Delft University of Technology,

to be defended publicly on 19 December 2023 at 13:00.

Supervisors:	dr. ir. T. Sinnige	
	Prof. dr. ir. L.L.M. Veldhuis	
Thesis committee:	dr. ir. F. Oliviero	Chair of the Committee
	dr. ir. T. Sinnige	Supervisor
	Prof. dr. ir. L.L.M. Veldhuis	Supervisor
	dr. ir. A.H. van Zuijlen	Committee Member

An electronic version of this thesis is available at <http://repository.tudelft.nl/>.



# PREFACE

This thesis report is the culmination of 5 years worth of education in Aerospace Engineering. While challenging at times, it has been a very rewarding and interesting period. I have gained a lot of knowledge, and learned many new skills, both technical and personal. I will remember this period of my life with fondness.

While this report bears my name, it would not have been possible without the help of many other people. First of all, I would like to express my gratitude towards my supervisors, professor Veldhuis and dr. Sinnige, for their guidance and feedback during the project. Their insights and expertise have certainly helped raise the level of this thesis. I would also like to thank my parents for their support throughout my studies, and for proofreading my work. Finally, I would like to thank my friends from room NB1.09. Our discussions on thesis-related and other topics have been very helpful.

*Egon E. A. Beyne  
Delft, December 2023*



# SUMMARY

The aerodynamic performance of a regional, propeller-powered strut-braced wing is investigated. The main wing planform and operating conditions are based on an ATR72, to which a strut and jury strut are added. The research focuses on the different drag components in cruise. The first research objective is to quantify the effect the different wing components have on the change in induced drag caused by the propeller. The second objective deals with viscous effects, such as separation and friction. At the strut-wing and strut-jury strut junctions, it is tested whether the propeller affects the size and location of any separated regions. In addition, the influence of the propeller on the skin friction drag is quantified. The final objective deals with interference and compressibility. The close proximity of the strut, jury strut and wing, combined with the increased slipstream velocity of the propeller, and the change in angle of attack caused by swirl recovery might lead to high supersonic velocities. The regions with the highest supersonic velocities are localised, and it is verified whether any supersonic flow exists.

Induced drag is calculated with a panel method (Flightstream), which allows simulating different configurations in a relatively short time. By simulating different combinations of wing elements (with and without strut, jury strut and propeller) it is possible to isolate their contributions. The research objectives about viscous effects and interference were investigated using unsteady RANS. The CFD simulation were also used to validate the panel method. In general, it agreed well with CFD. Some discrepancies were caused by the absence of vortex dissipation and an offset in the pressure distribution inside the propeller slipstream.

The propeller reduced induced drag significantly, around 58% for all configurations. The main strut had the largest effect. Both the strut itself and interference of it with the wing lead to an additional reduction of 1% in induced drag. The jury strut had limited effect. Under the influence of a propeller, it had a small induced thrust component. Interference with the main wing cancelled out this benefit. These results were obtained using unoptimised loading distributions, optimising these would increase the gains for both the conventional and strut-braced wings.

The strut-wing junction only showed separation at the strut leading edge. The local flow behaviour was not influenced by the propeller. The strut-jury strut junction also exhibited leading edge separation, in addition to corner separation at the trailing edge of the jury strut, and separation at the trailing edge of the main strut. The size of the corner separation reduced under the influence of the propeller, by favorably changing the pressure gradient on the jury strut. The net effect of the propeller on the separated region at the trailing edge of the strut was to move it inboard, by increasing the pressure gradient there, and moving the location of the horse-shoe vortex system inward. Friction drag increased by roughly 3%, insignificant compared to the reduction in induced drag.

Finally, the region most sensitive to high supersonic velocities was the strut-jury strut junction. The closely spaced elements, combined with the higher slipstream velocity and increased angle of attack lead to a small supersonic pocket. Due to its limited size, it is expected that using a slightly different airfoil for the jury strut can already eliminate it.

While some attention needs to be paid to junction flows and interference effects, this work has shown the advantage of a propeller-powered strut-braced wing for regional aviation, compared to conventional aircraft.



# CONTENTS

<b>Nomenclature</b>	<b>ix</b>
<b>1 Introduction</b>	<b>1</b>
<b>2 Relevant Aerodynamic Phenomena</b>	<b>3</b>
2.1 Strut-braced wing aerodynamics . . . . .	3
2.2 Propeller-wing aerodynamics . . . . .	5
<b>3 Research Outline</b>	<b>11</b>
3.1 Research Questions . . . . .	11
3.2 Research Strategy . . . . .	11
3.3 Geometry . . . . .	13
<b>4 Computational Setup</b>	<b>19</b>
4.1 Methodology . . . . .	19
4.2 Initial validation . . . . .	23
4.3 Strut-Braced Wing . . . . .	33
<b>5 Validation</b>	<b>39</b>
5.1 Propeller modelling . . . . .	39
5.2 Initial validation . . . . .	41
5.3 Strut-Braced Wing . . . . .	46
<b>6 Results</b>	<b>51</b>
6.1 Induced drag . . . . .	51
6.2 Viscous Effects . . . . .	57
6.3 Compressible Effects . . . . .	62
<b>7 Recommendations and Conclusion</b>	<b>65</b>
7.1 Recommendations . . . . .	65
7.2 Conclusion . . . . .	65



# NOMENCLATURE

## SYMBOLS

Symbol	Definition
$A$	Aspect Ratio
$a$	Increase in velocity behind the propeller in actuator disk theory
$B$	Number of Propeller Blades
$b$	Wing Span
$\bar{c}$	Mean Aerodynamic Chord
$C_D$	Drag Coefficient
$c_f$	Skin Friction Coefficient
$C_L$	Lift Coefficient
$C_p$	Pressure Coefficient $\left(\frac{p-p_\infty}{\frac{1}{2}\rho V_\infty^2}\right)$
$C_Q$	Propeller Power Coefficient
$c_Q$	Local Torque coefficient $\left(\frac{BQ_{loc}}{\frac{1}{2}\rho n^2 D^4}\right)$
$C_r$	Root Chord
$C_T$	Thrust Coefficient $\left(\frac{T}{\rho n^2 D^4}\right)$
$c_T$	Local Thrust Coefficient $\left(\frac{BT_{loc}}{\frac{1}{2}\rho n^2 D^3}\right)$
$c$	Chord Length
$h_{js}$	Jury Strut Height
$h_s$	Strut Height
$J$	Advance Ratio
$l_p$	Pylon length
$M$	Mach Number
$n$	Rotational Speed
$p$	Pressure/Observed Order of Accuracy
$Q_{loc}$	Local Torque ( $N$ )
$Re$	Reynolds Number
$S$	Reference Area
$S_{sl}$	Wetted Area inside the propeller slipstream
$S_{nsl}$	Wetted Area outside the propeller slipstream
$S_w$	Wetted Area
$r$	Radial position along the propeller blade
$T$	Temperature
$T$	Thrust
$T_{loc}$	Local Thrust ( $N/M$ )
$U_\phi$	Discretisation Error
$V_\infty$	Freestream Velocity
$V_{in}$	Local Inflow Velocity
$w$	Downwash Velocity
$x_s$	Wing-Strut Attachment x-position
$y_k$	Wing Kink Position
$y_s$	Wing-Strut Attachment y-position
$y^+$	Dimensionless Wall Distance
$\alpha$	Angle of Attack

---

Symbol	Definition
$\Gamma$	Circulation
$\beta$	Propeller pitch angle
$\eta$	Normalised y-position along wing span ( $2 \cdot y/b$ )
$\lambda$	Taper Ratio
$\rho$	Density
$\tau_w$	Skin Shear Stress

---

# 1

## INTRODUCTION

In the quest for more sustainable aviation, different pathways towards the ultimate goal of carbon-free air travel are studied. Changing the way aircraft are operated can yield reductions in emissions and operating cost. Flying lower and slower reduces wave and friction drag, at the cost of longer travel times. While the lower speed may be prohibitive on long-haul flights, its effect on low distance flying is less. Eurocontrol found that 25% of all aviation-attributable CO<sub>2</sub> in Europe is emitted by flights under 1500 km [16], illustrating the possible savings that can be made.

While wave and friction drag decrease at lower speeds, induced drag grows. Increasing the aspect ratio is a common way to counter this increase. However, it comes at the cost of a heavier wing, which in turn requires more lift and may offset the advantage of the increased aspect ratio. A solution for this is the strut-braced wing (SBW). Its high aspect ratio reduces the induced drag, while a supporting strut keeps the weight within bounds.

The concept of a strut-braced wing is not new. The first generations of aircraft often required multiple external structural members to ensure sufficient strength of the wing. Advances in aircraft structures, such as the use of metals and load-carrying skins, soon made the use of struts obsolete. Eliminating them meant a reduction in interference and parasitic drag. However, these are part of the profile drag, which is typically only half of the total drag in cruise. The other component, induced drag can be reduced by employing high aspect ratio wings. As a method to keep the weight down and still use a high aspect ratio, the strut made a comeback in the 1950's. French aircraft manufacturer Hurel-Dubois produced several SBW aircraft. They proved the practicality of the concept with the HD.10 research aircraft, results of which were applied in the design of the HD.31. This aircraft had a wing with an aspect ratio of 20, and was used as an airliner and for aerial photography [46]. However, the aircraft was not as successful as anticipated, possibly because of its disadvantage in cruising speed compared to the new jet airliners of that time. More recently, the strut-braced wing has received renewed attention; rising fuel costs and the need to reduce emissions in aviation made the aircraft interesting again.

Figure 1.1 shows the geometry of a propeller-powered strut-braced wing, annotated are the different components. Apart from the main strut, it also employs a so-called jury strut. This can be employed to increase the buckling resistance of the strut. Because of its slender shape, buckling is often the main sizing criterion for the structure of the strut [34]. A pylon is employed to separate the wing and main strut, to reduce interference effects.

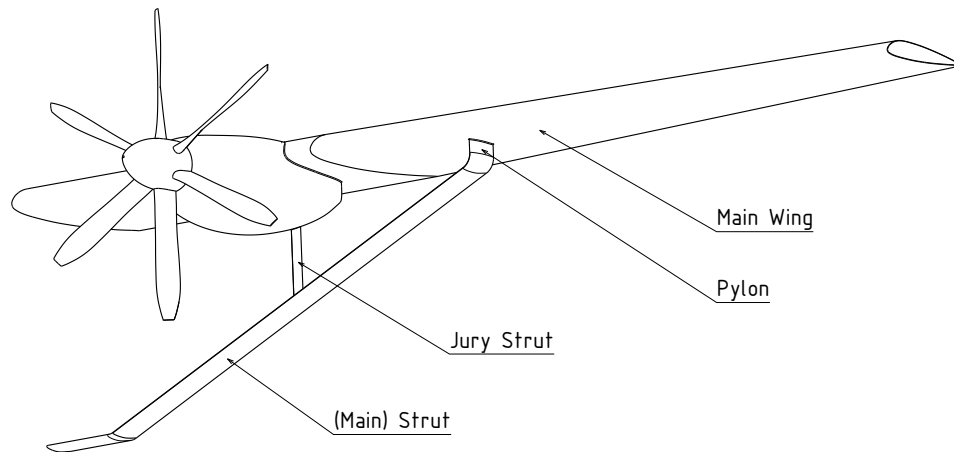


Figure 1.1: Definition of wing components of a strut-braced wing

SBW concepts have been researched by multiple institutions. The most well-known is SUGAR Volt, designed by a team led by Boeing. Reductions in fuel burn were estimated at 54%, but this includes gains from other new technologies as well. The most recent iterations of the concept use turbofan engines, and cruises at Mach 0.8. In January 2023, NASA awarded Boeing nearly half a billion dollar to build an SBW technology demonstrator, designated the X-66. Another study, performed by Gundlach et al. [19] studied an SBW aircraft with a slightly higher cruise speed of Mach 0.85. Compared to a generic cantilever wing aircraft, this yielded more modest reductions in fuel burn of around 14%. These may be attributable to the higher cruise speed, where induced drag plays a smaller role, and the lower aspect ratio of the wing (12.17 instead of the 19.5 employed by SUGAR Volt). Ma et al. [29] compared the application of a strut-braced wing at different market segments. They found that the strut-braced wing was more efficient than conventional aircraft on all market segments. On a short range mission, 28% of fuel weight was saved by using a propeller-powered SBW, compared to the ATR 72-600.

Aside from Ma et al., most research focuses on transonic SBW concepts. At this speed regime, wave and friction drag are the dominant drag sources. The contribution of induced drag is higher when flying slower. A high aspect ratio, strut-braced wing might therefore be more beneficial at lower speeds. In this report, a regional propeller-powered strut-braced wing is researched. More specifically, the effects of the propeller on the cruise performance of the aircraft are analysed. This is done by looking at the different components of the drag. For the induced drag, the contributions of the strut and jury strut on the change in induced drag caused by the propeller are quantified. Viscous drag is looked at in a more qualitative way. Regions of separated flow are identified, and it is checked whether they change under the influence of the propeller. In addition, the change in friction due to the propeller is treated. Finally, it is verified whether any regions of supersonic flow exist due to interference or propeller effects. Two methods are used for the analysis. Induced drag is obtained using a panel method, which can give results in a short time frame. Viscous and compressible effects are simulated using an unsteady Reynolds-Averaged Navier Stokes (RANS) solver.

The report starts with a short overview of relevant theory in [chapter 2](#). This summarises a literature review on topics relevant for strut-braced wing aerodynamics. It includes a treatment of aerodynamic mechanisms, with and without propeller. Next, the research questions and approach are presented in [chapter 3](#), together with the geometry of the different configurations used. The settings used for the flow solvers and meshing are given in [chapter 4](#). Additionally, this chapter contains mesh convergence studies to quantify the spatial discretisation errors. Validation of the panel method used for induced drag computations follows in [chapter 5](#). Finally, the research questions are answered in [chapter 6](#), which shows the results of the research. The findings are summarised in [chapter 7](#), and recommendations for future work are given.

# 2

## RELEVANT AERODYNAMIC PHENOMENA

Regional, propeller-powered strut-braced wings have received relatively little attention in literature. Some design studies have been done, but none of them go deeply into the aerodynamics. In this chapter, the result of a literature study into topics relevant for the aerodynamics and analysis of a propeller-powered strut-braced wing aircraft are presented. [section 2.1](#) is about the unpowered aircraft, focusing on induced and interference drag. This is followed by a treatment of propeller-wing aerodynamics in [section 2.2](#). While virtually all literature researched conventional wings, some of the concepts are translated to SBW aircraft.

### 2.1. STRUT-BRACED WING AERODYNAMICS

A short review of aerodynamic phenomena relevant for a strut-brace wing is given in this section. Induced drag is where the main advantage of a strut-braced wing originates from, it is treated in [subsection 2.1.1](#). It elaborates on the induced drag due to the non-planar wing planform of a SBW. The advantage of high aspect ratio wings is well-known, and is not explained here. Interference between the different wing elements is expected to play an important role. Most literature specific to strut-braced wings target the transonic speed regime, where interference largely manifests itself in the form of shockwaves. This is not directly of interest for a regional strut-braced wing. Instead, [subsection 2.1.2](#) focuses on phenomena that are also present at lower speed, such as junction flows.

#### 2.1.1. INDUCED DRAG

The most evident benefit in terms of induced drag for the strut-braced wing is the increased aspect ratio that is possible. Indeed, wings with aspect ratios around 20 are being studied [\[39\]](#), potentially leading to large savings in induced drag. The effect of aspect ratio on induced drag is well-documented, and will not be treated here.

A more interesting aspect of the induced drag of strut-braced wings, is the non-planarity. In most SBW concepts, the strut is a lifting surface as well. According to Kroo [\[26\]](#), non-planar wings have the potential of an increased span efficiency factor, given an optimal loading distribution. This is supported by a paper of Takahashi and Donogan [\[50\]](#). They studied different non-planar wing concepts more in depth using an inviscid numerical model. One of the concepts evaluated is an SBW. They found that an SBW can have a span efficiency between 1.02 and 1.04, depending on the ratio between strut height and wing span, where a larger strut height was more beneficial.

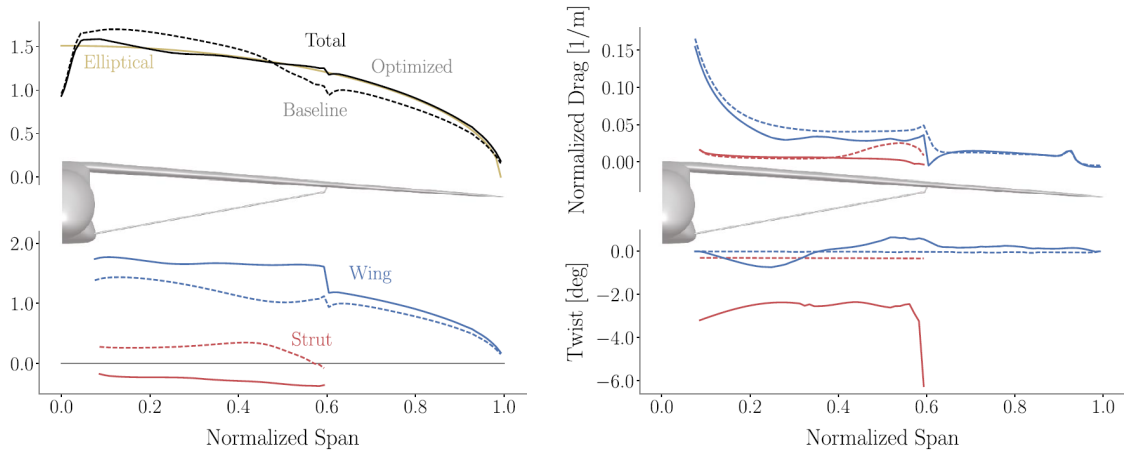


Figure 2.1: Spanwise loading and drag of the baseline and optimised SBW configurations by Secco and Martins [39].

When considering the most efficient loading distribution of a strut-braced wing, there is no unique solution. All closed elements have an optimal loading distribution, to which a vortex ring of constant, arbitrary strength can be added [11] [26]. This opens possibilities, especially for the low speed regime. The loading of the strut and main wing can be tuned such that they both achieve their maximum lift at the same moment, increasing the usable lift of the SBW. However, in their optimisation of an SBW, Secco and Martins [39] found that the optimal loading of the strut with respect to drag is negative. This is possibly to reduce superelevations on the upper side of the strut. The lift distribution is shown in Figure 2.1. It can be seen that the negative lift of the strut is compensated by an increased lift of the inboard section of the main wing. Effectively, the optimiser added a vortex ring to the closed inboard section. Note how the total lift distribution closely follows the elliptical. In their research for SUGAR Volt, Boeing came up with a similar lift distribution, although the strut provides negative lift only near the junction [12]. When jury struts are added in addition to the main strut, they are ideally unloaded, or at least have a constant loading [11].

### 2.1.2. INTERFERENCE DRAG

Interference drag is defined as the difference between the drag two individual bodies experience and the drag felt when adding these two bodies together. When connecting two surfaces together, their pressure fields and boundary layers will interact with each other. These junction flows have been studied in the past, mostly at the wing-fuselage connection. This location is also of interest for a strut-braced wing, but there are some additional regions where junction flow may play a role. These could be all the connection points between wing, strut, jury strut and fuselage. The junction flows between lifting elements of a strut-braced wing may be more complex than those found in literature, as the intersections deal with multiple lifting elements. Still, fuselage-wing junction flows may qualitatively be similar. Some studies of these flows are presented here.

Near the leading edge of the root airfoil, the stagnation point is present. Around this point, the flow decelerates from free-stream velocity to virtually standstill. Accordingly, the static pressure will also increase. The adverse pressure gradient associated with this can lead to separation of the fuselage boundary layer around the leading edge region of the root. Maughmer et al. [30] experimentally observed this effect on a glider model at relatively low Reynolds numbers (250 000 - 400 000). They noted that the separated boundary layer consequently formed a horseshoe vortex wrapping around the complete root of the wing, leading to increased vortex drag. An illustration of this flow is provided in Figure 2.2. The same phenomenon is observed at higher, more representative Reynolds numbers. Kegerise et al. [24] experimentally investigated the junction flow between a wing and fuselage at a Reynolds number of 2.4 million. They also observed separation of the fuselage boundary layer near the leading edge of the root, as well as the horseshoe vortex. While the Reynolds number is not yet representative of full flight, it approaches the Reynolds number of a typical turboprop transport of around 15 million.

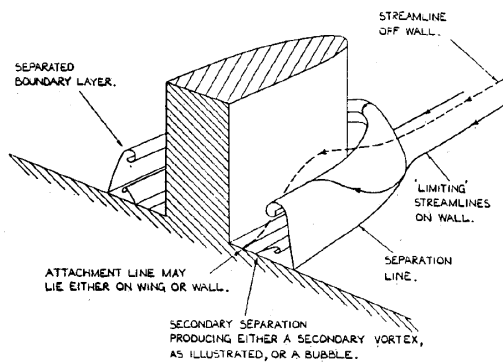


Figure 2.2: Typical flow near the leading edge of a wing-fuselage junction. Image taken from [44].



Figure 2.3: Separation near the trailing edge of a wing root, visualised by oil. Image taken from [24].

Another critical region is the rear portion of the suction side of the intersecting element. Here the flow decelerates from its maximum velocity at the suction peak, back to something near freestream velocity. This can lead to separation of the merged boundary layers of the fuselage and wing. Such a portion of separated flow is shown in [Figure 2.3](#). The vortex originating from the separation near the leading edge may complicate the flow field further. Gand et al. [17] studied the unsteady behaviour of this vortex, and found that its position oscillated with a Strouhal number of around 0.2. The boundary layer thickness at 0.5 chord lengths ahead of the wing root leading edge was used as length scale. This could introduce unsteady loading, and complicates the analysis of fuselage-wing junction flow. It could also prevent separation near the trailing edge. According to Barber [5], the drag penalty associated with a junction flow depends mainly on the thickness of the incoming boundary layer. A thick boundary layer is more prone to separating, and will thus lead to a large and relatively strong horseshoe vortex. Near the trailing edge of the intersecting element, the vortex increases the momentum of the flow, and prevents or reduces separation. When the incoming boundary layer is thin, the horseshoe vortex may not be strong enough to prevent corner separation. For strut-strut and strut-wing intersections, the incoming boundary layers will be relatively thin. Hence, it is expected that corner separation will be observed.

The angle between two intersecting elements can have a large effect on corner flows. Tétrault et al. [51] looked at the effect of strut angle and thickness ratio on interference between a surface and a strut, using a RANS simulation. They found that an angle of 90 degrees is most optimal with respect to interference drag. At this angle, a thicker strut resulted in negative interference drag, because the wall boundary layer attenuates the strength of a shockwave present on the strut. At smaller angles interference drag rises, an effect aggravated by thicker struts. Furthermore, it was noted that increasing the Reynolds number reduced interference drag in all cases. An important limitation of this study is that only the drag of the strut was considered. Following [30] and [58], a thick strut at 90 degrees may well cause the boundary layer of the surface to separate, cancelling the favourable interference drag found by the study. Practically, ensuring a 90 degrees angle between the different wing elements of a strut-braced wing is done by adding a pylon between the strut and wing. This has the additional benefit of increasing the area of the channel between the two elements. According to Ko et al. [25], the flow in this region behaves almost two dimensional. If the area between wing and strut becomes too shallow, choked flow and shockwaves may result.

## 2.2. PROPELLER-WING AERODYNAMICS

The main research area of this report is propeller integration. It is hypothesised that gains in drag due to aero-propulsive interactions in strut-braced wings exceed those of conventional wings, due to the possibility of swirl recovery by the additional wing elements. However, this is a topic that has not received any attention in literature. The following section therefore mostly draws on literature for conventional propeller-wing combinations, and tries to extrapolate results to a strut-braced wing. Induced drag reduction are possible due to swirl recovery and slipstream contraction. These are treated in [subsection 2.2.1](#). In addition, propeller-induced changes in viscous drag is treated in [subsection 2.2.2](#). Finally, compressibility is treated in [subsection 2.2.3](#). The limited literature available about this topic focused on transonic propeller-powered aircraft.

### 2.2.1. INDUCED DRAG

The integration of a tractor propeller can reduce the induced drag of a wing significantly. The decrease in induced drag can be attributed to the swirl velocity induced by the propeller. These locally alter the angle of attack of the wing. Since lift is defined perpendicular to the incoming flow, a change in angle of attack induces a component of the lift in freestream direction. This leads to a thrust component behind the upgoing blade, but increases drag behind the downgoing blade. If the upgoing blade influences a wing portion with a higher local lift than the downgoing blade, the net effect is a thrust component. It is for this reason that inboard up rotation is more beneficial for the performance of a propeller-wing system [55]. The optimal lift distribution for a propeller-wing combination exploits this effect, by increasing the local lift behind the upgoing blade and vice versa for the downgoing blade. Witkowski et al. [60] found reductions of up to 60% in a combined numerical and experimental study. In a different experimental study at low Mach (0.1) and Reynolds number (470 000) Johnson et al. [22] achieved slightly lower reductions, of around 45%. The difference in drag reduction may be caused by the difference in configuration used. While both studies use a wing with a similar aspect ratio, [60] places the propeller more outboard on the wing which yields higher gains in drag, as explained later.

To achieve these gains, the optimal lift distribution differs significantly from the elliptical, as illustrated in Figure 2.4. This figure is the result of an optimisation with respect to total drag by Kroo [27]. While the optimal loading distribution of a wing and tractor propeller is very different from the elliptical, it is often created almost automatically by the swirl and axial velocity in the propeller slipstream. Indeed, the lift distributions behind an optimised and non-optimised wing are very similar, as demonstrated by Chauhan and Martins [9]. While they confirm the savings in induced drag by the integration of a tractor propeller, they found that a wing optimised with or without propeller yield about the same gains. The main variables affecting the induced drag were the propeller rotational direction, and wing planform shape and twist. The wing configuration used has a low aspect ratio of 5.3. If the conclusion of the study holds for large aspect ratio, non-planar wings, it would mean their lift distribution could be optimised cheaply without considering the propeller.

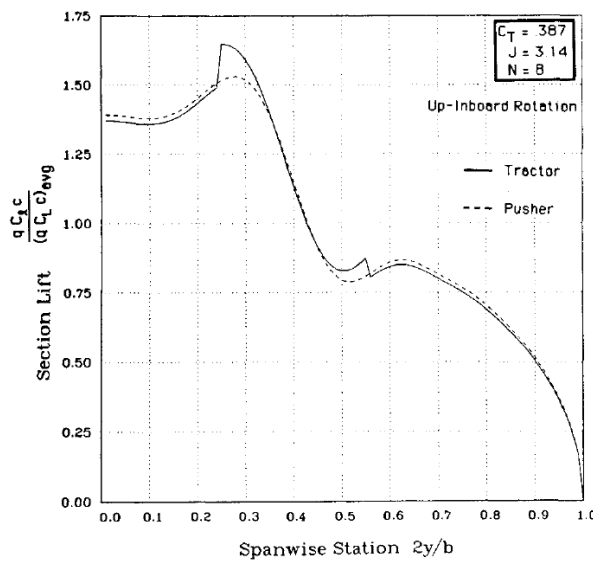


Figure 2.4: Lift distribution giving minimal drag when including a propeller. Image taken from [27]

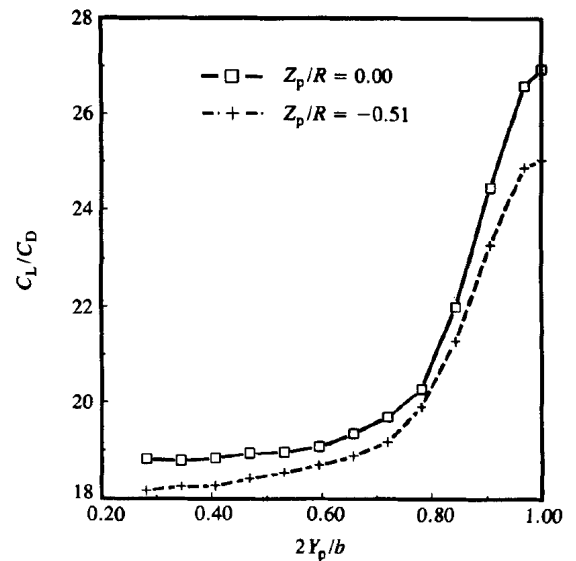


Figure 2.5: Effect of spanwise propeller position on L/D ratio. Image taken from [55]

As was mentioned earlier, savings in induced drag of the wing by a propeller mainly come from a difference in lift between the upgoing and downgoing blades. This can be achieved in a conventional wing by moving the propeller outboard, as there usually a large gradient in lift is observed. The extreme case of this is a wingtip propeller. Here only the slipstream from the upgoing blade washes over the wing, giving an increase in lift and a reduced induced drag not offset by the downgoing blade. The effect of this on lift-to-drag ratio estimated by Veldhuis [55] on an unoptimised low aspect ratio wing is shown in Figure 2.5.

**Propeller-strut interaction** Because of one-engine-inoperative controllability requirements, the engine is usually located close to the fuselage. In a strut-braced wing, this would be inboard of the strut-wing junction. As a consequence, the propeller is located above the strut. In terms of induced drag, two effects will have an influence. First, the strut will recover some of the propeller swirl. Even though the swirl components of the velocity are not perpendicular to the strut, they will likely still affect the loading distribution. Another effect is the slipstream contraction, which would put the strut under an increased angle of attack and tilt the lift vector forward [56]. The slipstream contraction affects the strut even if it is below the propeller slipstream. This is confirmed by Wang et al. [59], who tested the influence of a propeller on a wing at multiple positions. When placing the propeller over the wing, such that the slipstream does not wash over it, they found an increase in lift and a decrease in drag. The most beneficial position was with the propeller positioned somewhere along the wing chord, but a propeller in front and above the wing also led to a higher lift-to-drag ratio. Still, a vertical propeller position as close to the wing as possible seems to give the largest increase in L/D, see Figure 2.6. They attribute the gain in performance to the decrease in static pressure in front and increase behind the propeller disk, which respectively act on front facing and rear facing faces of the wing when the propeller is placed along the wing chord. However, this does not explain why a propeller in front of the wing also benefits the lift and drag. Instead, this may have been due to the slipstream contraction.

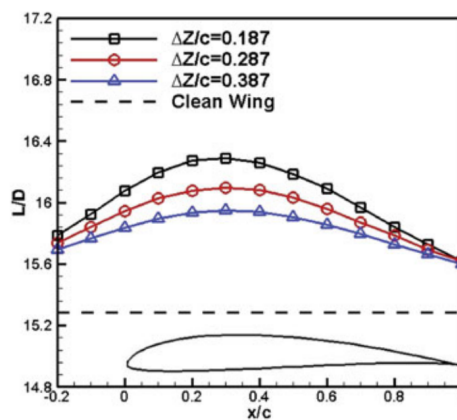


Figure 2.6: Effect of vertical and longitudinal propeller position on lift-to-drag ratio. The vertical position  $\Delta Z$  is the distance from the lowest part of the propeller disk to the chord of the airfoil. Image taken from Wang et al. [59].

Another consideration of strut-propeller interaction is that the strut will be immersed in a portion of the slipstream with a different axial velocity than the main wing. The axial velocity will reach a maximum around three quarters of the propeller radius. An increased slipstream velocity would favorably influence the lift of the wing but also increase drag [56].

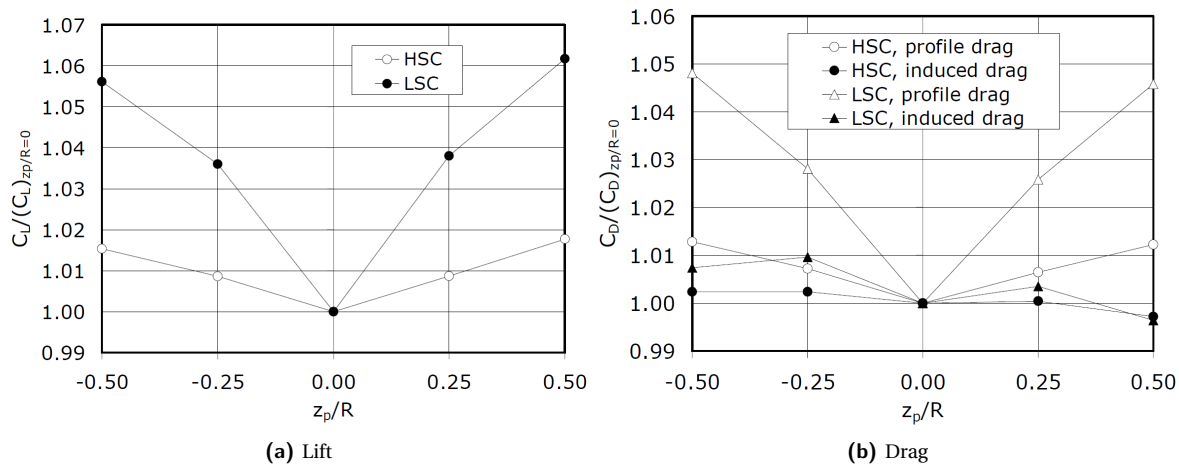


Figure 2.7: Effect of vertical propeller positioning on the drag and lift of a wing at high speed (HSC) and low speed (LSC). The low speed case has a lower advance ratio than the high speed case. Image taken from [56].

Figure 2.7 shows how the lift and drag of a wing change with respect to the vertical position of a propeller. Note that the change in drag mainly originates from the profile drag, due to the increased slipstream velocity. Furthermore, even though the local angle of attack increases when moving the propeller upward, the induced drag does as well. This may be because moving the propeller away from the wing or strut results in a component of the swirl velocity that is in the plane of the wing, which does not contribute to swirl recovery.

**Propeller-jury strut interaction** In some SBW configurations, a jury strut provides an additional connection point between the strut and the wing. Its function is to increase the buckling resistance of the main strut, which is its critical sizing criterion according to Park [34]. When ignoring the connection with the strut, they can be considered as swirl recovery vanes (SRV). In most studies, the swirl recovery vanes are considered as part of the propulsion system, and their effect on the performance of the aircraft is expressed in terms of propulsive efficiency. A design with multiple vanes can typically achieve increases in propeller efficiency of roughly 2% by reducing the kinetic swirl energy in the propeller wake by around 50% for an isolated propeller-SRV system [4] [57]. The presence of a wing is usually found to reduce the gains in efficiency, since the up- or downwash ahead or after the wing interacts with the SRV's, and the wing itself already recovers a large part of the swirl [57]. The first effect should not affect SBW's much, as the strut and pylon are located somewhere along the chord of the wing, where the down- or upwash is relatively small. The second effect might also have a limited influence, as the jury strut and pylon are usually at almost right angles with the wing, and should thus be influenced by different parts of the slipstream.

The length of the pylon or jurystrut may play a role in the effectiveness of it as swirl recovery device. Avallone et al. [4] investigated how the length of an SRV impacts the aerodynamic performance. They found that most of the thrust generated by the SRV comes from the blade wake, corresponding to the more central sections of it. The central part of a propeller blade is also the location where the swirl velocity reaches a maximum. However, the outward part of an SRV can get some additional thrust from the impingement of the blade tip vortex. It is unclear how this would translate to a strut-braced wing. Depending on the location of the jury strut and propeller, the propeller tip vortices may or may not interact with it.

Unlike most SRV systems, the jury strut or pylon consists only of 1 blade. This specific case was investigated by Li et al. [28]. They performed research into the interaction between propeller, wing and swirl recovery vanes. One of their findings is that when the SRV's are aligned with the plane of the wing, they will reduce the effectiveness of the wing to recover swirl. When placing the SRV in front of the wing (behind the upgoing blade), the downwash of the SRV will reduce the lift of the wing and increase its induced drag. This to the extent that the induced drag benefit of the SRV was cancelled out completely. When positioning the vane behind the wing (most effective behind the downgoing blade), the vane produces negative lift, forcing a higher lift coefficient of the main wing and consequently increasing induced drag. Still, the study concludes that positioning the SRV behind the wing gives the best performance in terms of induced drag and SRV thrust. However, when looking at Figure 2.8, it seems that moving the SRV more to the front may benefit the combination of induced drag and thrust of the wing and SRV system. In addition, the jury strut and wing will recover the components of the slipstream swirl perpendicular to their plane, and will thus not compete. Finally, it is noted that Li et al. [28] is the sole research towards single swirl recovery vanes considering the influence of the wing. More research into this topic would benefit the understanding of propeller-jury strut integration in the strut-braced wing.

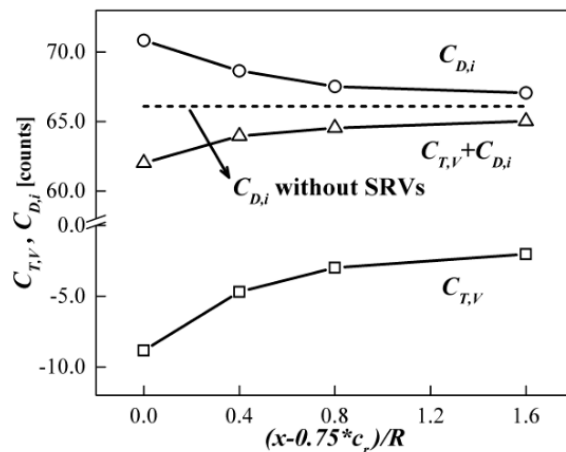


Figure 2.8: Effect of axial swirl recovery vane position on the induced drag of the wing and thrust produced by the SRV. Note that the position is defined relative to the trailing edge of the wing root. Image taken from Li et al. [28].

### 2.2.2. VISCOUS DRAG

A lot of effort is also put into reducing viscous drag of modern transport aircraft. The addition of a propeller may pose an additional challenge. The slipstream has been observed to move the transition point far upstream, increasing friction [8]. Miley et al. [31] performed flight tests using a GA-7 Cougar and wind tunnel tests on a NACA0012 wing section and propeller. The objective was to measure the effect of the propeller slipstream on the boundary layer. It was found that the propeller slipstream caused periodic transition of the boundary layer at the blade passage frequency. These were caused by the turbulence in the wake of the propeller blades. The periodically increased turbulence level in the external flow caused by the wake caused strips on the wing surface to transition as well. The length of these turbulent strip became longer as the laminar boundary layer stability reduced. Contrary to what could be expected based on the Reynolds number, this increases with aircraft speed. At high speed, the angle of attack is low, and a favorable pressure gradient is present. At low speed, the opposite is true, which causes the length of the turbulent strips to grow, up to the point where most of the wing boundary layer immersed in the slipstream becomes turbulent.

Another viscous effect comes from the propeller tip vortices. These are cut by the wing, such that the vortex core travels along the wing surface. The vortex core causes a low pressure region on the wing, while the vortex itself induces an increase in velocity on one side and a decrease on the other side. It is possible that either the pressure fluctuation due to the core, or the pressure gradient due to the induced velocity may cause the boundary layer to transition or separate. Although the specific cause is not mentioned, Johnston and Sullivan [23] observed a separation bubble preceding the vortex core on a wing surface. However, it seems that no fundamental research on boundary layer interaction with a perpendicular vortex has been performed.

The discussion above is mainly concerned with the nature of the boundary layer, which will to a large extent determine the friction coefficient. The earlier transition to a turbulent boundary layer will increase the friction. This is further aggravated by the velocity increase in the slipstream. To minimise this, the portion of the wing and strut immersed in the slipstream should be minimised. This would counter the benefits with respect to induced drag as well. As a compromise, the propeller could be placed such that only the regions where the slipstream benefits the induced drag are immersed. Based on the previous section, it is hypothesised that the region around the jury strut-wing junction yields the highest improvements.

### 2.2.3. COMPRESSIBLE EFFECTS

The increased velocity in the slipstream can give rise to additional wave drag. This was researched by Rizk [36] for a wing section immersed in a propeller slipstream at a freestream Mach number of 0.8. He found an increase in wave drag due to the axial and circumferential induced velocities of the propeller. The main effect of the swirl velocity is to alter the local angle of attack of the wing sections. This gave rise to increased superelevations on the suction side and decreased elevations on the pressure side behind the upgoing blade, the opposite happening at the downgoing blade. The axial induced velocity increases the Mach number over the entire submerged wing section. This led to an aft movement and subsequent increase in strength of the

shock wave on the upper surface behind both the upgoing and downgoing blades. On the lower surface, a new shock wave formed due to the increased superelevations of the swirl behind the downgoing blade. Behind the upgoing blade, this did not happen. The pressure distributions behind the up- and downgoing blades are shown in Figure 2.9. The work of Rizk was performed for a transonic aircraft already exhibiting shock waves. It is not clear how this would translate to a regional aircraft, flying at a little more than half the Mach number. No research into the effect of a propeller on compressibility of a regional aircraft was identified.

At the speed of a regional aircraft, no shock waves are expected in a conventional aircraft. For a strut-braced wing, there is the potential for more interference. If the propeller slipstream washes over the strut-wing junction, the magnitude of the superelevations could be aggravated by the channel flow effect described by [25]. This is a topic that may benefit from further research.

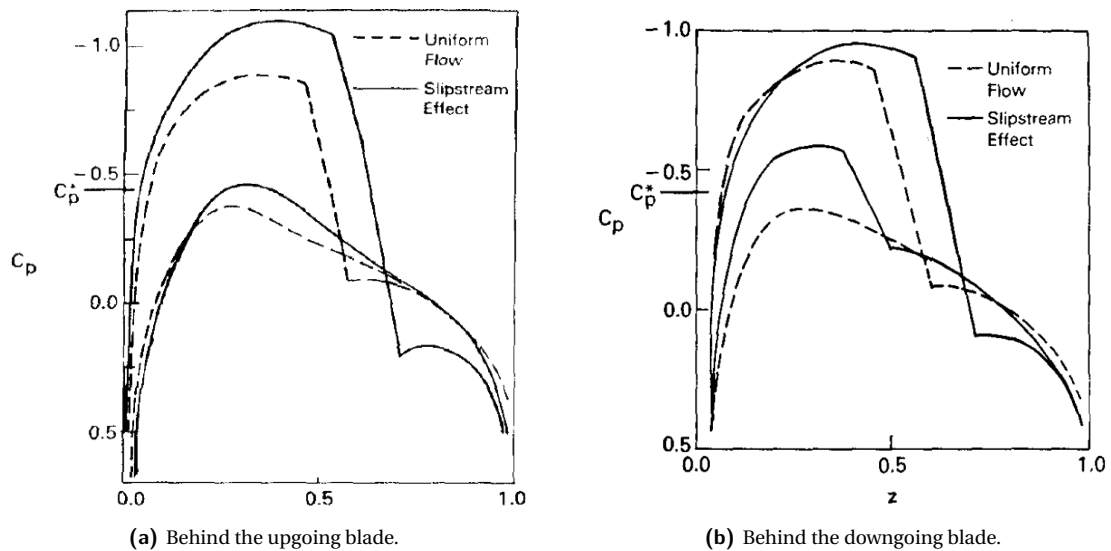


Figure 2.9: Pressure distributions of wing sections at different locations in a propeller slipstream. Image obtained from [36]

# 3

## RESEARCH OUTLINE

In this chapter, the research plan is laid out. It is started with the research questions in [section 3.1](#). A strategy was devised to answer these, which is presented in [section 3.2](#). Apart from the methodology, all wing configurations that will be simulated are summarised there. Finally, these configurations are defined in more detail in [section 3.3](#). Here the propeller, nacelle and wing are shown, along with their operating conditions.

### 3.1. RESEARCH QUESTIONS

Following the discussion in [chapter 2](#), it is expected that the advantage in aerodynamic performance of a strut-braced wing comes in the form of a reduced induced drag. The effect of aspect ratio on induced drag is well known, and is not of interest in this research. More interesting would be to assess the change in induced drag caused by the strut and jury strut. It is already known from literature that unpowered strut-braced wings have the potential of a lower induced drag than a wing without strut, provided that both have an optimal loading distribution. No literature was found on the cruise drag of a propeller-powered strut-braced wing, which will be the objective of this report. The research is split up in three parts. The first, and most important part deals with the induced drag. The second looks at viscous effects, while the aim of the last part is to find out whether compressibility affects the performance of the wing. Based on this, the following research questions and sub-questions were formulated:

1. **How does a propeller affect the induced drag of a strut-braced wing?**
  - (a) **What influence does the main strut have on the induced drag change by a propeller?**
  - (b) **What influence does the jury strut have on the induced drag change by a propeller?**
2. **What is the effect of a propeller on the viscous aerodynamics of a strut-braced wing?**
  - (a) **Are there regions of separated flow, and do they change due to the propeller?**
  - (b) **How much does the addition of a propeller change the friction drag?**
3. **What effect does the propeller have on compressible and interference drag?**
  - (a) **Does the propeller lead to areas with supersonic flow, and associated shock waves?**
  - (b) **Does the propeller increase interference between the different wing elements?**

### 3.2. RESEARCH STRATEGY

In this section, the strategy to answer the research questions is laid out. First, the plan for question 1 is given in [subsection 3.2.1](#). In addition, the different strut-braced wing configurations that will be simulated are presented. Next, the approach for the second and third research questions is treated shortly in [subsection 3.2.2](#). Finally, it is explained how the different methods will be validated in [subsection 3.2.3](#).

### 3.2.1. INDUCED DRAG

The first research question deals with induced drag, and the effect different sub-components of the wing have on it. The effect a certain wing component has on the induced drag is evaluated by comparing the induced drag of the wing with and without that component. In order to investigate the effect of the jury strut and main strut on the induced drag, 3 different aircraft configurations will be used. All of these will be tested in powered and unpowered conditions, to isolate the effects of the propeller. The unpowered condition will include the nacelle, but not the propeller. All configurations are shown in [Figure 3.1](#). Because of the relatively large number of configurations, a panel method is used to keep the computational cost manageable. It will be used only to answer the research questions on induced drag.

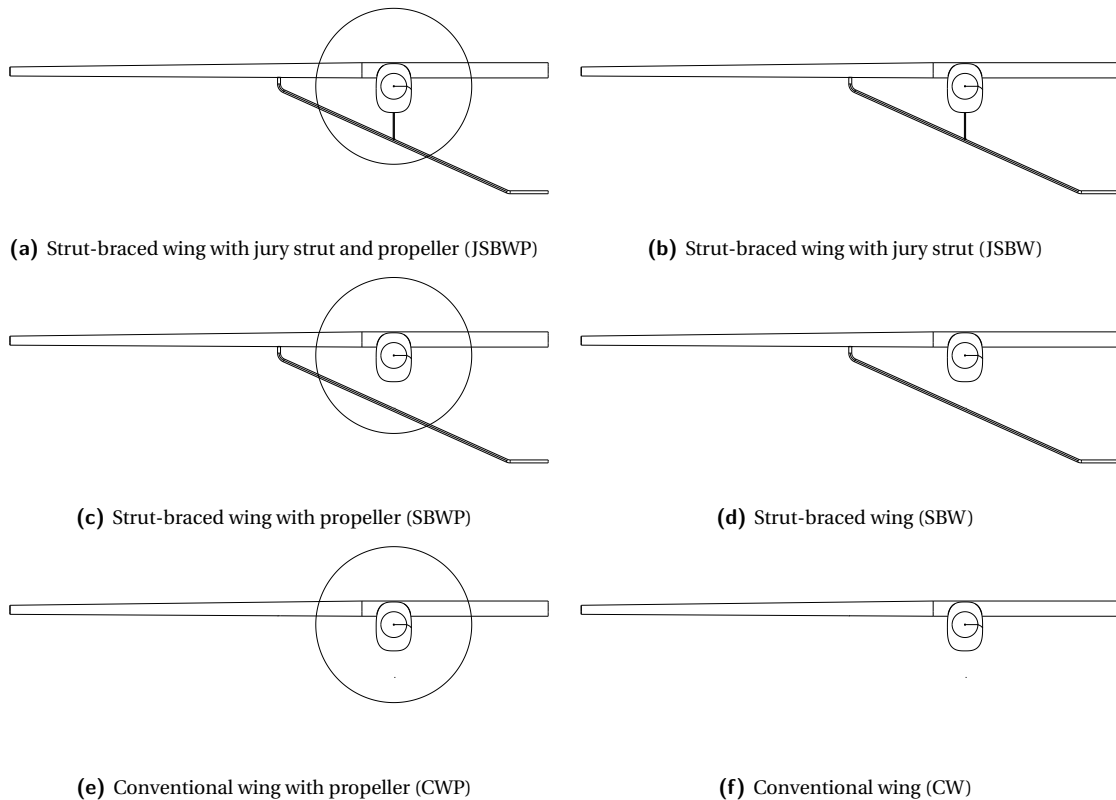


Figure 3.1: Different configurations to be used in the experiment

### 3.2.2. VISCOUS AND COMPRESSIBLE EFFECTS

Induced drag can be evaluated accurately with a panel method. Some panel codes include options to calculate viscous effects and to correct for compressibility. For attached flows at moderate Mach numbers, these are usually reasonably accurate. However, research questions 2a and 3a deal with separation and supersonic flow. To answer these with some accuracy, RANS simulations will be used. Depending on the turbulence model, RANS can have issues with the location and presence of flow separation. This introduces an additional uncertainty to the results. Since the goal of the research is not to resolve the exact location and size of separated regions, but instead to qualitatively assess whether they are present and how they change due to a propeller, this is acceptable. However, for a quantitative treatment of separation and the effect it has on drag, a higher fidelity method may be necessary. For answering research questions 2 and 3, it is sufficient to simulate the JSBW and JSBWP configurations in CFD.

### 3.2.3. VALIDATION

In order to validate the results of the panel method, two configurations will be simulated using RANS. Before starting the main tests, a simplified model will be tested. This model contains a propeller, wing and nacelle, where the wing is mounted some distance below the propeller, see [Figure 3.2](#). It will experience two effects that are expected to be important for strut-propeller interference. First, the slipstream contraction of the propeller should alter its angle of attack. This effect may be reduced because the flow has to go around the

nacelle. Second, the swirl velocity components will not be perpendicular to the plane of the wing. If these are simulated accurately by the panel method, it is assumed that subsequent simulations of the strut-braced wing will yield accurate results as well. When simulations with CFD and the panel code have been performed on the strut-braced wing with jury strut, this assumption is verified by a second validation using the JSBW and JSBWP configurations.

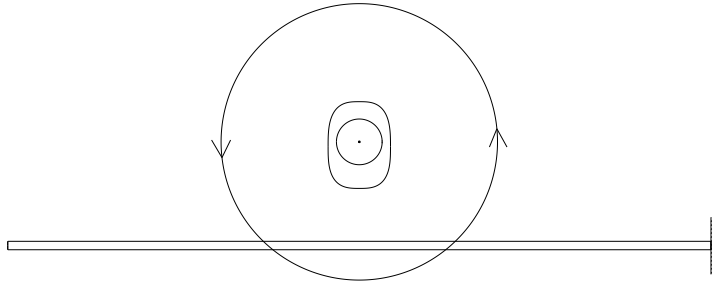


Figure 3.2: Simplified configuration for initial validation

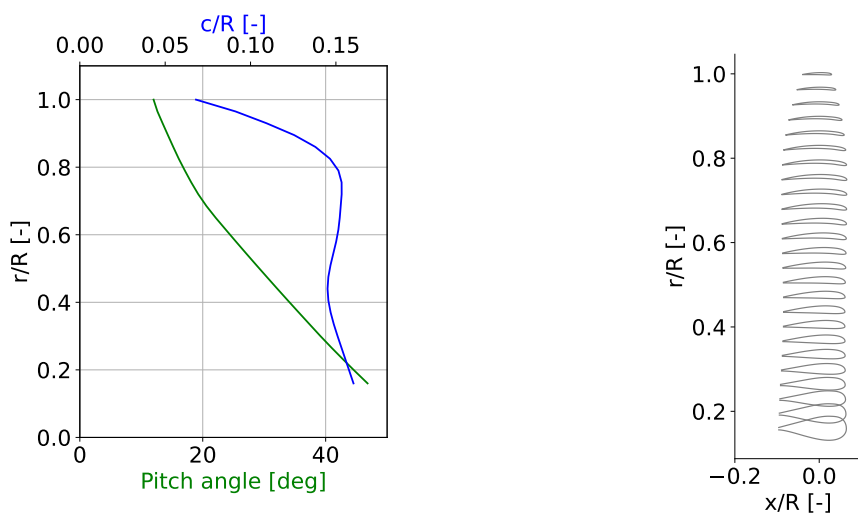
The RANS simulations will not be validated separately. Due to its large popularity, it has been validated numerous times, including propeller-wing configurations. No validation cases for strut-braced wings have been found. Validating this would require either higher fidelity simulations or wind tunnel tests. These would require too much resources for this report.

### 3.3. GEOMETRY

The design and operating conditions of the different configurations are presented in this section. First, the propeller and nacelle geometry are given in subsection 3.3.1. Next, the geometry used for the initial validation is shown in subsection 3.3.2. This simplified configuration consists of only a propeller, nacelle and wing. Finally, in subsection 3.3.3 the design of the strut-braced wing including jury strut (JSBWP) configuration is shown.

#### 3.3.1. PROPELLER AND NACELLE

The propeller and nacelle were chosen to be representative of a conventional turboprop. The propeller used was a scaled up version of XPROP. Because it has been used in multiple studies at the TUDelft, data about propeller performance and geometry were openly available. The propeller geometry was obtained from Stokkermans and Veldhuis [47]. The twist, chord and airfoil distribution is shown in Figure 3.3.



(a) Local pitch and chord distribution for XPROP ( $\beta_{0,7R} = 20deg$ ).

(b) Airfoils used for XPROP

Figure 3.3: XPROP geometry, image based on Stokkermans and Veldhuis [47]

The nacelle was modelled after that of the ATR72 regional airliner. The height and width distribution of the nacelle were modelled using Class-Shape Transformation (CST) functions. The cross-sectional shape was defined by superellipses. Their shape is defined by a height, width and exponent. Based on this exponent, the cross-section can be varied from a rectangle to a circle. It was given a value of three everywhere, which yields a rounded rectangle. At the spinner connection, an exponent of two was used, which represents a circle. The height, width and offset in z-direction are determined from their distributions prescribed by the CST coefficients. The current representation of the shape of the nacelle allows changing it to a different nacelle with relatively few parameters, which could be useful in optimisation studies, although this is outside the scope of this work. Some information about the nacelle geometry has been given in Table 3.1. An isometric view of the nacelle shape, including the superellipses is shown in Figure 3.4.

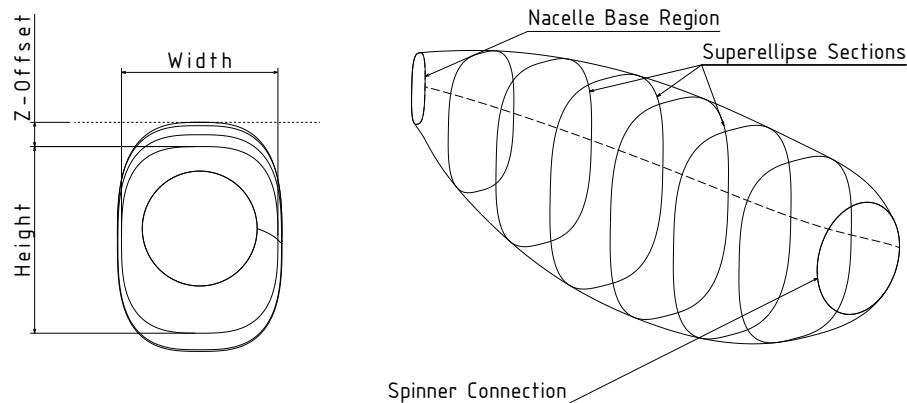


Figure 3.4: Schematic drawing of the nacelle definition

Table 3.1: Nacelle specifications

Parameter	Value
<b>Length</b>	3.4 [m]
<b>Height CST coefficients</b>	618 1230, 1106, 1343, 1278, 1082, 860, 400
<b>Width CST coefficients</b>	618, 1024, 885, 667, 1336, 494, 700, 100
<b>z-offset CST coefficients</b>	0, -58, -209, 91, -156, 108, 75, 181
<b>CST characteristic shape parameters (N1 and N2)</b>	0
<b>Superellipse exponent</b>	2 at the spinner connection, 3 elsewhere

### 3.3.2. INITIAL VALIDATION

The geometry of the initial validation case represents a simplified representation of a propeller-strut combination, designed to capture effects such as slipstream contraction and swirl velocities not perpendicular to the strut. In addition to validating Flightstream, it is used to select some key settings at a modest computational cost. To represent the strut, a straight wing with an aspect ratio of 20 was chosen. The wingtip is positioned relatively far away from the propeller, so that it does not influence the propeller-wing aerodynamics. A propeller is positioned halfway the wing, 0.75 times the propeller radius above the wing plane. The airfoil for the untwisted wing planform is a NACA0012. A drawing of the configuration is provided in Figure 3.5.

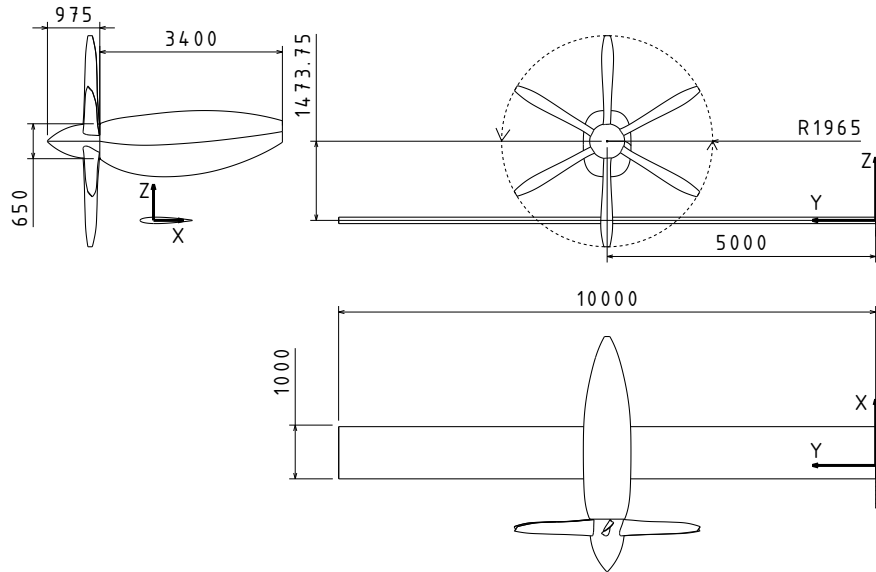


Figure 3.5: 3-view drawing of the validation case. Some key dimensions have been indicated in mm. The hatched areas represent the root of the wing.

The initial validation is ran at conditions representative for a regional turboprop-powered aircraft, to prove that Flightstream can accurately predict the aerodynamic loads at this regime. These are summarised in Table 3.2, together with a short summary of the wing planform.

Table 3.2: Initial validation parameters

(a) Geometry		(b) Operating conditions	
Parameter	Value	Parameter	Value
$b$	20 [m <sup>2</sup> ]	$\rho$	0.6597 [kg/m <sup>3</sup> ]
$S$	20 [m]	$p$	47181 [Pa]
$C_r$	1 [m]	$T$	249.15 [K]
$\lambda$	1	$V_\infty$	133 [m/s]
$A$	20	$M_\infty$	0.42
		$\alpha$	0 [deg]
		$n$	15.92 [Hz]
		$J$	2.13
		$\beta_{0.75R}$	45 [deg]

### 3.3.3. STRUT-BRACED WING CONFIGURATION

The geometry of the full strut-braced wing was loosely based on that of an ATR72. The planform shape is almost identical, consisting of a double tapered wing. Because of a lack of data, and to simplify the analysis, the wing was kept untwisted. In addition, it consisted of a single airfoil, namely the NACA43015, shown in Figure 3.6. The ATR72 wing has a relatively low aspect ratio compared to most SBW concepts. This is justified by the fact that the wing design presented here will not be used in an actual aircraft. It will just be used to identify relevant aerodynamic phenomena, located around the strut region. It is expected that these will not be affected significantly by the aspect ratio of the wing, as long as the tip vortex is situated far enough from the strut. The operating conditions for the strut-braced wing are the same as those of the initial validation. The only exception is the angle of attack, which is 2 degrees for the strut-braced wing. This was chosen because it results in a lift coefficient of 0.4, which is representative for a regional aircraft in cruise conditions.

The strut and jury strut were both given a symmetric airfoil, the NACA 65015, see Figure 3.7. This was done because it can be loaded both positively and negatively at different locations. Although using different airfoils

along the span could lead to a more efficient wing, it was decided to keep the airfoil constant. This is justified because the focus of this report is on identifying aerodynamic phenomena, and not on creating the most optimal strut-braced wing. Both the main and jury strut were kept untwisted for the same reason. The chord of the strut is 500 mm, or 10.6% of the wing root chord. The jury strut has a chord length of 200 mm, or 40% of the main strut chord.

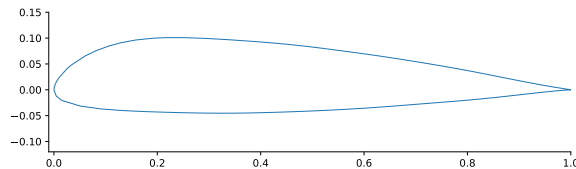


Figure 3.6: NACA43015 airfoil used for the wing

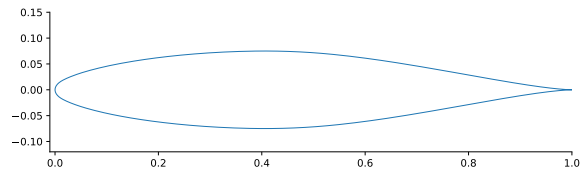


Figure 3.7: NACA65015 used for the strut

The main strut was rounded with a radius of 200 mm near the pylon and near the root. This was done to reduce the interference effects of junction flows, and to allow a better mesh quality at those locations. Additionally, to facilitate meshing the geometry, fillets of 10mm were added to the nacelle-wing, jury-nacelle, jury-main strut and main strut-wing junctions. A smaller, 5mm fillet was added to the wingtip. A three-view drawing of the strut-braced wing configuration is shown in [Figure 3.8](#). In addition, some key geometric parameters for the wing, strut and jury strut are listed in [Table 3.3](#).

Table 3.3: Geometric parameters for the strut-braced wing.

(a) Main Wing		(b) Strut		(c) Jury Strut	
Parameter	Value	Parameter	Value	Parameter	Value
$b$	27.13 [m]	$\eta_{\text{strut}}$	0.5	$\eta_{\text{jury}}$	0.286
$S$	61 [m <sup>2</sup> ]	$x/c_{\text{strut}}$	0.25	$x/c_{\text{jury}}$	0.25
$\eta_{\text{kink}}$	0.35	$C_{\text{strut}}$	0.5 [m]	$C_{\text{jury}}$	0.2 [m]
$C_r$	2.626 [m]	$h_s$	3 [m]	$h_{js}$	0.87 [m]
$\lambda_{\text{kink}}$	1	$l_p$	0.16 [m]		
$\lambda_{\text{chord}}$	0.59				
$A$	12				
$\bar{c}$	2.235				

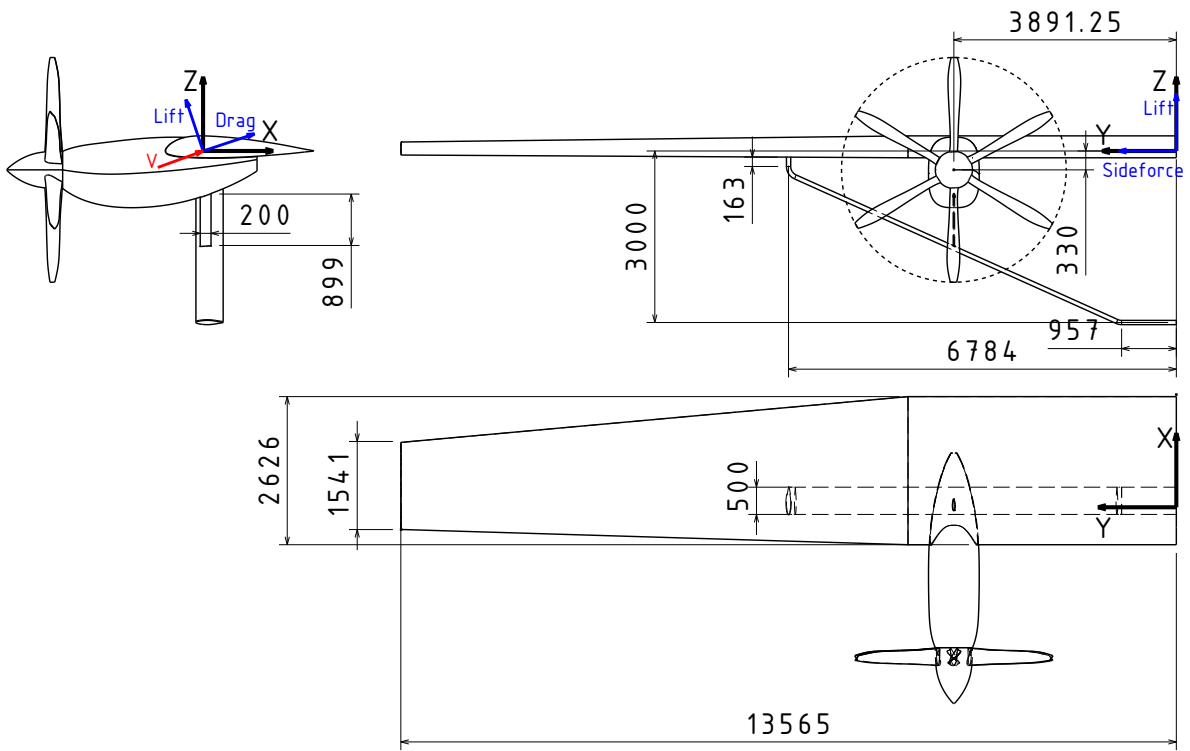


Figure 3.8: 3-view drawing of the strut-braced wing, with dimensions in mm. The positive directions for lift, drag and sideforce have been indicated in blue.



# 4

## COMPUTATIONAL SETUP

This chapter explains the computational tools that were used for the simulations. [section 4.1](#) is a short theory section on the different methods that were used for simulating, and how errors are estimated. The setup for the panel method and CFD simulations for the initial validation case is given in [section 4.2](#). That for the strut-braced wing follows in [section 4.3](#). The aim is to justify some of the most influential settings for both CFD and Flightstream. This is only done for the initial validation. As the operating conditions are the same, it is assumed that the conclusions will hold for the strut-braced wing as well. In addition, mesh refinement studies are done for both methods, to quantify the spatial discretisation error and select a suitable mesh for further study.

### 4.1. METHODOLOGY

In this section, the theory behind the methods that will be used for the research are explained. First, an introduction is given to panel methods in [subsection 4.1.1](#). It is started by a brief overview of the capabilities of panel methods in general, followed by some of the methods used by Flightstream, which is the panel code used in this report. Next, CFD is treated in [subsection 4.1.2](#). Some examples are given of a few relevant studies that used RANS, along with a few limitations they discovered. In addition, the turbulence model used is explained. Finally, [subsection 4.1.3](#) goes over the different types of errors that arise in numerical simulations.

#### 4.1.1. PANEL METHODS

Panel methods are a relatively cheap way to simulate aerodynamic flows. They solve the potential flow equation, which represents the velocity field based on one variable only, the potential function  $\phi$ . To achieve this simplification, the assumption of irrotational, incompressible flow is made. Luckily, the flow is usually irrotational outside boundary layers and shockwaves. Instead of having to mesh the entire flow domain, only the surfaces of bodies in the flow have to be discretised, together with their wakes. This leads to a much smaller system that needs to be solved. Propeller integration studies can be performed using unsteady panel methods. Accurate results for a wing and tractor propeller were obtained by Ahuja and Litherland [3], especially at low to moderate angles of attack. Furthermore, because thickness of bodies is simulated, the resulting flowfield can give an idea of interference effects. Shock waves can be avoided indirectly by eliminating high supersonic velocities found with the panel method [20]. Results obtained by Valzero [54] for an aircraft with tail mounted engines show good agreement of the pressure distribution on the fuselage between experiment and panel code. He used dipoles to model the lifting surfaces and wake. Combining the pressure fields obtained from the panel method with a boundary layer calculation can allow viscous effects to be considered as well. Panel methods can be coupled to boundary layer calculations using an iterative procedure [21], where the effect of the boundary layer thickness on the external flow is captured as well.

The panel code that will be employed for the research is Flightstream. This is a commercial package developed by Research In Flight. To model wakes, it uses vortex elements. It has been used successfully by several researchers. Ahuja and Litherland [3] used Flightstream to simulate a propeller-wing combination. They found good agreement with unsteady Reynolds Averaged Navier-Stokes (URANS) solutions and delayed detached eddy simulations (DDES) at moderate angles of attack. However, behaviour of separation was not

simulated well by Flightstream. Separation is modelled by the empirical condition proposed by Stratford [49], and is valid only for turbulent flows.

An inherent limitation of panel codes when simulating propeller-wing interactions is the absence of viscous dissipation in the wake. In reality, viscosity reduces the strength of propeller tip vortices. In Flightstream, the propeller wake convects through any panels in its path. This may lead to local peaks in lift and drag, as the unattenuated vortex core gets very close to a wing panel and induces a large velocity there.

A short explanation on the boundary layer model of Flightstream is given here, largely based on Ahuja et al. [2]. The boundary layer is implemented in Flightstream by solving boundary layer equations along surface streamlines. There is the option to use a laminar, turbulent or transitional boundary layer. The laminar boundary layer is modelled using Thwaites method [52]. The turbulent model used is a modified version of the model derived by Standen [45]. Transition is accounted for by changing the boundary layer type at a prescribed location. This location is found using the method of Dvorak et al. [13]. Flightstream has the option of iterating between the boundary layer model and the inviscid flow calculation. First the inviscid solution is calculated, which is used for the boundary layer calculation. Based on the displacement thickness of the boundary layer, a normal velocity component is found. This normal velocity accounts for the boundary layer growth by blowing the flow streamlines away from the surface of the body. The magnitude of it is found based on the momentum flux into the boundary layer. In a second inviscid calculation, they are accounted for by modifying the Neumann boundary conditions. This procedure is iterated until the inviscid and viscous solutions converge [2].

Flightstream has the option to correct for compressibility, but uses the Prandtl-Glauert or Karman-Tsien correction, depending on the freestream Mach number. These correction factors do not capture any shock-related phenomena. As a consequence, it is not possible to answer the research question about wave drag using Flightstream.

To obtain the magnitude and distribution of forces and moments, there are two methods in Flightstream; one based on surface pressure integration and another based on vorticity, using the Kutta-Joukowski theorem. As the name suggests, surface pressure integration integrates the pressures along the surface of the body. For lift, surface integration is relatively accurate. However, it is very sensitive to the panelling when considering pressure drag. To capture all gradients in pressure, extremely dense panelling is required, both in chordwise direction [53] and spanwise direction [42]. The Kutta-Joukowski method for calculating lift and induced drag is less sensitive to panel density. In Flightstream, it works by dividing the wing in multiple sections in spanwise direction, located at the nodes of the trailing edges of the wing [1]. The local lift of a wing section is obtained from the circulation around that section, based on the velocity induced by the bound vorticity, using Equation 4.1. Using the local circulation at all sections, lifting line theory can be applied to find the downwash at a section located at  $y$ , with the help of Equation 4.2. In the case of a wing consisting of multiple elements and a propeller, their respective downwash components should be added too. This, combined with the local circulation can be used to find the local induced drag, with Equation 4.3.

$$L_{loc} = \rho_{\infty} V_{\infty} \Gamma_y \quad (4.1)$$

$$w_y = \frac{1}{4\pi} \int_{-\frac{b}{2}}^{\frac{b}{2}} \left( \frac{1}{y - y_0} \right) \frac{-d\Gamma_{y_0}}{dy} dy_0 \quad (4.2)$$

$$D_{i,loc} = \rho_{\infty} w_y \Gamma_y \quad (4.3)$$

#### 4.1.2. COMPUTATIONAL FLUID DYNAMICS (CFD)

Reynolds-averaged Navier Stokes (RANS) solvers are a popular method to numerically solve the Navier-Stokes (NS) equations. To reduce computation time, only the averaged solution of the NS equations is solved for, ignoring fluctuations. This may limit their applicability for propeller-wing interaction, which are per definition unsteady. This can be solved by including slow unsteady effects, and solving the URANS equations. Since fluctuations in the flow due to the propeller can be considered slow compared to typical turbulent fluctuations, URANS is generally applicable to these problems.

Sinnige et al. [40] used URANS to evaluate the aerodynamic performance of a propeller with swirl recovery vanes. The flow fields obtained both by CFD and Particle Image Velocimetry (PIV) of a wind tunnel experiment were compared. It was found that RANS approximated the velocity profile near the center of the propeller disk rather well. However, numerical diffusion reduced the accuracy of the outboard part of the blades,

due to the large velocity gradients in the tip vortices. It was concluded that RANS approximated the flow well enough to be used as a tool to assess the relative trends in efficiency of swirl recovery vanes. When comparing actual torque and thrust coefficients, the CFD simulation was found to predict the torque within 2% for all power settings. The thrust coefficient was only accurate to within 10%, being least accurate at low thrust conditions.

Validation of the Flightstream results will be performed with RANS. In addition, it will be used to answer the final research questions, about viscous effects, interference and wave drag. Still, turbulence modelling reduces the accuracy of boundary layer flows in RANS, which may not yield accurate results for junction flows, such as between wing and nacelle or wing and strut. In these regions, boundary layers of different components will interact with each other and be influenced by the pressure fields around the different bodies. As described by Gand et al. [17] for a wing-body, RANS does not simulate these interactions very well. The issue in the present research might however not be as large as that described by Gand et al., as here the incoming boundary layer on the nacelle and wing or strut will likely not have developed a large thickness yet. Additionally, this report aims to qualitatively identify flow phenomena relevant to propeller-powered strut-braced wings. For example, the exact location of a separated region is not of interest, as long as it is present at the approximate location.

#### A. TURBULENCE MODELLING

Since turbulence is modelled through the Reynolds stress tensor, boundary layer aerodynamics depends on which model is used. This can affect the location of transition and separation, which are not always accurate when using RANS. Therefore, it is important to properly validate results, for example by comparison to wind tunnel experiments. Stokkermans et al. [48] compares the Spalart-Allmaras (SA) and  $k-\omega$  models to experimental data for the simulation of a wingtip propeller whose slipstream impinges on a flap. It was found that the SA model predicted separation on the flap much better. Furthermore, it exhibits less numerical diffusion than  $k-\omega$ , which mainly benefits the rear part of the wing. The SA model predicted lift and drag very accurately as well. The study concludes that the SA model is suitable for simulation of wingtip-mounted tractor propellers, as long as the numerical diffusion is quantified by a grid refinement study. Since a lot of the phenomena are the same for strut-braced wings, this model could be useful to investigate propeller integration effects. It has however not been checked whether it also applies at a higher speed regime, since the study was done at a freestream velocity of 40 m/s. [48]

Due to the good results obtained by Stokkermans et al, it is decided to use the Spalart-Allmaras model for the CFD simulations in this report. The Spalart-Allmaras model is a one equation eddy viscosity model, which solves for the turbulent viscosity  $\tilde{\nu}$ . The transport equation is given by Equation 4.4 [43]. By default, the flow is turbulent everywhere in the boundary layer. It is possible to add a laminar region by setting  $\tilde{\nu}$  to zero, although this requires a slight modification to the turbulence production term to ensure numerical stability. In the present report, the fully turbulent model is applied.

$$\frac{D\tilde{\nu}}{Dt} = c_{b1}\tilde{S}\tilde{\nu} + \frac{1}{\sigma} [\nabla \cdot ((\nu + \tilde{\nu})\nabla\tilde{\nu}) + c_{b2}(\nabla\tilde{\nu})^2] - c_{w1}f_w \left[ \frac{\tilde{\nu}}{d} \right]^2 \quad (4.4)$$

Originally, a  $y^+$  value of 1 was required to fully resolve the viscous sublayer of the boundary layer. However, using wall functions, this is no longer needed in Fluent. By assuming an (empirical) model for the variation of velocity and other important quantities for the boundary layer, such as  $\tilde{\nu}$ , it is possible to fill in the part of the boundary layer not resolved by the mesh. While this is generally accurate for attached flow, it can introduce errors when trying to model separation. Eça et al. [14] found that the location of separation on a cylinder was not estimated well when using wall functions. Furthermore, no literature was found on how wall functions perform in junction flows and when dealing with propeller wake-boundary layer interaction. For this reason, it was decided to resolve the boundary layer with a  $y^+$  in the order of 1 everywhere.

#### 4.1.3. ERROR ESTIMATION

There are multiple types of errors associated with numerical modelling. They are listed below. Not all of these can readily be calculated. In this report, only discretisation errors will be estimated. Modelling errors can be estimated by performing validation. Propeller-wing aerodynamics have been simulated using RANS in numerous publications, some of which included validation with wind tunnel simulations (see [48], [61]). Therefore, the CFD simulations in this report will not be validated separately. Instead, they will be used as

validation case for the panel code results. Iteration errors are also not quantified here. To ensure them being small enough, it is sufficient to let the CFD and Flightstream simulations reach sufficiently low residuals.

- **Modelling errors** These stem from simplifications and uncertainties in the physical model used. For example, turbulence modelling in the RANS equations reduces the cost of a simulation, but introduces a modelling error.
- **Discretisation errors** Introduced by representing the governing equations on a discrete grid. This way, a finite number of algebraic equations is reached, which can be solved for the solution. This only approximates the real solution. The discretisation error is the difference between the real solution of the governing equations and those obtained on the finite grid.
- **Iteration errors** Iterative procedures are usually applied to solve the algebraic system. This is to avoid the high computational cost of directly solving a large matrix. When reaching a certain accuracy or number of iterations, the iterations are terminated. The exact solution of the algebraic relations is usually not yet reached at this point, introducing the iteration error.
- **Round-off errors** Round-off errors follow from the number representation on computers. They only have a finite precision, depending on how many bits are used to store the number. Usually this kind of error is smaller than the other 3, and can be ignored.

#### A. DISCRETISATION ERRORS

It is important to quantify discretisation errors. It serves as a verification tool, ensuring that the mesh used for a simulation is fine enough to capture all gradients. In addition, for CFD simulations it gives an estimate of the magnitude of numerical diffusion. This is especially important in propeller-wing studies, as the propeller tip vortex is particularly susceptible to numerical diffusion due to the large gradients [48]. Finally, it can explain differences between the results of two methods during validation. If the difference between those results are larger than the discretisation error, one can be reasonably sure that the error does not originate from the mesh.

The discretisation error associated with spatial discretisation will be estimated for both the panel method and CFD. This will be done using the method of Eça and Hoekstra [15]. According to Richardson extrapolation, the discretisation error of a solution on grid  $i$  ( $\phi_i$ ) can be calculated as in Equation 4.5. In this equation,  $p$  is the observed order of accuracy of the method,  $h$  the grid cell size and  $\alpha$  a constant. Note that higher order terms in the error are ignored, it is assumed that the grid is fine enough for the solution to be in the asymptotic regime.

$$\delta_{RE} = \phi_i - \phi_0 = \alpha h_i^p \quad (4.5)$$

In theory, one needs only the solutions on three different grids to find  $\alpha$ ,  $\phi_0$  and  $p$ . However, usually higher order terms are present, and the solution does not converge monotonically over the different grids. Therefore, Eça and Hoekstra proposed using solutions on more than three grids, and applying least squares to find the three unknowns in Equation 4.5. The function to be minimised is then Equation 4.6. The standard deviation is found by Equation 4.7. In these equations,  $n_g$  represents the number of grids.

$$S(\phi_0, \alpha, p) = \sqrt{\sum_{i=1}^{n_g} (\phi_i - \phi_0 - \alpha h_i^p)^2} \quad (4.6)$$

$$U_s = \sqrt{\frac{\sum_{i=1}^{n_g} (\phi_i - \phi_0 - \alpha h_i^p)^2}{n_g - 3}} \quad (4.7)$$

In order for Richardson extrapolation to be applicable, the solution should converge monotonically over the different grids, which is characterised by  $p > 0$ . For a second order method, such as the CFD simulations performed in this report, the error can be found according to Equation 4.8. With  $\Delta_M = \max(|\phi_i - \phi_j|)$ .

$$\begin{aligned} U_\phi &= 1.25\delta_{RE} + U_s & \text{if } 0.95 \leq p < 2.05 \\ U_\phi &= \min(1.25\delta_{RE} + U_s, 1.25\Delta_M) & \text{if } 0 < p < 0.95 \\ U_\phi &= \max(1.25\delta_{RE} + U_s, 1.25\Delta_M) & \text{if } p \geq 2.05 \end{aligned} \quad (4.8)$$

For a panel method, it is less clear what the order of accuracy is. It depends on how the panels are modelled (straight/curved), what distribution of vorticity is used (linear, quadratic,...). According to Oskam [33], a quadratic doublet distribution leads to third order accuracy, whereas piecewise constant doublet strengths over panel gives first order accuracy. Flightstream uses vortex panels, which might give another order of accuracy. To simplify matters, Equation 4.9 will be used to estimate the discretisation error for the Flightstream simulations.

$$U_{\phi} = 1.25\delta_{RE} + U_s \quad (4.9) \quad U_{tot} = \sqrt{U_{\phi, chord}^2 + U_{\phi, span}^2} \quad (4.10)$$

Panel density in chord- and spanwise direction are refined in two separate studies. This is necessary to ensure monotonic convergence. The total discretisation error of the wing is then found by adding the chord- and spanwise errors together, according to Equation 4.10. Disadvantages of this method are that faces can become very skewed at high refinements and that interactions between chordwise and spanwise panel density are not captured. The former can lead to a degradation in accuracy, and can be avoided by not refining the mesh too much. The latter is harder to assess, and introduces another uncertainty.

## 4.2. INITIAL VALIDATION

The initial validation case was conceived as a relatively cheap way to validate Flightstream. In addition, it is used to investigate the effect of propeller and boundary layer modelling and to find a suitable timestep for further simulations. The results of these are presented in subsection 4.2.1, together with a mesh refinement study for the wing. The setup for the CFD simulation of the initial validation is given in subsection 4.2.2. Here the computational domain is shown, including refinement regions and the settings used to create the mesh. Solutions on three different grids are shown as well, to demonstrate the independence of the results on the mesh.

### 4.2.1. FLIGHTSTREAM

The setup for the initial validation in Flightstream is treated in this section. Since an unsteady panel code simulation still has a reasonably high computational cost, it is tried to reduce the computational effort where possible. Some gains are possible by making simplifications in the propeller model, which is explained qualitatively in subsection A. Next, iterating between the boundary layer model and the potential flow solver increases the time needed for the solver to converge. In subsection B, the necessity of such a viscous iteration is considered, by comparing the results with and without it. One of the settings having the largest influence on the computational cost of an unsteady panel code is the timestep used. The temporal discretisation error is estimated in subsection C. Finally, the influence of the panel density on the initial validation wing is quantified in subsection D, the same procedure is repeated for the propeller in subsection E. The mesh settings found based on these refinement studies are presented in subsection F.

#### A. PROPELLER MODELLING

There are different ways of modelling a propeller in a panel code. The most accurate way is to mesh the actual blade, and simulate it directly in the panel code. This is also the most computationally expensive method, as it requires a relatively high number of faces. A reduction in mesh faces can be obtained by instead only using the mean camber line of the propeller. Essentially, this means using the Vortex Lattice Method (VLM). The propeller is replaced by a curved plane, roughly halving the size of the mesh. While this significantly changes the flowfield in close proximity to the propeller itself, it should still be reasonably accurate for the induced velocities in the farfield. It is these farfield velocities that are of interest in this report, more specifically their interactions with the wing. Finally, the simplest method is to represent the propeller by an actuator disk. Using an actuator disk allows the propeller-wing combination to be simulated in steady state. Flightstream has this option, which is based on the method from Conway [10]. An actuator disk greatly reduces computational cost, but comes at the price of several disadvantages. First, the propeller is not simulated. The thrust and rotational speed are provided by the user, based on which swirl and jet velocities are calculated. In Flightstream, these are found based on the assumption that the load distribution on the propeller blades is elliptical. Additionally, the propeller slipstream is superimposed on the freestream, and does not deform under the influence of the wing.

The disadvantages of the actuator disk model were considered too great, so it was not considered for the research. Instead it was decided to use the mean camber line to model the propeller, as it provides a good

trade-off between accuracy and computational cost. Later on, in [section 5.1](#) the thrust and torque distribution of the full blade and VLM are compared to CFD to validate the propeller modelling.

Because of the proximity between the spinner and nacelle, stability issues were observed when the spinner rotated with the propeller, as would be the case in reality. To prevent these and simplify the meshing process, the propeller blades were detached from the spinner. When rotating, the blades 'slide' over the spinner. A disadvantage of this method is that the flow can leak between the blades and the spinner, introducing an additional uncertainty.

## B. BOUNDARY LAYER MODEL

As explained in [subsection 4.1.1](#), Flightstream can solve boundary layer equations based on the potential flow solution. There are multiple options to simulate the boundary layer. The two expected to be the most influential are the type of boundary layer (turbulent, laminar or transitional), and whether to include an iteration between the boundary layer calculation and the potential flow solution, to account for the effect of the boundary layer thickness.

As for the boundary layer type, it was decided to go with a fully turbulent boundary layer. For the initial validation case, the wing is operated at a Reynolds number of 5 million. According to a wind tunnel test at  $C_L = 0$  and  $Re = 5.2 \cdot 10^6$ , the transition location for a NACA0012 airfoil lies at around  $x/c = 0.29$  [6]. Assuming fully turbulent flow ignores the laminar flow at the leading edge, but gives a more conservative estimate of friction drag. The strut, which uses a NACA63015 airfoil, exhibits transition at  $x/c = 0.54$  at the same Reynolds number according to XFOIL. This makes the use of a fully turbulent boundary layer harder to defend. However, in reality transition will happen before this point due to contamination of the wing surface. In addition, the CFD simulations were done using the Spalart-Allmaras model, which also assumes fully turbulent flow. Since the actual friction drag is not of interest for the Flightstream simulations, the only function of the boundary layer calculation would be to have the correct thickness when iterating between the panel code and viscous model, to account for the decambering effect. For this reason, using the turbulent model is deemed sufficiently accurate.

In addition to the turbulence model, it was also investigated how much effect the viscous coupling has on the results of the simulation. When viscous coupling is turned on, Flightstream first calculates the flow around a body assuming inviscid flow. After this, the boundary layer thickness is calculated. Next, Flightstream does a new inviscid calculation, which accounts for the boundary layer thickness.

The effect of viscous coupling has been assessed by comparing the lift, friction and pressure drag with viscous coupling on and off. The results of this are shown in [Figure 4.1](#). The simulations were done using the actuator disk model because it fast. It was mentioned earlier that this was not accurate enough for the initial validation and SBW aircraft. However, for assessing the effect of viscous iterations it is adequate. Surprisingly, the lift increases slightly because of viscous-coupling. It is unclear why this is the case, normally the decambering effect reduces the effective curvature of the airfoil, thereby reducing the lift. The friction drag is unchanged by turning on viscous coupling, which is expected, as only one boundary layer calculation is done. Another surprising result is seen in the pressure drag, which remained mostly unchanged. One would expect the decambering effect to increase the pressure drag, as it reduced the pressure on the trailing edge of the airfoil. Because the viscous coupling option only introduced small changes to the results, it will not be used for the remainder of the report. Instead, all friction drag presented from Flightstream is obtained by performing a boundary layer calculation on the inviscid solution directly, without feeding the boundary layer thickness back into a second inviscid iteration.

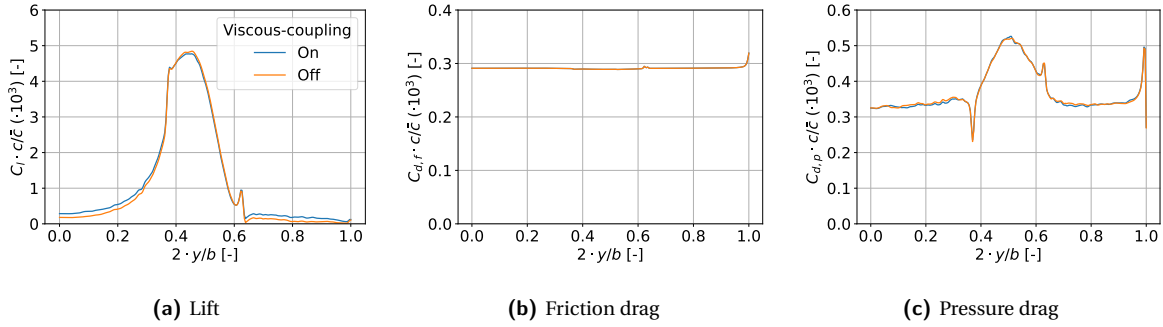


Figure 4.1: Effect of viscous-coupling on the lift, friction drag and pressure drag distributions of the initial validation configuration.

### C. TIMESTEP CONVERGENCE

Since the number of timesteps has a large influence on the computational time of a panel method, it was attempted to find the largest timestep that still gave sufficiently accurate results. 4 simulations were performed using a very coarse mesh, consisting of roughly 29000 cells. The geometry was the same as that used for the initial validation. Over these simulations, the timestep was decreased, while keeping the total simulated time constant at 0.0629 sec, which corresponds to one full propeller rotation. The different timesteps were chosen to represent 20, 15, 10 and 5 degrees of propeller rotation per step.

Table 4.1 summarises the timesteps and total wall clock times needed for each simulation. In addition, the wing lift and drag and propeller thrust averaged over 60 degrees of propeller rotation are given. Due to the dramatic increase in wallclock time beyond a timestep corresponding to 10 degrees of propeller rotation, it is decided not to use a smaller timestep.

Table 4.1: Investigation of the effect of the timestep on the accuracy and run-time of Flightstream. The values obtained by Richardson extrapolation have been added in the final column.

Deg per timestep	20	15	10	5	Richardson Extrapolation
Timestep	0.003491	0.002618	0.001745	0.0008725	
Iterations	18	24	36	72	
Time needed [min.]	10.6	47.5	44.8	197	/
$C_{L,avg} [-]$	0.0216	0.0182	0.0172	0.0164	0.0161
$C_{D,avg} [cts]$	47.2	48.1	48.9	50.2	49.8
$C_{T,avg} [-]$	0.221	0.217	0.211	0.202	0.205

In Figure 4.2, the lift, drag and thrust are plotted versus the timestep, together with the error bar corresponding to the time discretisation error at a timestep corresponding to 10 degrees of propeller rotation, calculated following the method from subsection 4.1.3. According to Richardson extrapolation, the lift converges to a value of 0.0161. The drag converges to 49.8 counts. Because the lift is very small, the induced drag represent less than 1% of the total drag. From this it can be concluded that profile drag is not influenced much by the timestep. The thrust coefficient, shown in Figure 4.2b does not level off at a constant value. Instead it seems like the difference in thrust increases when reducing the timestep. Since the convergence is not monotone, the estimated error may not be representative.

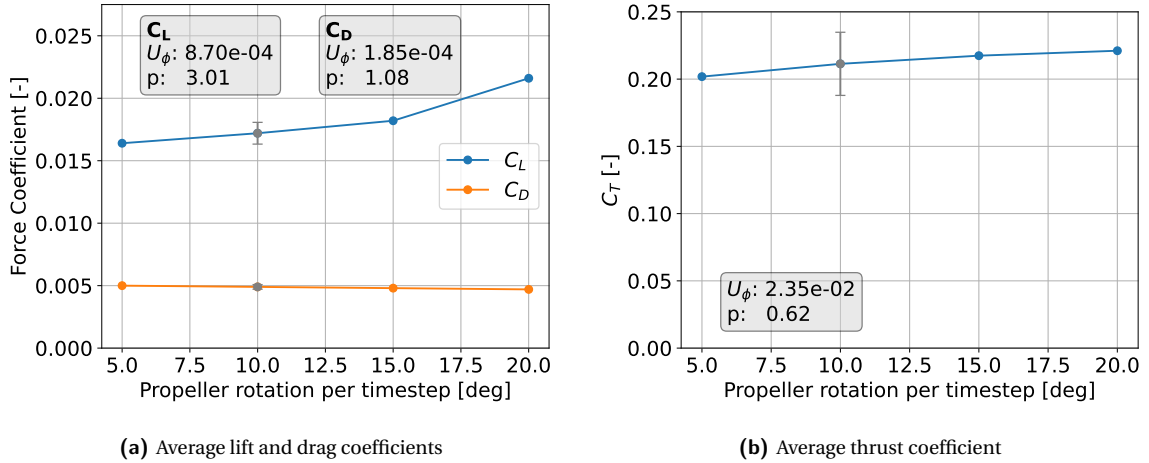


Figure 4.2: Wing lift and drag and propeller thrust coefficients averaged over 60 degrees of propeller rotation. The estimated temporal discretisation error and observed order of accuracy are given in the grey text boxes.

Figure 4.3 shows the average lift and drag distribution for three of the time steps. The lift distribution for 15 degrees of propeller rotation per step has been omitted for clarity. These plots have been obtained by integrating surface pressure and shear forces at different spanwise stations of the wing in Flightstream. It can be seen that all distributions follow the same trend. While the largest timestep is quite different, especially in terms of drag, the two smallest timesteps agree more closely. For lift, the largest differences are in the peaks at  $2 \cdot y/b = 0.45$  and  $2 \cdot y/b = 0.58$ . In addition to this, the coarsest step overestimates lift almost everywhere on the domain. At the first location, the largest timestep differs 25% from the smallest, whereas the 10 degrees per timestep gives a difference of 8%. The second peak has a lower error absolute error, but since the values of lift are lower, the relative error is large. The graph corresponding to 20 degrees/step has an error of 60%, a timestep of 10 degrees gives a difference of 39%.

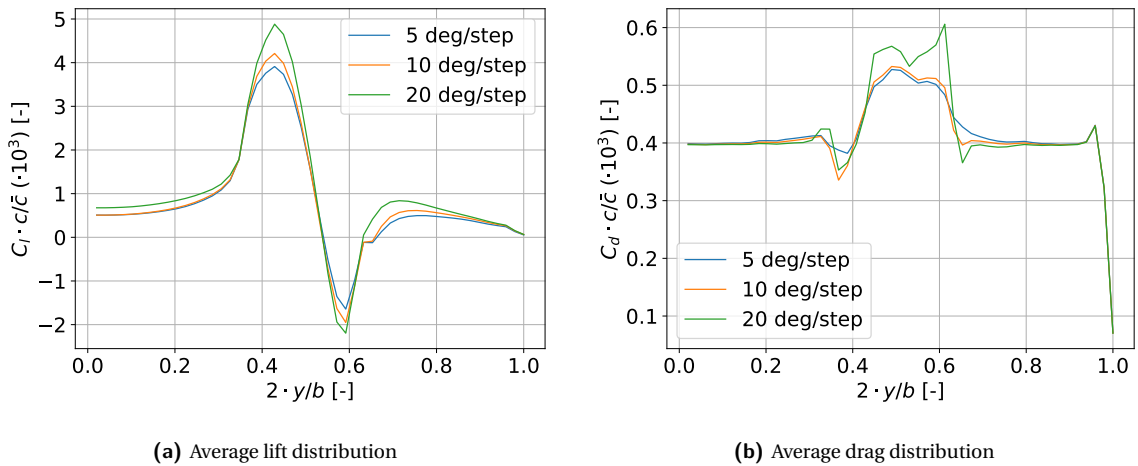


Figure 4.3: Lift and drag distributions for different timesteps.

For drag, the three timesteps agree well outside the propeller slipstream, which extends from  $2 \cdot y/b = 0.37$  to  $0.63$ . The largest differences are at the edges of the slipstream, where there is a difference of 9% between 20 and 5 degrees per step, and 13% between 10 and 5 degrees per step for the inboard edge. At the outboard edge, the difference with the smallest step is 15% and 6% for 20 and 10 degrees per step, respectively. In the slipstream itself, the largest timestep differs 8% from the smallest step on average. A timestep of 10 degrees propeller rotation per step gives a smaller difference, of roughly 2%. It was already confirmed that using a timestep of 10 deg/step gives a small integral error in lift in drag. The force distribution graphs also prove that the behaviour of lift and drag for this step does not differ significantly from a finer timestep.

#### D. WING MESH REFINEMENT STUDY

To make sure the results of Flightstream were not mesh-dependent and to have an idea of the mesh error in the results, a mesh convergence study was done. Contrary to CFD, the mesh was not refined uniformly. Instead, the number of cells in chord- and spanwise direction were varied separately. This was done because it gave more uniform convergence, making it easier to calculate the discretisation error. A disadvantage of this method is that mesh faces can become too stretched at high refinements, which can cause issues with the stability of the solver. To prevent this, the refinement had to be kept within certain bounds. For the initial validation geometry, a mesh convergence study was only performed for the wing. Since only the lift and drag of the wing was of interest, the nacelle and spinner were ignored. The lift, induced drag and zero-lift drag were obtained using the Kutta-Joukowski Theorem. This gives more accurate results than surface pressure integration.

To save time, no unsteady simulations were performed for the mesh convergence study. The propeller was instead modelled using an actuator disk. It has already been established that this is not sufficiently accurate. Among other reasons, the influence of the wing on the propeller is not captured. Since the propeller is relatively far away, the mesh density should not impact these interactions too much. The actuator disk still imposes a representative swirl and jet velocity on the wing at a very modest computational cost. When assessing whether a mesh is fine enough to capture all propeller-induced effects, it is assumed sufficient.

**Chordwise mesh spacing** First, the number of cells in chordwise direction was varied. Initially, no growth scheme was applied to the cells in chord direction. The number of cells in spanwise direction was kept constant at 316. The values for lift, profile and induced drag are given in Table 4.2. The values obtained using Richardson extrapolation are given in the last column. Based on these values, the discretisation error was calculated for each mesh, also shown in the table. The errors for lift and induced drag reduce relatively quickly. On the other hand, the profile drag exhibits very slow convergence. This is visualised in Figure 4.4. For this research, the profile drag will be analysed using CFD, and hence it is not necessarily to resolve the boundary layer properly in Flightstream.

Table 4.2: Lift, profile drag and induced drag for different numbers of chordwise nodes. The values for each variable, obtained by Richardson extrapolation have been added as well. In the bottom three rows, the discretisation error for each mesh is given, based on the extrapolated value.

Nodes	Mesh Convergence Study					Richardson Extrapolation	
	10	20	40	80	160	$\phi_0$	Pobs
$C_L$ [-]	0.0066	0.0176	0.0198	0.0221	0.0222	0.02224	1.75
$C_{D,0}$ [cts]	42.4	60.6	77.4	91.2	106.7	285.0	0.65
$C_{D,i}$ [cts]	0.58	0.60	0.65	0.64	0.65	0.67	0.79
$U_{C_L}$ [%]	90.9	29.0	16.6	4.0	3.4		
$U_{C_{D,0}}$ [%]	106.7	98.7	91.3	85.3	78.5		
$U_{C_{D,i}}$ [%]	18.5	14.1	4.8	6.0	4.4		

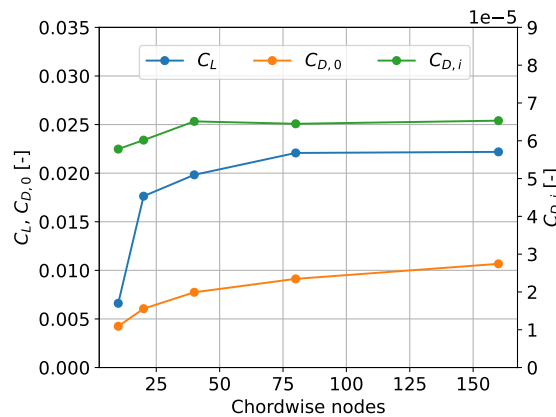


Figure 4.4: Plot showing the evolution of lift, induced and profile drag for different numbers of nodes in chordwise direction.

Because it is not necessary to capture the profile drag accurately, it was decided to use 80 panels for the simulation. To better capture the larger pressure gradients near the leading and trailing edge, a growth rate of 1.05 was applied there. This is also the number of cells Ahuja and Litherland used on a similar configuration [3].

**Spanwise mesh spacing** After doing the refinement study in chordwise direction, the same was done for the amount of nodes in spanwise direction. The number of chordwise cells was fixed at 80. The results of the refinement study are summarised in Table 4.3, and plotted in Figure 4.5.

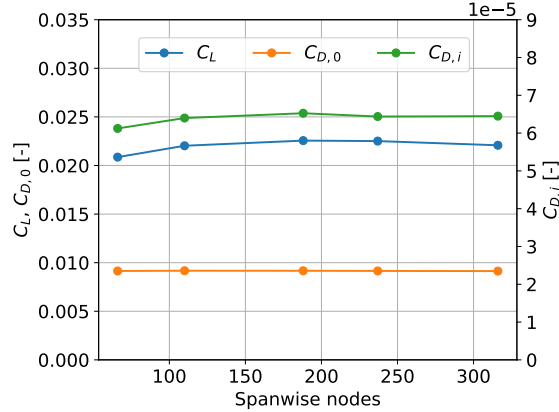


Figure 4.5: Evolution of lift, induced and profile drag for different numbers of nodes in spanwise direction.

When looking at the profile drag, it can be seen that it converges much better in spanwise direction than in chordwise direction. The reason for this is because Flightstream integrates the boundary layer equations along a streamline. Since the flow is largely in chord direction, the amount of spanwise cells has limited influence on this. Furthermore, there is no curvature in spanwise direction, hence the geometry can be represented accurately with relatively few nodes.

At 316 nodes, the error in lift and profile drag starts to increase. This is possibly because cells start to become too stretched. However the error in induced drag still reduces. It is not worth while to refine the mesh more than that as it would only increase numerical issues. As a result, it is decided to use the mesh with 316 nodes for the rest of the analysis.

Table 4.3: Lift, profile drag and induced drag for different numbers of spanwise nodes. The discretisation error for each mesh is given in the bottom rows.

Nodes	Mesh Convergence Study					Richardson Extrapolation	
	66	110	188	237	316	$\phi_0$	$P_{obs}$
$C_L$	0.0209	0.0220	0.0226	0.0225	0.0221	0.02239	0.43
$C_{D,0}$ [cts]	91.5	91.7	91.7	91.5	91.3	91.6	0.16
$C_{D,i}$ [cts]	0.61	0.64	0.65	0.64	0.64	0.65	1.28
$U_{C_L}$ [%]	9.8	3.3	2.3	2.0	3.0		
$U_{C_{D,0}}$ [%]	0.37	0.45	0.38	0.30	0.52		
$U_{C_{D,i}}$ [%]	7.6	2.3	1.8	1.5	1.3		

**Total Spatial Discretisation Uncertainty** Based on the mesh refinement study, the spatial discretisation error can be estimated for the initial validation wing. The chordwise and spanwise uncertainties are added together following Equation 4.10. A mesh with 80 chordwise and 316 spanwise nodes has a discretisation error of 4.5% in lift, 78.5% in profile drag and 4.58% in induced drag.

#### E. PROPELLER MESH REFINEMENT STUDY

In this section, the mesh settings for the propeller are obtained using a mesh refinement study. As for the wing, the chordwise and radial node distribution are done separately. In addition to finding the mesh den-

sity, the discretisation uncertainty is obtained. All results in this section come from unsteady simulations, performed at the same operating conditions as the initial validation case. The propeller blades were simulated in isolated conditions, without nacelle or spinner. Following [subsubsection C](#), a timestep of 0.001745s was used. The thrust and torque converged after 150 degrees of propeller rotation, so only 15 timesteps were needed.

**Chordwise Mesh Spacing** [Table 4.4](#) gives the results for the chordwise refinement study of the propeller, the amount of radial nodes was kept constant at 60. Both thrust and torque converge relatively well, although their orders of accuracy are relatively low. It was decided to use 30 nodes for the chordwise discretisation. This has an uncertainty error of around 5% for the thrust, which is considered acceptable. The error for the torque is much lower, at around 3%.

Table 4.4: Thrust and torque coefficient for different numbers of chordwise nodes. The extrapolated values, observed orders of accuracy and uncertainties for all meshes are given as well.

Nodes	Mesh Convergence Study				Richardson Extrapolation	
	15	30	60	120	$\phi_0$	$P_{obs}$
$C_T$	0.1624	0.1580	0.155	0.154	0.152	0.80
$C_Q$ [cts]	0.185	0.183	0.182	0.182	0.180	0.43
$U_{C_T}$ [%]	8.8	5.2	2.9	1.8		
$U_{C_Q}$ [%]	3.6	2.7	1.9	1.5		

**Radial Mesh Spacing** The mesh convergence study for the radial nodes is shown in [Table 4.5](#). Now the amount of chordwise nodes was fixed, at 30. For the radial spacing the thrust converged well, having an observed order of accuracy of 0.59. The torque converged much slower, having an order of accuracy of 0.06. However, the values are already close to the extrapolated value, hence the error is relatively small. It was decided to go with 60 radial nodes. Although this specific value was not part of the mesh refinement study, it was the amount of nodes used for the chordwise mesh refinement study. Using the results from the radial mesh convergence study, this would have a discretisation error of 3.69% for the thrust and 3.94% for the torque.

Table 4.5: Lift, profile drag and induced drag for different numbers of spanwise nodes. The discretisation error for each mesh is given in the bottom rows.

Nodes	Mesh Convergence Study				Richardson Extrapolation	
	10	20	40	80	$\phi_0$	$P_{obs}$
$C_T$	0.1643	0.1605	0.156	0.157	0.154	0.59
$C_Q$ [cts]	0.184	0.184	0.183	0.183	0.178	0.06
$U_{C_T}$ [%]	8.9	5.9	4.2	2.7		
$U_{C_Q}$ [%]	4.2	4.1	3.9	3.7		

**Total Spatial Discretisation Error** Combining the results of the chordwise and radial mesh convergence studies, the total discretisation error for thrust and torque can be calculated. The selected mesh consisting of 30 chordwise nodes, and 60 radial nodes. This led to a discretisation error of 6.4% for the thrust, and 4.8% for the torque.

## F. RESULTING MESH

Following the results of the mesh refinement study, the meshes for the wing and propeller were made. The meshes for the spinner and nacelle were much coarser. This is because the specific flowfield near these bodies is not of interest, as long as they impose the correct flowfield on the wing and propeller. Since disturbances die out with increasing distance in potential flows, it is not necessary to fully resolve the nacelle and spinner. The parameters used for the meshing are listed in [Table 4.6](#). For the spanwise nodes of the wing, no growth scheme was applied. Instead, the cells behind the propeller were made half the size of those outside the slipstream. The growth rates applied to the wing chord nodes and the propeller radial and chordwise nodes are all double-sided, meaning the growth rate is applied to both sides of the chord or span. In a panel method, the wake also needs to be meshed. The spanwise distribution of nodes in the wake follows directly from the

node distribution on the trailing edge of the wing, which sheds the wake. The streamwise panelling depends on the timestep. The wake is modelled as a free wake, so elements deform based on the local velocity. The panelling density in freestream direction thus depends on the local velocity. All the structured meshes (wing, nacelle and propeller) were given quadrilateral elements in Flightstream, the spinner consisted of triangular elements.

Table 4.6: Resulting mesh parameters for the initial validation in Flightstream.

wing		nacelle		propeller		spinner
nodes	growth rate	nodes	growth rate	nodes	growth rate	cell size
80 (chord)	1.0/1.05	40 (circ.)	1.0	30 (chord)	1.05	51 mm
320 (span)	N/A	40 (long.)	1.0	60 (radial)	1.05	unstruct.

In addition to selecting a suitable panel density for the wing mesh, the spatial discretisation error for the distributions of lift, pressure drag and friction drag was estimated. This was done by systematically coarsening the selected mesh (Table 4.6), in span- and chordwise direction. Smaller steps in mesh size were used compared to subsection D. The chordwise panel density varied from 50 to 80 nodes, the spanwise density from 238 to 316 nodes. Both used 4 different meshes. The discretisation error was estimated for the lift, pressure drag and friction drag distributions. The wing was divided into 250 equispaced stations. For each of these locations, the local lift and drag could be found by integration of  $C_p$  and  $c_f$  graphs. (Note that this is a different method than used for the mesh refinement study for the integral values, where the forces were obtained using the Kutta-Joukowski theorem.) The method from Eça and Hoekstra [15] (see subsection 4.1.3) was applied to each station to find the local discretisation error.

The spatial discretisation error bands for the different force distributions are superimposed on the solutions of the finest Flightstream mesh in Figure 4.6. For lift, the uncertainty is very small. There are some locations where it locally increases, such as around  $2 \cdot y/b = 0.2$ . These are caused by local oscillations in some of the meshes, which interferes with the least-squares fit. Adding more meshes might improve the behaviour, by reducing the weight of the individual meshes and oscillations in the fit. The pressure drag exhibits large error bands. This is due to the inherent difficulty of calculation pressure drag by surface integration, already mentioned in subsection 4.1.1. The friction drag has relatively small error bands, which do not vary noticeably across the span.

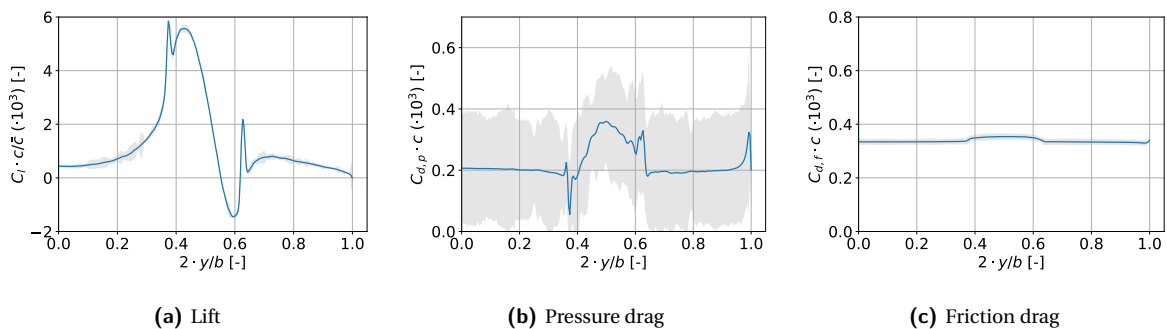


Figure 4.6: Uncertainty bands for the lift and pressure and friction drag

#### 4.2.2. CFD

A CFD simulation of the initial validation configuration was performed to validate Flightstream. This was done with unsteady RANS, ran with second-order upwind spatial discretisation. For temporal discretisation, a first-order implicit scheme was used. The timestep of 0.0001745s was chosen such that a step corresponds to one degree of propeller rotation. This is smaller than the two degrees per step used by [48]. The Spalart-Allmaras model was used to model turbulence. As a consequence, the boundary layer is turbulent everywhere. For the initial validation case, no formal mesh refinement study was done to estimate spatial discretisation error. Instead, the results for three different meshes are compared to verify that there are no significant differences between their lift and drag distributions. If the differences between these graphs are

much smaller than the difference with the results from the panel method, it is assumed that the CFD mesh density will not affect validation results.

### A. COMPUTATIONAL DOMAIN

The domain used for the CFD simulation is sketched in Figure 4.7. It consists of a quarter of a sphere with a radius of 100 times the chord of the wing, which equals 100 meter. The aft part of the sphere was extruded with the same length. This is 23 times the length of the model including nacelle, which is slightly smaller than the 25 body lengths recommended in the best practices document from Goetten et al. [18]. To achieve sufficient mesh refinement near regions of interest, several bodies of influence were defined. The first is a rectangular body completely enclosing the wing. Next, the wake of the propeller was refined in a cylindrical body, extending from the propeller up to 10 meters downstream of the wing quarter chord. This distance was chosen because the Flightstream simulations were ran for 42 iterations, in which the lift, drag and thrust reached steady state (they were oscillatory with constant amplitude and mean). Over these iterations, the wake convected 10m downstream. It was assumed that if the part of the wake further than 10m downstream does not significantly impact the wing and propeller in Flightstream, it is unlikely to do so in CFD. Hence, there is no point refining it beyond this distance. Finally, a body to capture the wing wake was made. It also extends downstream up to 10 meters from the quarter chord line. It has the same thickness as the wing everywhere except at the wingtip, where it is made bigger to encapsulate the wingtip vortex.

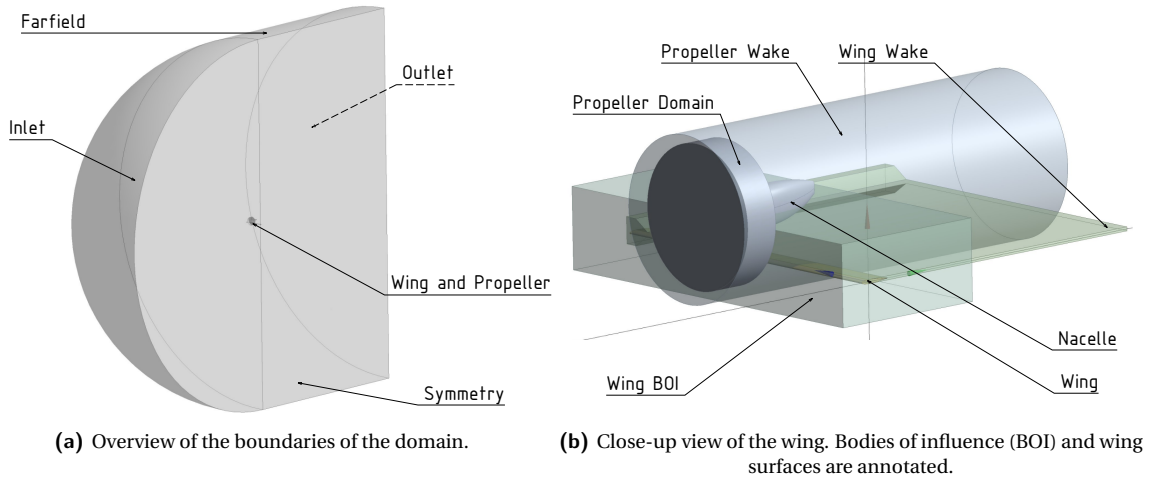


Figure 4.7: Computational domain for the CFD simulation of the initial validation case.

### B. MESHING

The meshes for the initial validation were made using Ansys Fluent meshing. While the walls and inflation layers are meshed with triangular and tetrahedral elements, the rest of the domain consists of a hexcore mesh. This allows using parallel computing, significantly reducing the time needed to construct a mesh. The propeller rotation was modelled using a sliding mesh. The rotating propeller domain and stationary external domain were meshed separately, and added together in the solver.

In order to capture the boundary layer well, an inflation layer was used at all no-slip walls. It consisted of 31 layers, and a growth rate of 1.3. A  $y^+$  value of 1 was used over the entire wing to resolve turbulence production in the boundary layer. In order to find the required height of the first cell of the inflation, the definition of  $y^+$  is applied (Equation 4.11). In order to solve it for  $y$ , the skin friction  $\tau_w$  is needed. This is obtained using Prandtl's one-seventh power law [35], see Equation 4.12. Note that this law is derived for a flat plate without pressure gradient. In a real wing, the presence of pressure gradients can locally increase the friction coefficient and thus require a lower  $y^+$  value.

$$y^+ = \frac{u_\tau}{\nu} y \quad \text{with} \quad u_\tau = \sqrt{\frac{\tau_w}{\rho}} \quad (4.11)$$

$$c_f = \frac{\tau_w}{\frac{1}{2} \rho_\infty V_\infty^2} = \frac{0.027}{Re_x^{1/7}} \quad (4.12)$$

Filling in the above equations, using the local Reynolds number at the trailing edge of the root of the wing yields a required cell height of 0.00523mm. While the skin friction at the trailing edge of the wing is generally

smaller than at the leading edge, using this spacing gave a  $y^+$  distribution below unity everywhere on the domain, except at the leading edge of the propeller blades, where it was slightly larger (order of 1.5). Since the boundary layer behaviour of the propeller itself is not of interest for this report, this was deemed acceptable.

Table 4.7: Mesh size settings in mm for the external domain.

	outside domain					
	wing wake	propeller wake	wing boi	nacelle, wing face size	interface face size	nacelle, wing curvature size
<b>coarse</b>	15	30	100	20	30	2
<b>intermediate</b>	12	24	80	16	24	2
<b>fine</b>	10	20	66	13	20	2

Table 4.8: Mesh size settings in mm for the mesh of the propeller domain.

	propeller domain				
	propeller face size	spinner face size	propeller, spinner curvature size	domain size	interface face size
<b>coarse</b>	20	30	1	30	30
<b>intermediate</b>	16	24	1	24	24
<b>fine</b>	13	20	1	20	20

The initial validation case was simulated on three different meshes. The sizing settings used to generate these are given in Table 4.7 and Table 4.8 for the external and propeller domain, respectively. The resulting mesh size and average lift, drag and thrust can be found in Table 4.9. The three meshes give very similar forces. For drag and thrust, the difference in integral forces are below 1% for all the meshes. In lift, there are slightly larger variations. Between the fine and intermediate mesh, the total lift differs by 2.1%, which is still relatively small. The lift and drag distributions are plotted in Figure 4.8. They agree well for the three different meshes. The differences in lift are negligible for most of the span, except near the maximum in lift at  $2 \cdot y/b = 0.45$ , where the intermediate mesh underestimates the peak in lift by 2%. The drag distribution is noisy, which is a result of the pressure integration method used to calculate it. The wing is divided in multiple sections, over which the  $C_p$  and  $c_f$  values are integrated. The pressure drag is only a very small component of the pressure force acting on a wing mesh cell. Depending on where the cells are located, they have a different slope, which leads to a slightly different pressure drag. To conclude, the differences between the three meshes are very small, making it suitable for validating Flightstream.

Table 4.9: Lift, drag and thrust for the different meshes. All forces are averaged over 60 degrees of propeller rotation.

	coarse	intermediate	fine
<b>Million cells</b>	63.8	145.5	158.6
<b><math>C_L</math> [-]</b>	0.0278	0.0275	0.0280
<b><math>C_D</math> [cts]</b>	94.3	94.3	94.4
<b><math>C_T</math> [-]</b>	0.201	0.201	0.201

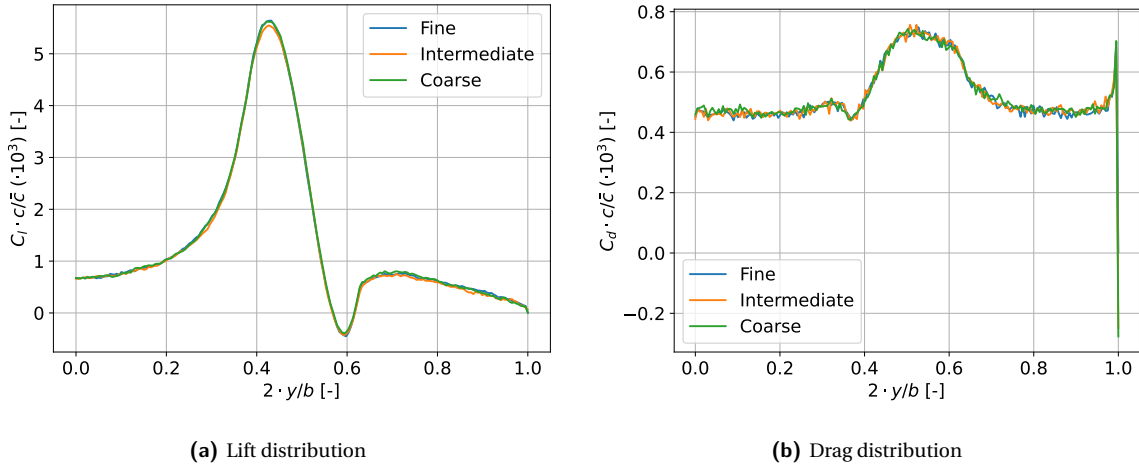


Figure 4.8: Lift and drag distributions for the three different CFD meshes.

### 4.3. STRUT-BRACED WING

In this section, the computational setup for the strut-braced wing is presented. As in the previous section, first a mesh refinement study is done in Flightstream. This is presented in [subsection 4.3.1](#). Next, the setup for the CFD simulation is treated in [subsection 4.3.2](#). A more formal mesh refinement study is done there, estimating the spatial discretisation uncertainty.

#### 4.3.1. FLIGHTSTREAM

Contrary to the initial validation case, the strut-braced wing consists of several elements of interest (wing, strut and jury strut). For the wing and main strut, a mesh refinement study was done for the isolated element, see [subsubsection A](#) and [subsubsection B](#) respectively. This was not done for the jury strut, which was instead given the same mesh spacing as the main strut. After refining the elements separately, they were put together, and the refinement study was redone for each element to estimate the discretisation error for the force distributions. For this, smaller changes in mesh density were used. The procedure for this is outlined in [subsubsection C](#), along with the resulting mesh density.

#### A. WING MESH REFINEMENT

First the number of chordwise nodes was varied. This was done while keeping the number of spanwise nodes constant at 161. The lift, induced and profile drag for each mesh are given in [Table 4.10](#). Using Richardson extrapolation, the values on an infinitely refined mesh are estimated. These values are used to find the discretisation uncertainty on each mesh. Similar to the initial validation, the lift and induced drag converged well, and have a low discretisation error. The profile drag is not converged yet at 80 nodes. Because the lift and induced drag are most important, it was decided to use 80 chordwise cells for the wing, with a growth rate of 1.05 on the leading and trailing edges of the wing.

Table 4.10: Lift, profile drag and induced drag for different numbers of chordwise nodes on the wing. The extrapolated values, using the method from [15] are also given, together with the discretisation uncertainty for each mesh.

Nodes	Mesh Convergence Study						Richardson Extrapolation	
	5	10	20	30	40	80	$\phi_0$	$\mathbf{P}_{\text{obs}}$
$\mathbf{C}_L$	0.352	0.376	0.379	0.382	0.388	0.389	0.388	1.31
$\mathbf{C}_{D,0}$ [cts]	27.0	42.3	59.1	71.9	78.9	86.7	310.5	0.12
$\mathbf{C}_{D,i}$ [cts]	51.9	46.6	42.6	41.5	42.0	42.0	41.2	1.36
$\mathbf{U}_{C_L}$ [%]	12.5	4.6	3.8	2.8	0.96	1.4		
$\mathbf{U}_{C_{D,0}}$ [%]	114.5	108.4	101.6	96.5	93.6	90.5		
$\mathbf{U}_{C_{D,i}}$ [%]	34.3	18.0	6.1	2.7	4.3	4.2		

Similarly, the number of spanwise nodes was varied (see [Table 4.11](#)). The chordwise nodes were selected

based on the results of the chordwise study above. The selected number of spanwise cells is 161, which gives a good balance between accuracy and computational cost. The junction regions (nacelle-wing and strut-wing) are given a node spacing half the size of the rest of the wing, to capture any interference effects and the gradients due to the propeller slipstream.

Table 4.11: Lift, profile drag and induced drag for different numbers of spanwise nodes on the wing, together with extrapolated values and uncertainties.

Nodes	Mesh Convergence Study					Richardson Extrapolation	
	79	107	161	215	271	$\phi_0$	$\mathbf{P}_{obs}$
$C_L$	0.385	0.388	0.391	0.393	0.393	0.397	0.55
$C_{D,0}$ [cts]	96.1	94.6	93.1	91.8	90.4	82.5	1.53
$C_{D,i}$ [cts]	40.5	41.1	42.1	42.5	42.7	43.9	0.47
$\mathbf{U}_{C_L}$ [%]	3.9	3.0	1.7	1.3	1.2		
$\mathbf{U}_{C_{D,0}}$ [%]	21.0	18.7	16.5	14.5	12.4		
$\mathbf{U}_{C_{D,i}}$ [%]	10.1	8.3	5.4	4.5	3.8		

### B. STRUT MESH REFINEMENT

The results of the chordwise mesh refinement of the strut are given in Table 4.12. Lift, induced and profile drag converge almost monotonically. At 40 nodes, the lift and induced drag are converged sufficiently well, so it is decided to use this amount of nodes, again with a growth rate of 1.05 at both ends. In fact, the discretisation error for lift and induced drag is lowest at 40 nodes. This may be because the error increases when cells are stretched too much.

Table 4.12: Chordwise mesh refinement of the strut, together with extrapolated values and uncertainties.

Nodes	Mesh Convergence Study					Richardson Extrapolation	
	5	10	20	40	80	$\phi_0$	$\mathbf{P}_{obs}$
$C_L$	0.0171	0.0210	0.0228	0.0233	0.0233	0.0236	0.024
$C_{D,0}$ [cts]	5.0	7.6	11.0	13.5	15.1	28.8	8.2
$C_{D,i}$ [cts]	0.61	0.65	0.66	0.65	0.64	0.65	2.11
$\mathbf{U}_{C_L}$ [%]	35.0	14.2	4.8	2.1	2.1		
$\mathbf{U}_{C_{D,0}}$ [%]	104.8	93.6	78.6	67.9	60.7		
$\mathbf{U}_{C_{D,i}}$ [%]	9.7	2.0	4.4	2.2	4.3		

In spanwise direction, there was relatively little variation of the different force components when varying the amount of nodes. The results are given in Table 4.13. The regions close to the wing-strut and strut-jury strut junctions are refined by a factor of 2 compared to the rest of the wing. It is decided to use 160 spanwise nodes. Beyond this, the error increases again for lift and induced drag.

Table 4.13: Spanwise mesh refinement of the strut.

Nodes	Mesh Convergence Study					Richardson Extrapolation	
	40	63	102	164	260	$\phi_0$	$\mathbf{P}_{obs}$
$C_L$	0.0229	0.0230	0.0231	0.0232	0.0232	0.0232	11.7
$C_{D,0}$ [cts]	13.1	13.1	13.1	13.1	13.1	12.5	0.12
$C_{D,i}$ [cts]	0.63	0.63	0.64	0.65	0.64	0.65	0.30
$\mathbf{U}_{C_L}$ [%]	1.8	1.3	0.75	0.37	0.48		
$\mathbf{U}_{C_{D,0}}$ [%]	6.3	6.3	6.4	6.2	5.6		
$\mathbf{U}_{C_{D,i}}$ [%]	5.1	3.8	2.8	0.9	1.9		

### C. RESULTING MESH AND UNCERTAINTY ESTIMATION

The mesh resulting from the mesh convergence study is summarised in Table 4.14. The nacelle and spinner have a different kind of mesh than the initial validation. They are unstructured, which makes it easier to connect the nacelle mesh with the wing and jury strut. The propeller mesh was not changed, and can be found in Table 4.6.

Table 4.14: Resulting mesh parameters for the strut-braced wing in Flightstream. c stands for chordwise, s for spanwise.

wing		strut		jury strut		nacelle/spinner	
nodes	refinement	nodes	refinement	nodes	refinement	cell size	refinement
80 (c)	1.05 growth	40 (c)	1.05 growth	30 (c)	1.05	100mm	matches mesh of jury at junction curvature refinement
157 (s)	2X refined at junctions	164 (s)	2X refined at junctions	30 (s)	1.05		

For the uncertainty estimation, the number of nodes on each element was reduced to roughly two thirds of the selected amount of nodes in four steps. The resulting amount of nodes for each element is given in Table 4.15. While varying one parameter, all the other were kept constant. The error associated with chordwise and spanwise spacing where calculated according to subsection 4.1.3.

Table 4.15: Number of nodes used in spanwise and chordwise direction for each element to estimate the discretisation uncertainty.

wing		strut		jury strut	
span	chord	span	chord	span	chord
97	50	114	25	21	21
118	60	132	30	24	24
139	70	148	35	27	27
157	80	164	40	30	30

The resulting error bands are shown in Figure 4.9. For the wing, the error bands for lift are relatively wide, especially inboard of the strut-wing junction. Also in pressure drag there is a region with a relatively large error band, around  $2 \cdot y/b = 0.75$ . This is likely caused by the transition from quadrilateral to triangular elements at the trailing edge of the wing. This is done automatically in Flightstream, and causes some oscillations in induced drag. It is illustrated in Figure 4.10. The error bands for the strut are much less significant. The jury strut has large bands in pressure drag, which is caused by surface integration. The low number of chordwise cells makes this method relatively unreliable.

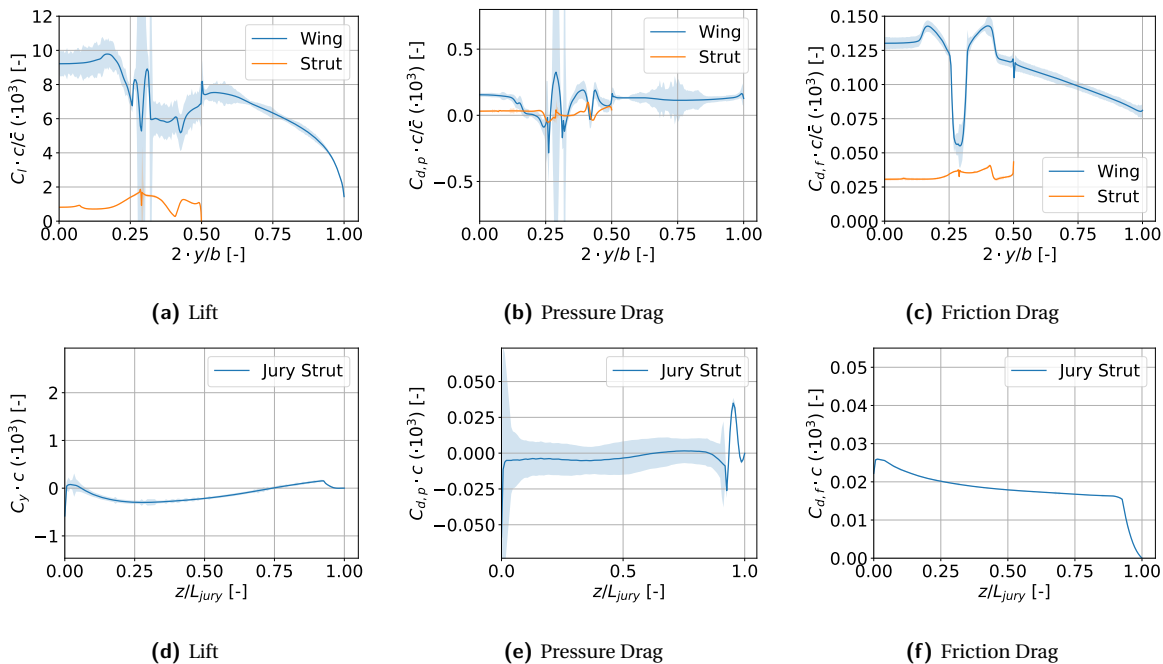


Figure 4.9: Discretisation error for the local lift, pressure drag and friction drag.

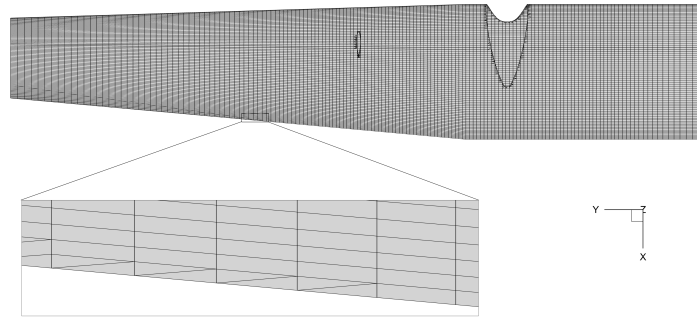


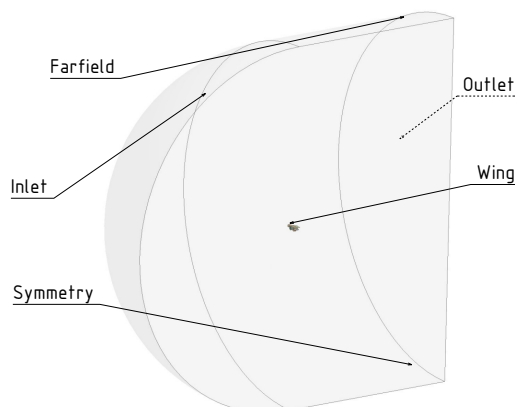
Figure 4.10: Transition from quadrilateral to triangular mesh faces at the trailing edge of the wing.

### 4.3.2. CFD

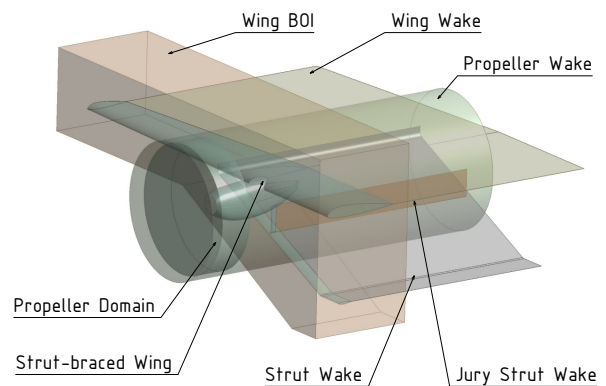
The setup for the CFD simulations of the strut-braced wing are presented here. The computational domain and refinement regions are treated in [subsubsection A](#). Contrary to the initial validation, a formal mesh refinement study is performed. The different mesh settings and discretisation errors are presented in [subsubsection B](#).

#### A. COMPUTATIONAL DOMAIN

The CFD domain of the strut-braced wing is shown in [Figure 4.11](#). It is similar to that of the initial validation case. The spherical part has a radius of 100 times the wing root chord. The cylindrical part has the same length, see [Figure 4.11a](#). Again, some refinement regions were added to capture all relevant flow phenomena near the wing. Refinement bodies for the wakes of the wing, strut, jury strut and propeller were extruded 10 m downstream. In addition, a body of influence was added around the entire strut-braced wing. The refinement regions are displayed in [Figure 4.11b](#).



(a) Overview of the boundaries of the domain.



(b) Close-up view of the strut-braced wing, including bodies of influence.

Figure 4.11: Computational domain for the CFD simulation of the strut-braced wing.

#### B. MESHING

The CFD meshes for the strut-braced wing were made in the same way as those for the initial validation case. Since the CFD results for the strut-braced wing are of interest for answering the research questions, more effort was put into quantifying the discretisation errors. For this reason, the strut-braced wing mesh was systematically refined 5 times. Following Roache [37], the inflation layer was kept constant at 31 layers, with a fixed first layer height of 0.005mm and a 1.3 growth rate. The mesh settings for the 5 different meshes are given in [Table 4.16](#). Those for the external domain can be found in [Table 4.17](#). A simulation of the same configuration without propeller was also performed. No mesh refinement study was done for this configuration. Instead, the settings for the M5 mesh were reused, but without propeller.

Table 4.16: Sizing settings in mm for the mesh of the propeller domain.

	propeller					
	propeller face size	propeller curvature size	spinner face size	spinner curvature size	domain size	interface face size
<b>M1</b>	20	2	20	4	40	40
<b>M2</b>	17.5	1.75	17.5	3.5	35	35
<b>M3</b>	15	1.5	15	3	30	30
<b>M4</b>	12.5	1.25	12.5	2.5	25	25
<b>M5</b>	10	1	10	2	20	20

Table 4.17: Mesh size settings for the external domain, given in mm.

	outside domain					
	wing wakes	propeller wake	wing boi	nacelle, wing, strut jury face size	interface face size	nacelle, wing, strut curvature size
<b>M1</b>	20	40	150	80	40	2
<b>M2</b>	17.5	35	131.25	70	35	1.75
<b>M3</b>	15	30	112.5	60	30	1.5
<b>M4</b>	12.5	25	93.75	50	25	1.25
<b>M5</b>	10	20	75	40	20	1

The size of the different meshes and the lift and drag averaged over 60 degrees of propeller rotation are shown in Table 4.18. A grid convergence study was done for the 5 grids, using the method of Eça and Hoekstra [15]. It was done for both the integral lift and drag of the entire strut-braced wing, and the distributions of lift, pressure drag and friction drag. The results of the refinement study for the integral lift and drag are plotted in Figure 4.12, and are tabulated in Table 4.18. Superconvergence in lift is detected, meaning that the observed order of accuracy is higher than the theoretical order of accuracy (2 in this case). This leads to an error band relatively large compared to the values encountered during the convergence study, even though the lift looks well converged. Also note the small range in  $C_L$  on the y-axis, indicating that the error is small in absolute numbers. The convergence in drag is less clear than that for the wing. The observed order of accuracy is closer to the theoretical value, leading to the smaller error band.

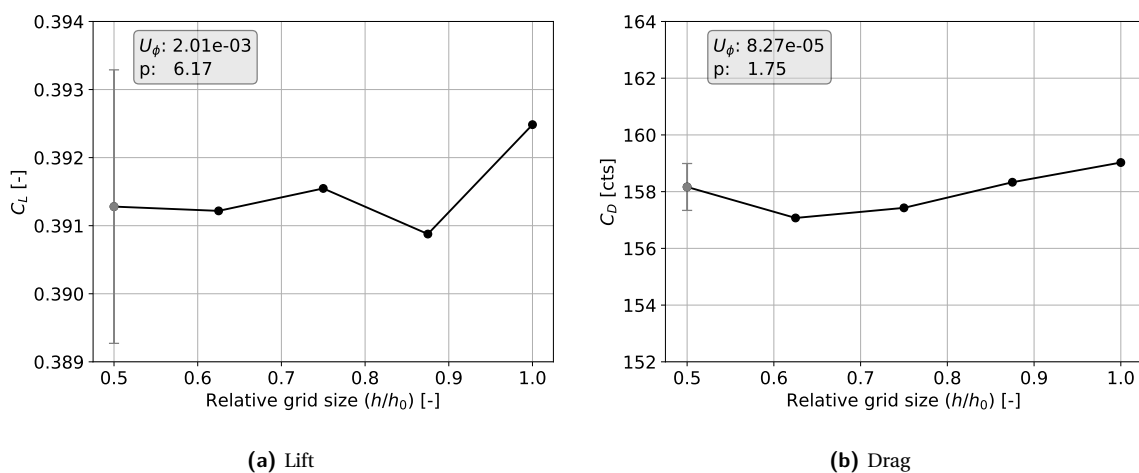


Figure 4.12: Discretisation error in lift and drag for the finest grid (M5). The uncertainty and observed order of accuracy are given in the text box.

Table 4.18: Average lift, drag and thrust for the different meshes. Extrapolated values ( $\phi_0$ ), observed order of accuracy ( $p_{obs}$ ) and fitting constant for the error ( $\alpha$ ) are given as well, together with the discretisation error  $U_\phi$ .

mesh name	M1	M2	M3	M4	M5	$\phi_0$	$p_{obs}$	$\alpha$	$U_\phi$
<b>Cells (Millions)</b>	43.2	53.89	59.91	81.01	115.76				
<b>Average <math>C_L</math> [-]</b>	0.3924	0.3908	0.3916	0.3912	0.3912	0.3914	6.17	0.0006268	0.5134%
<b>Average <math>C_D</math> [cts]</b>	159.0262	158.3	157.4	157.1	158.2	157.8	1.75	0.001004	0.5239%

The error bands are plotted over the lift and drag distributions for the wing and strut in Figure 4.13. The discretisation error for the lift distributions is very low, while that for the pressure drag is significantly higher. Pressure drag consists of induced drag, viscous drag and wave drag, although the last is likely very small since no shockwaves were observed. Given the low error bands of the wing lift distribution, it is unlikely that the error in the pressure drag comes from induced drag. Instead, it may originate from viscous drag or from a too coarse surface mesh. Given the low error of the friction drag, it is more likely to be caused by the latter.

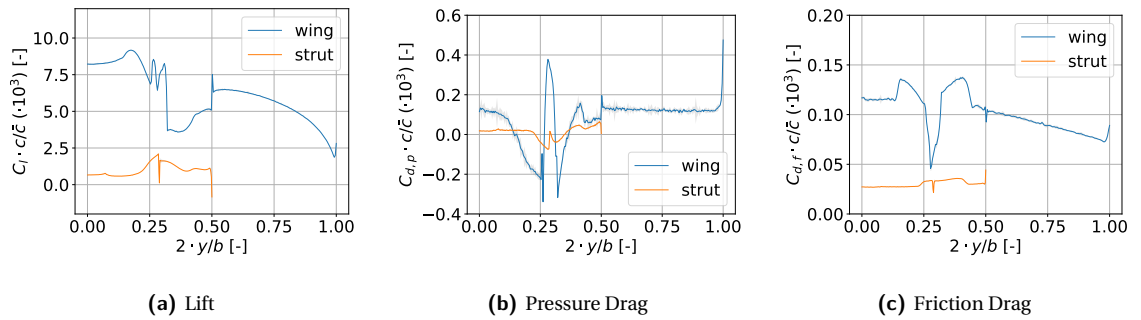


Figure 4.13: Uncertainty bands for the lift and drag distributions of the wing and strut.

The error bands for the jury strut are shown in Figure 4.14. The discretisation error in side force is small everywhere except near the strut-jury strut junction. The pressure and friction drag also exhibit larger errors around this region. The flow around this junction is very complex, there is the junction flow combined with the increased velocity due to the propeller slipstream. This possibly requires a very fine grid.

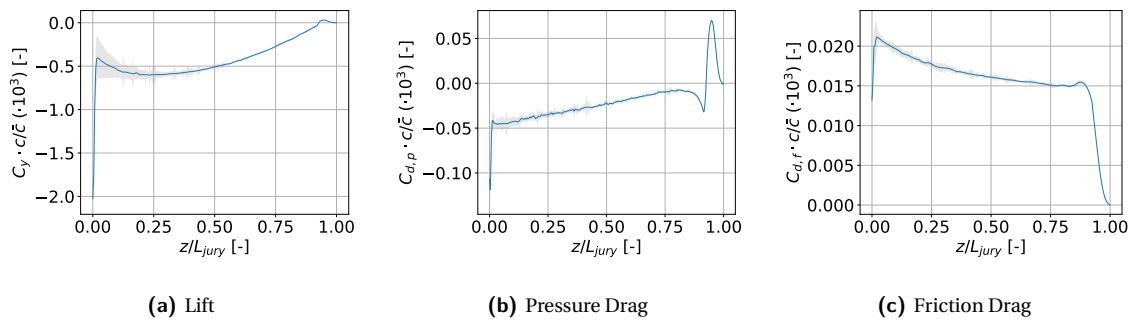


Figure 4.14: Uncertainty bands for the lift and drag distributions of the jury strut.

# 5

## VALIDATION

In this chapter, the results obtained by Flightstream are validated with RANS. First, the propeller modelling in Flightstream is validated with CFD in [section 5.1](#). Next, the simplified initial validation case is considered in [section 5.2](#). It consists of a propeller and nacelle mounted above a straight wing. The goal of this validation is to check whether Flightstream can capture some of the fundamental mechanisms thought to have an influence on the aerodynamics of a propeller-powered strut-braced wing. The validation is done by comparing lift, drag and pressure distributions. The real strut-braced wing geometry is validated in [section 5.3](#). The goal of this second validation is to confirm the results of the initial validation, and is done less in-depth. Only lift and drag distributions are compared for the different elements of the strut-braced wing (wing, strut and jury strut).

The lift and drag distributions in this section are obtained using integrated surface pressures. This method is known to be inaccurate, especially for the calculation of induced drag [\[42\]](#). However, surface pressure and friction data is available for both Flightstream and CFD results. For validation, it is considered better to analyse both cases with the same method. If the lift distribution and pressure drag distribution found by surface integration agree well with the CFD results, it is assumed that the induced drag found by Flightstream will be accurate as well. When analysing the Flightstream results in [chapter 6](#), the Kutta-Joukowski theorem will be applied to eliminate the errors associated with surface pressure integration.

### 5.1. PROPELLER MODELLING

As mentioned before, the propeller was modelled using the mean camber line of the airfoil sections. This is essentially the same as using a vortex lattice method. It was considered acceptable, as the propeller itself is not of interest for the present research. Only its influence on the wing should be accurate. To verify whether this is the case, the thrust and power distributions of an isolated XPROP was used as a metric. If these are accurate, it means that the vorticity distribution in the wake is similar to the real propeller, and so should be the induced velocities. The comparison was made between two propeller modelling options in Flightstream, namely the VLM propeller and a propeller of which the full blade was meshed. The actuator disk was not considered. In addition, a CFD simulation was done with the same propeller configuration, to validate Flightstream itself.

The integral values for thrust and torque coefficients are listed in [Table 5.1](#). Both modelling methods in Flightstream predict a higher thrust than CFD. The difference is the largest for the full blade propeller, at 11%. The VLM blade is slightly more accurate at 10%. The torque coefficient is more accurate. It is underestimated by 2% by the VLM blade, and less than 1% for the full blade.

Table 5.1: Integral thrust and torque coefficients for the different propeller models

	VLM Blade	Full Blade	CFD
$C_T$	0.199	0.208	0.178
$C_Q$	0.048	0.050	0.051

The comparison between the local thrust and torque distributions is shown in [Figure 5.1](#). In the case of thrust, The VLM and full blade propellers are accurate for the inboard part of the propeller, but overestimate the maximum local thrust by 23% and 30%, respectively. The full blade and VLM agree well, their maximum thrusts are within 6%. For the local torque, Flightstream underestimates it on the inboard part of the blade by a relatively constant value of 0.01, except near the tip. Again, the maximum torque is overestimated, by 6% for the VLM blade and 12% for the full blade. The underestimation at the inboard part cancels out the peak at the tip for both modelling options in Flightstream. This is why the integral values are more accurate.

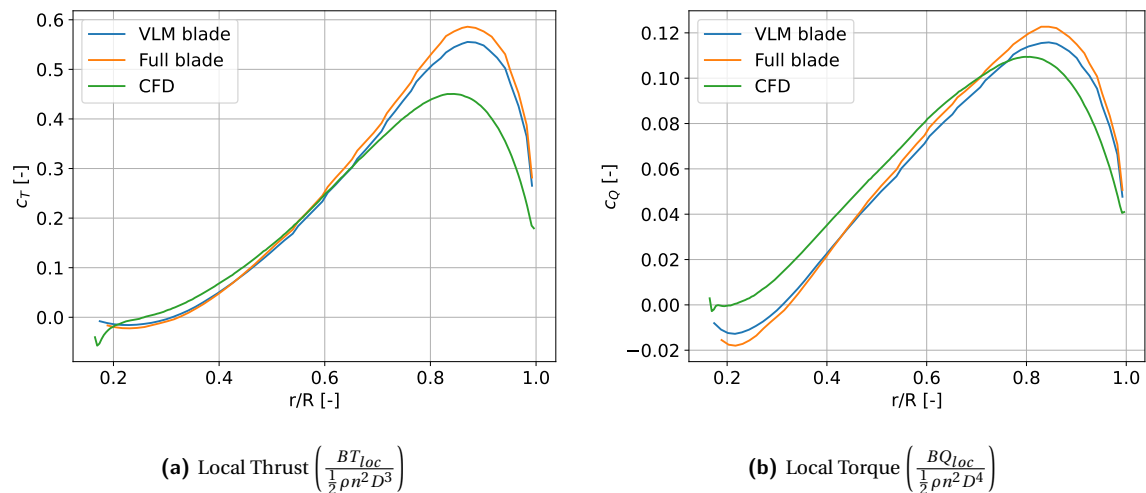


Figure 5.1: Comparison of thrust and torque distribution of the isolated XPROP propeller using different modelling methods.

As an additional validation tool, the propeller wakes simulated in CFD and Flightstream are visualised in [Figure 5.2](#), based on the vorticity. The figure for CFD has contour lines for the vorticity in Flightstream added, for easier comparison. The tip vortex locations agree well between CFD and Flightstream. The shape of the blade wakes is harder to compare, although the locations seem to be accurate. In the CFD simulations, they have been diffused too much to make out their shape clearly. This also happened to the tip vortices. The absence of (numerical) diffusion in Flightstream leads to a much more defined wake shape there. The concentration of vorticity in the Flightstream propeller wake leads to some peaks in lift and drag when adding a wing in the slipstream, as will be explained later.

Another conclusion based on the wake of the isolated propellers is that the slipstream contraction is very limited. For the Flightstream simulation, the radius of the slipstream reduces by 0.6% over a distance of 4 propeller radii downstream. It was initially thought that slipstream contraction would increase the angle of attack of a wing or strut mounted below a propeller, and so tilt the lift vector forward and reduce the induced drag. With such a small contraction in the slipstream, this effect will likely have a negligible influence on the lift of the wing.

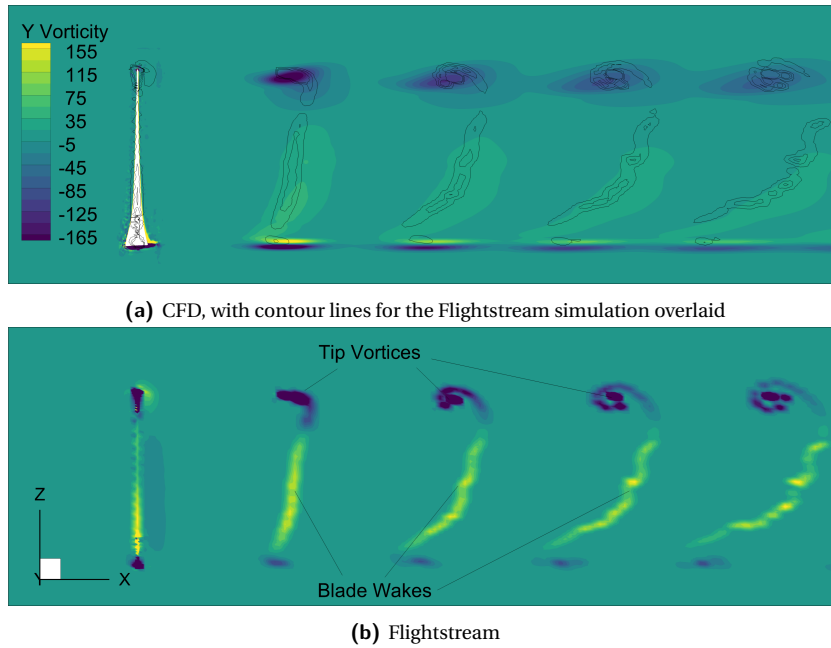


Figure 5.2: Visualisation of the wake of the isolated propeller. The CFD simulation has been ran for 360 degrees of propeller rotation. Only the upper half of the wake system is shown, the sections have been taken at the propeller centerline. The freestream is aligned with the positive X-axis.

## 5.2. INITIAL VALIDATION

Flightstream is validated with RANS using the initial validation geometry described in [subsection 3.3.2](#). The mesh used for the Flightstream simulation is that resulting from the mesh convergence study, see [Table 4.6](#). First, the lift and drag are validated in [subsection 5.2.1](#). Next, in section [subsection 5.2.2](#), the pressure distribution obtained by Flightstream is validated. The pressure distribution at the wing surfaces is compared, as well as  $C_p$  plots at different stations along the wing. Additionally, the  $c_f$  distribution on one of these sections is considered.

### 5.2.1. LIFT AND DRAG

The most important indicators of the aerodynamic performance of an aircraft are the lift and different components of the drag. In this section, the lift and drag obtained by Flightstream are validated. This is done by first looking at the integral values for lift, drag and thrust in [subsubsection A](#). Next, the distributions of lift, pressure drag and friction drag are compared with a CFD simulation in [subsubsection B](#).

#### A. AVERAGE LIFT AND DRAG

The average lift, drag and thrust coefficients for the initial validation are shown in [Table 5.2](#). The Flightstream values have been obtained by application of the Kutta-Joukowski theorem, whereas the CFD results come from surface integration. In both cases, they are the averages from 60 degrees of propeller rotation.

Flightstream estimates both lift and drag with roughly 10 percent accuracy. The discretisation uncertainty for lift was calculated at 4.5% for the Flightstream simulations, indicating that the difference observed here has other origins, such as modelling errors. The drag has a very large uncertainty in Flightstream due to the inaccuracy in profile drag. Still, given that the CFD and Flightstream results agree rather well, it is possible that the discretisation error in profile drag was overestimated. As will be shown later, the different drag components differ slightly more than 8.16%, but overestimates the pressure drag and underestimates the friction drag, thus partially cancelling out the error. The thrust is more different from the CFD simulation. There are multiple possible explanations for this. First, the propeller blades are modelled by their camber line alone in Flightstream, as opposed to the full blade geometry used for the CFD simulations. This introduced an error in thrust of 10%, as shown in [section 5.1](#). Second, the discretisation error of the Flightstream propeller was estimated at 6.4%, which could have contributed to the discrepancy. Finally, since the error in propeller thrust is larger here than for the isolated propeller, it is possible that the effect of the nacelle and spinner on the

propeller are not simulated well in Flightstream. This may have been caused by the small gap between the stationary spinner and rotary blades in the panel code, or the inability of it to capture junction flow effects. These are only present when the nacelle and spinner are added to the simulation.

Table 5.2: Lift, drag and thrust coefficients averaged over 60 degrees of propeller rotation.

	CFD	Flightstream	Difference [%]
$C_L$ [-]	0.0277	0.0246	-12.6%
$C_D$ [cts]	94.5	87.3	-8.16%
$C_T$ [-]	0.183	0.229	20.3%

## B. LIFT AND DRAG DISTRIBUTIONS

The distributions of lift, friction drag and pressure drag of the initial validation wing are shown in Figure 5.3. The lift distributions of Flightstream and the CFD simulation agree well. Overall, the lift from CFD is higher than that from Flightstream, which is consistent with the integral values given earlier. In addition, the Flightstream lift distribution exhibits peaks in lift at 37% and 63% of the span. These may be caused by the tip vortices of the propeller wake. In Flightstream, they pass through the wing without being attenuated by (numerical) diffusion or interactions with the wing boundary layer. The velocity induced by a vortex in a panel method goes to infinity when approaching its core. A real, viscous vortex does not exhibit this behaviour and has zero velocity at its core. The more smoothed vortices in CFD do not induce large pressure gradients as Flightstream does. As a result, the lift distribution is smoother.

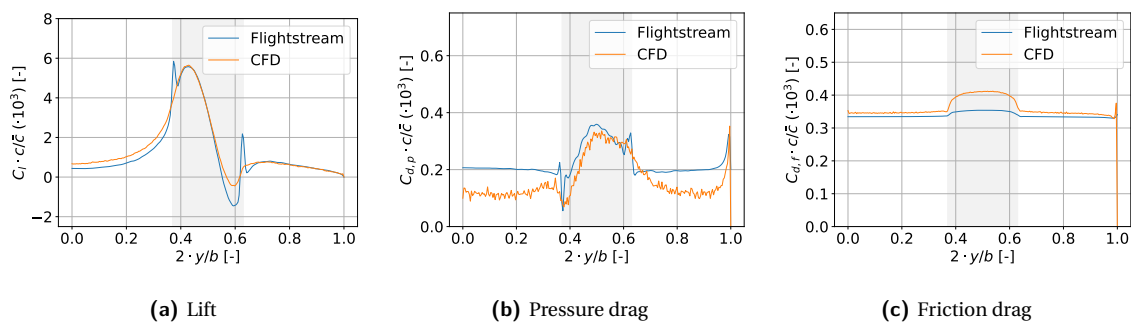


Figure 5.3: Comparison between CFD and Flightstream. The blue error bands represent the discretisation error in Flightstream. The region of the wing submerged in the slipstream is marked in grey.

The pressure drag is compared in Figure 5.3b. Here, Flightstream overestimates it everywhere except in the slipstream. The pressure drag was found to be rather sensitive to the chordwise spacing, see the large error bands in Figure 4.6b. This is because it is calculated by integrating the surface pressures. According to Smith and Kroo [42] induced drag is very sensitive to panel density and angle of attack when using surface integration. The Flightstream mesh is coarser than the CFD mesh, and thus relatively inaccurate for pressure drag calculations. However, since the lift distributions agreed closely, the induced drag and thus pressure drag should be very close as well. For this reason it is decided that the differences in pressure drag are mostly due to errors in integration in post-processing. For the actual analysis, the Kutta-Joukowski theorem will be applied for the induced drag in Flightstream. For friction drag (Figure 5.3c), there is a slight difference in behaviour between Flightstream and CFD in the wing portion submerged in the propeller slipstream, where Flightstream underestimates the friction.

### 5.2.2. PRESSURE DISTRIBUTIONS

In this subsection, the pressure distributions obtained from Flightstream are validated. First, the isobars of the wing are compared in subsection A. This is followed by a comparison of  $C_p$  plots at several locations on the wing in subsection B. Additionally, this includes a  $c_f$  plot to validate both CFD and Flightstream.

#### A. SURFACE PRESSURE

In Figure 5.4, the pressure contours for the upper and lower sides of the initial validation wing are compared. The behaviour of Flightstream and CFD is largely similar. Flightstream predicts the pressure peaks in the slip-

stream at the correct location, and with the correct magnitude. However, there is a more pronounced border between the part of the wing inside the slipstream and the part outside of it. This is consistent with the lift and pressure drag distribution (Figure 5.3), where large peaks are observed at the edge of the propeller slipstream. In addition, it seems like the lower pressure regions on the Flightstream wing are slightly larger than those in CFD. This could point at a higher slipstream velocity, which is not inconceivable, given that Flightstream estimated a 20.3% higher propeller thrust than CFD. Outside the propeller slipstream, Flightstream and CFD agree almost perfectly. Using actuator disk theory, the slipstream velocity would increase by 0.6% due to the higher thrust found in Flightstream. This is very limited, and might not be the reason for the offset in pressure.

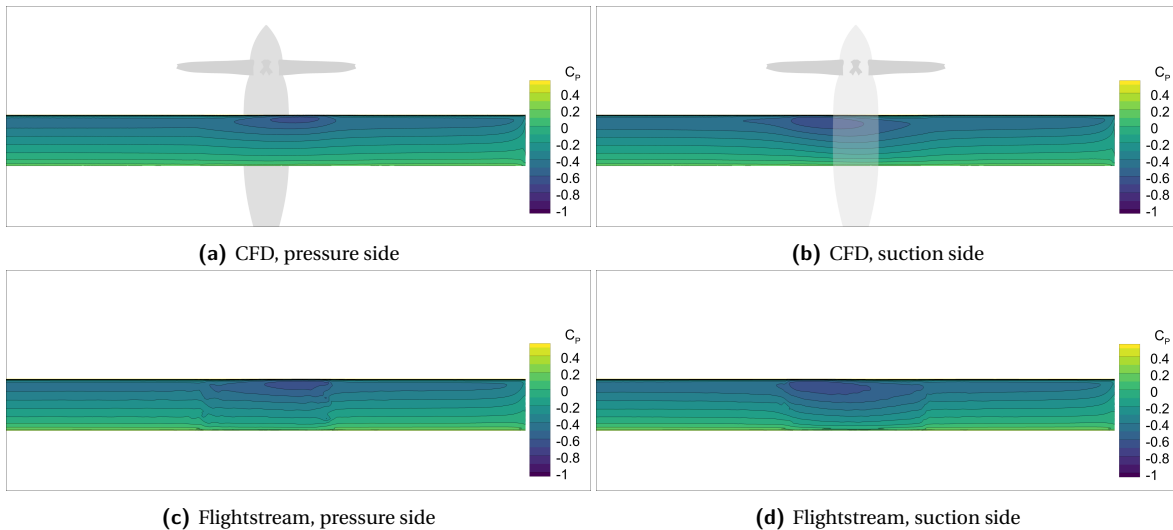


Figure 5.4: Wing pressure contours. The nacelle and propeller have been drawn in the CFD plots to visualise the location of the propeller slipstream.

### B. PRESSURE AND SKIN FRICTION PLOTS

The pressure contours in Figure 5.4 provided a qualitative validation of the pressure distribution of the initial validation wing. It was suspected that Flightstream overestimated the pressures inside the slipstream. To verify this, plots have been made of the pressure distribution along several spanwise stations.

First, the pressure distribution was obtained outside the slipstream, near the center of the wing. In addition to comparing CFD with Flightstream, an XFOIL simulation was done as well. It was done at a Reynolds number of 5.4 million, and an N factor of 9. Since the location on the wing is far enough from the propeller slipstream, the flow at that station should be mostly 2D. Indeed, it can be seen that the three methods agree very well (Figure 5.5a). Since the pressures predicted by XFOIL agree so well with CFD, it is assumed that the flow is indeed predominantly 2D. This allows using XFOIL to verify the turbulence modelling used in CFD. It has already been proven to be at least as accurate as CFD in predicting single element airfoil aerodynamics, such as pressure and skin friction distributions [32] [38]. The goal of this verification is to check whether the mesh was sufficiently refined near the surface to properly capture the boundary layer. It is done by comparing the skin friction coefficient of XFOIL with that of CFD and Flightstream, although the latter is of limited interest. To be consistent with the fully turbulent boundary layer in CFD and Flightstream, the transition point in XFOIL was fixed at the leading edge. The results are shown in Figure 5.5b. Apart from a peak not captured at the leading edge, the CFD simulation agrees well with XFOIL. Flightstream is slightly more different, but still reasonably accurate.

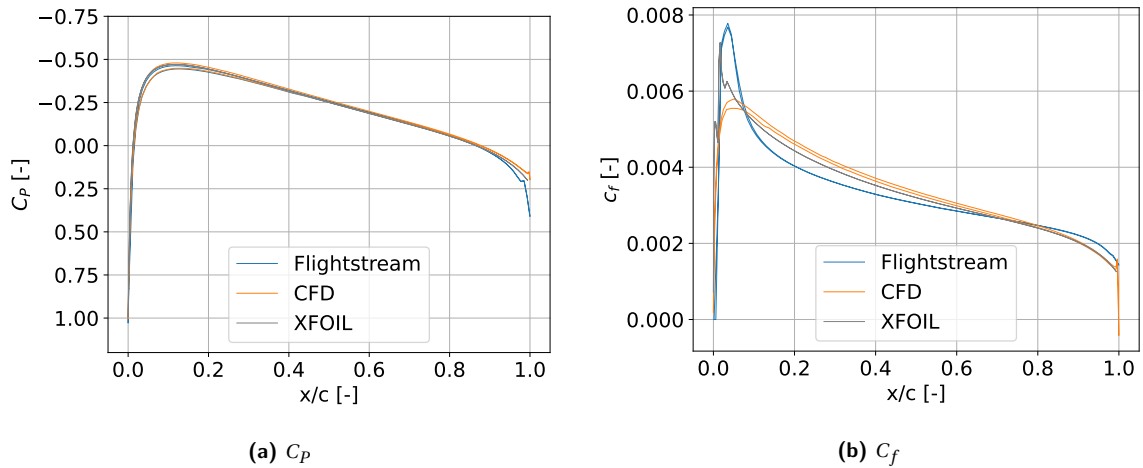


Figure 5.5: Pressure and skin friction plots outside the propeller slipstream, at  $2 \cdot y/b = 0.1$ .

Figure 5.6 shows pressure plots at two stations on the wing within the propeller slipstream, 1 meter on each side of the propeller. Here the difference between CFD and Flightstream is much bigger than outside the slipstream. Flightstream overestimates the magnitude of the pressure. As mentioned before, this may be caused by a higher slipstream velocity than the CFD simulation. Even though the Flightstream plots are shifted upwards, they still have roughly the same area within the  $C_p$  plots as CFD, which is why the lift distribution is so similar in Figure 5.3a.

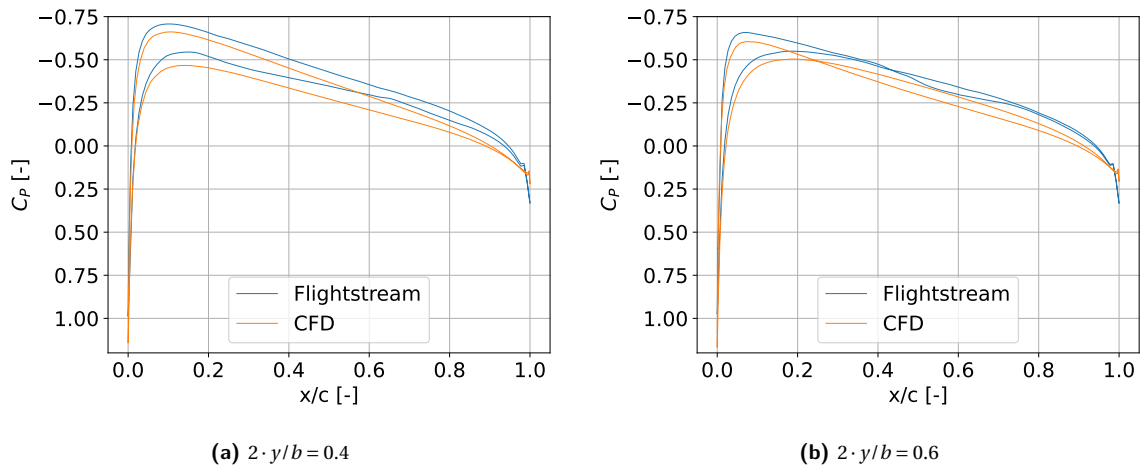


Figure 5.6:  $C_p$  plots at different location of the span of the initial validation configuration

### 5.2.3. DISCUSSION OF RESULTS

One of the goals of the initial validation case was to find out whether Flightstream is able to capture all relevant flow phenomena. This is discussed in subsection A, based on the validation results presented earlier. Previously, the method of validation was already outlined. CFD force distributions are compared with those of Flightstream, based on surface integration. For later analysis, the lift and drag distribution based on the Kutta-Joukowski theorem are used, since they are less sensitive to panel density. In subsection B, the results of both analysis methods are compared.

#### A. APPLICABILITY OF FLIGHTSTREAM FOR SLIPSTREAM CONTRACTION AND OUT-OF-PLANE SWIRL RECOVERY

The goals of the initial validation case were to find the best setup for Flightstream and CFD at a modest computational cost, and to investigate whether Flightstream could capture certain flow phenomena. The two most important are the effect of the propeller slipstream contraction on the wing lift and drag, and the

ability of the wing to recover swirl velocities that are not perpendicular to the wing plane. These are assumed to be captured by CFD, so if Flightstream agrees well with CFD, it should be able to simulate these phenomena as well. The good agreement of CFD and Flightstream for lift, drag and pressure distributions seem to suggest that this is the case. Whether these phenomena actually played any role is investigated here, based on the Flightstream simulations.

As already mentioned in [section 5.1](#), the slipstream contraction is negligibly small, as will be its effect on the angle of attack of the wing. It is thus not possible to conclude whether Flightstream captures the effect or not, but also not relevant to the discussion in this report. On the other hand, the lift does increase for the wing when mounted below the propeller, as can be seen in [Figure 5.3a](#). This may be caused by an increased circulation on the wing, due to the higher slipstream velocity on the upper side of it.

The results obtained with Kutta-Joukowski in [Figure 5.7](#) suggest that Flightstream is able to capture swirl velocity when it is not perpendicular to the wing. Swirl velocities would increase the angle of attack behind the upgoing blade and decrease it behind the downgoing blade. Since the freestream angle of attack of the initial validation case is zero, this leads to positive and negative lift behind the up- and downgoing blades, respectively. This is indeed visible in the plots. As already explained, the lift vector tilts forward in both cases, and leads to local negative induced drag. This behaviour is observed in [Figure 5.7b](#), which suggests that Flightstream indeed captures swirl velocities not perpendicular to the plane of the wing.

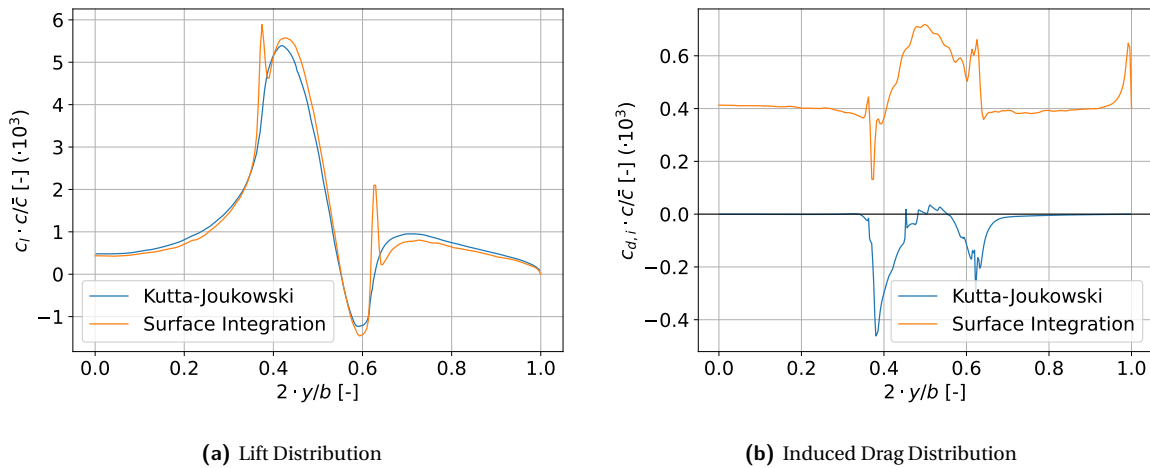


Figure 5.7: Comparison between surface integration and the Kutta-Joukowski theorem for obtaining aerodynamic force distributions.

## B. CALCULATING AERODYNAMIC FORCES USING SURFACE INTEGRATION AND KUTTA-JOUKOWSKI

For the validation, force distributions have been obtained using surface integration for both CFD and Flightstream. Using surface integration has some inherent drawbacks. The requirement for a prohibitively fine mesh has already been mentioned in [subsection 4.1.1](#). Another challenge is that it gives different results compared to using the Kutta-Joukowski theorem, combined with lifting line theory. When using the latter, the analysis of a wing including nacelle (as seen on the SBW configuration) implicitly adds the effect of the nacelle to the lift distribution. It only looks at the vorticity shed at the trailing edge of the wing, part of which comes from the nacelle. Surface integration would only include the indirect interference effects of the nacelle on the wing.

The difference between surface integration and the Kutta-Joukowski theorem is illustrated for the initial validation case in [Figure 5.7](#). Both methods analysed the same simulation in Flightstream. For the lift, the two methods agree rather well. Surface integration gives better result for calculations in lift than for induced drag. This is because the orientation of mesh cells is less important for calculating lift, hence it is less dependent on the mesh density. Induced drag gives larger differences between the two methods. Surface integration predicts a constant drag everywhere, with an increase behind the propeller slipstream ( $0.37 < 2 \cdot y/b < 0.63$ ). The Kutta-Joukowski results do not give any drag outside this region, and yields negative induced drag behind the propeller slipstream. The surface integration clearly overestimated the induced drag. The integrated value would be 88 counts. When assuming a span efficiency of 0.8, this is the induced drag the unpowered wing

would have at a lift coefficient of 0.67. The Kutta-Joukowski results seem more reasonable. Since the wing is at zero angle of attack, all lift results from a change in angle of attack caused by the propeller or nacelle. These would locally tilt the lift vector forward, even in the case of negative lift, and so lead to negative induced drag.

### 5.3. STRUT-BRACED WING

In the previous section, it was shown that Flightstream adequately predicts lift, drag and pressure distributions for the simplified initial validation configuration. This allowed selecting the right settings for Flightstream at a reasonable computational cost. It also suggested that phenomena relevant for a strut-braced wing, such as out-of-plane swirl velocities are captured well by Flightstream. Furthermore, it was found out that slipstream contraction does not play a significant role, even though that was expected initially. In this section, the JSBW configuration is validated, both with and without propeller. First, the integral values for lift and drag are used for validation in [subsection 5.3.1](#). Next, the lift and drag distributions for the wing, strut and jury strut are validated in [subsection 5.3.2](#), [subsection 5.3.3](#) and [subsection 5.3.4](#), respectively.

#### 5.3.1. INTEGRAL LIFT AND DRAG

The integral, time-averaged values for lift and drag are compared in [Table 5.3](#). The largest differences between Flightstream and CFD are for the lift. Especially the propeller-on case has a large difference, more than twice that of the propeller-off case. Drag is much more accurate, being well within 5% for the powered and unpowered aircraft. Both methods predict a decrease in total drag for the propeller-powered strut-braced wing, but Flightstream predicts a larger advantage. This may either be caused by the simplifications of a panel method, it could also be attributed to the different analysis method used for both. Flightstream used Kutta-Joukowski for the induced drag, combined with the profile drag calculated from the boundary layer equations applied to surface streamlines on the body. The CFD drag comes from the integration of pressure and friction drag over all the surfaces of the aircraft.

Table 5.3: Lift and drag averaged over 60 degrees of propeller rotation.

		CFD	Flightstream	Difference [%]
<b>Propeller-Off</b>	$C_L$ [-]	0.390	0.418	6.7%
	$C_D$ [cts]	162.1	165.9	2.2%
<b>Propeller-On</b>	$C_L$ [-]	0.391	0.453	15.9%
	$C_D$ [cts]	158.1	153.1	3.2%

#### 5.3.2. WING

The comparison between CFD and Flightstream for the wing lift and drag distributions is given in [Figure 5.8](#). In the propeller-off case, lift and pressure drag agree very well. Inboard of the strut-wing junction, Flightstream seems to overestimate the lift slightly. This may be caused by interference between the strut and wing, which would cause the flow speed inside the wing-strut channel to increase. Compressibility might increase the interference, which is not captured by potential flow. When looking at the  $C_p$  plot at  $2 \cdot y/b = 0.35$  in [Figure 5.9a](#), Flightstream slightly overestimates the pressure at the pressure side of the wing. Whether this is caused by compressible interference with the strut, or something else is unclear. In the same region, Flightstream also overestimates the pressure drag slightly, although the differences are small. Surprisingly, Flightstream predicts a higher friction drag away from the propeller region in the propeller-off case, compared to the propeller-on case.

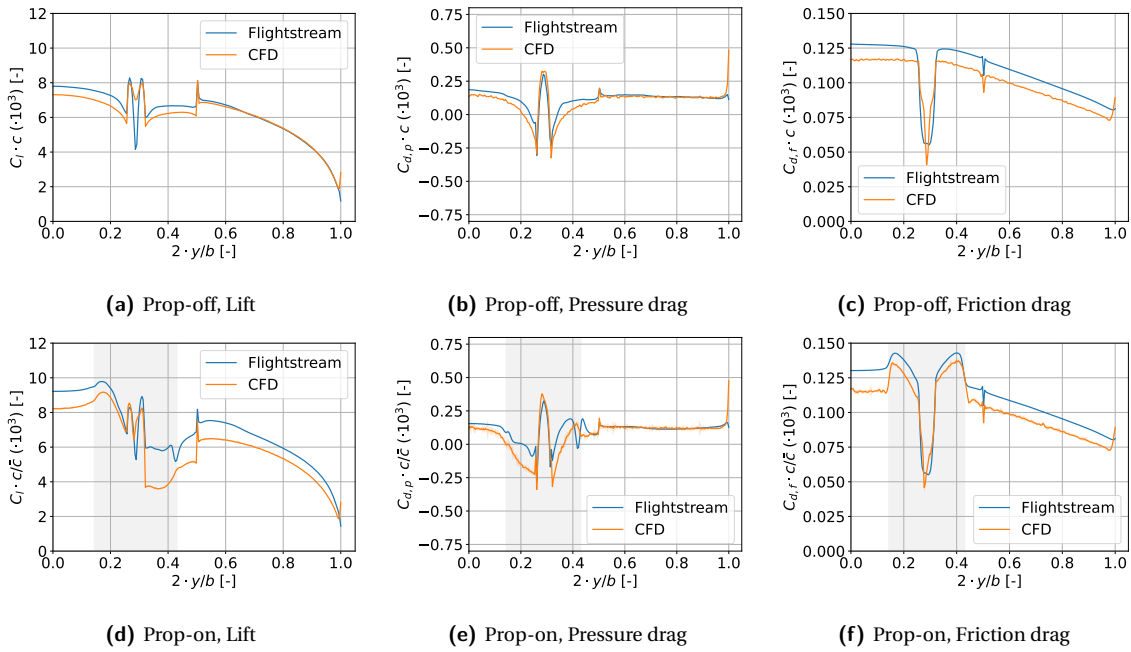


Figure 5.8: Lift and drag distribution of the wing of the JSBW configuration, with and without propeller. In the propeller-on case, the discretisation uncertainty bands for the CFD simulation have been added.

In the propeller-on case, Flightstream overestimates the lift everywhere. This is most apparent between the nacelle and strut junctions ( $0.29 < 2y/b < 0.5$ ). According to the  $C_p$  plot in Figure 5.9b, the discrepancy is mostly caused by an overestimated suction at the suction side of the wing. A similar offset was observed in the propeller slipstream of the initial validation case. In addition, Flightstream fails to capture the pressure peak near the leading edge of the airfoil. This may have been caused by an inadequate panel density. Similar to the initial validation, some peaks are present in the lift distribution at the edge of the propeller slipstream (marked in grey), these are caused by the propeller tip vortices, which do not lose their strength in Flightstream.

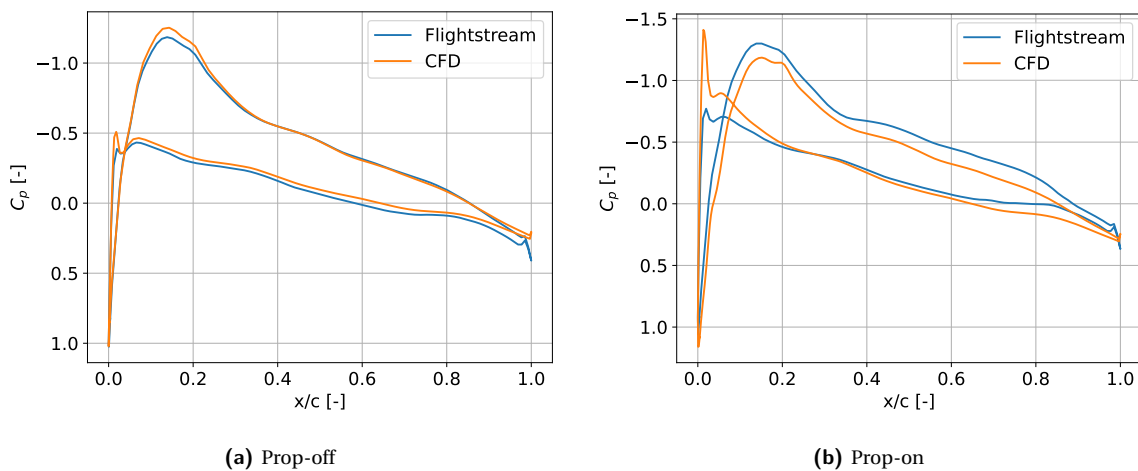


Figure 5.9:  $C_p$  plots at  $2 \cdot y/b = 0.35$  of the main wing.

The pressure drag is also overestimated by Flightstream. The CFD simulation predicted a region around the nacelle ( $2 \cdot y/b = 0.29$ ) where the pressure drag is negative. This region is also present in Flightstream, but is much smaller. Finally, the friction drag on the wing agrees well with that predicted by CFD. As was the case for the initial validation, Flightstream underestimates the friction drag in the propeller slipstream, but slightly

overestimates it outside of it. Still, the error is relatively small, and may have been caused by the chordwise panel density in Flightstream. There was still a large discretisation error in friction drag for the current mesh.

### 5.3.3. STRUT

The lift and drag of the strut are generally simulated well by Flightstream, see Figure 5.10. For the unpowered configuration, Flightstream and CFD are very close, especially for lift and pressure drag. When considering propeller effects, there are some peaks in the lift distribution predicted by Flightstream that are not found by CFD. At  $2 \cdot y/b = 0.43$ , there is a peak in the lift distribution of Flightstream. It is possible that this is caused by the interaction between the propeller tip vortex and the strut, which is not captured perfectly by Flightstream. This was already observed for the initial validation.

Near the edges of the slipstream, the pressure drag predicted by Flightstream diverges from CFD. At  $2 \cdot y/b = 0.25$ , there is an increase in pressure drag inboard, and a decrease outboard. The shape of this oscillation looks as if it has been caused by a vortex rotating in the direction of the freestream. This is consistent with the hypothesis that it is caused by a propeller tip vortex. At high advance ratios, the propeller vortex system becomes more aligned with the freestream. When it intersects a wing or a strut, it will induce velocities in its plane. This locally changes the angle of attack, and alters the lift and induced drag. It is likely that this is what causes the oscillations in lift and pressure drag. In the CFD simulation, the vortex loses strength due to diffusion and viscosity, which limits the effect of the vortex on the strut. Again, the skin friction drag agrees well with that of CFD.

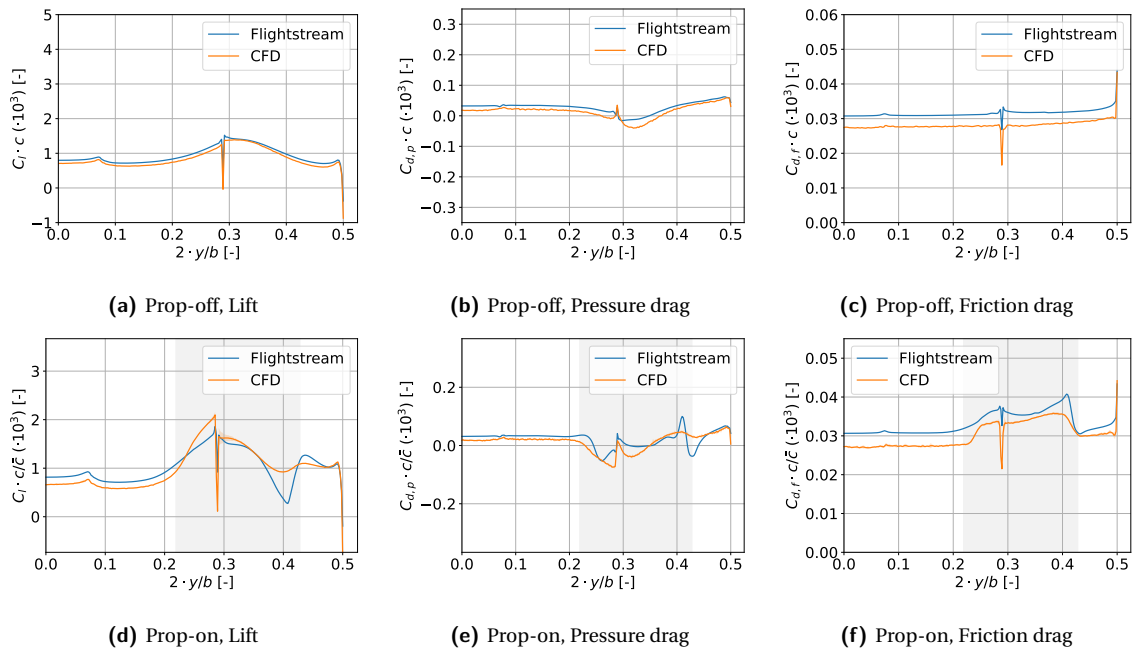


Figure 5.10: Lift and drag distribution of the strut of the JSBW configuration, with and without propeller.

### 5.3.4. JURY STRUT

Figure 5.11 shows the comparison between CFD and Flightstream for the jury strut. Instead of lift, the side force is used for validation in Figure 5.11a and Figure 5.11d. The force distributions are plotted from the bottom up, so a  $z$ -location of zero is the strut-jury strut junction, and 1 the nacelle-jury strut junction.

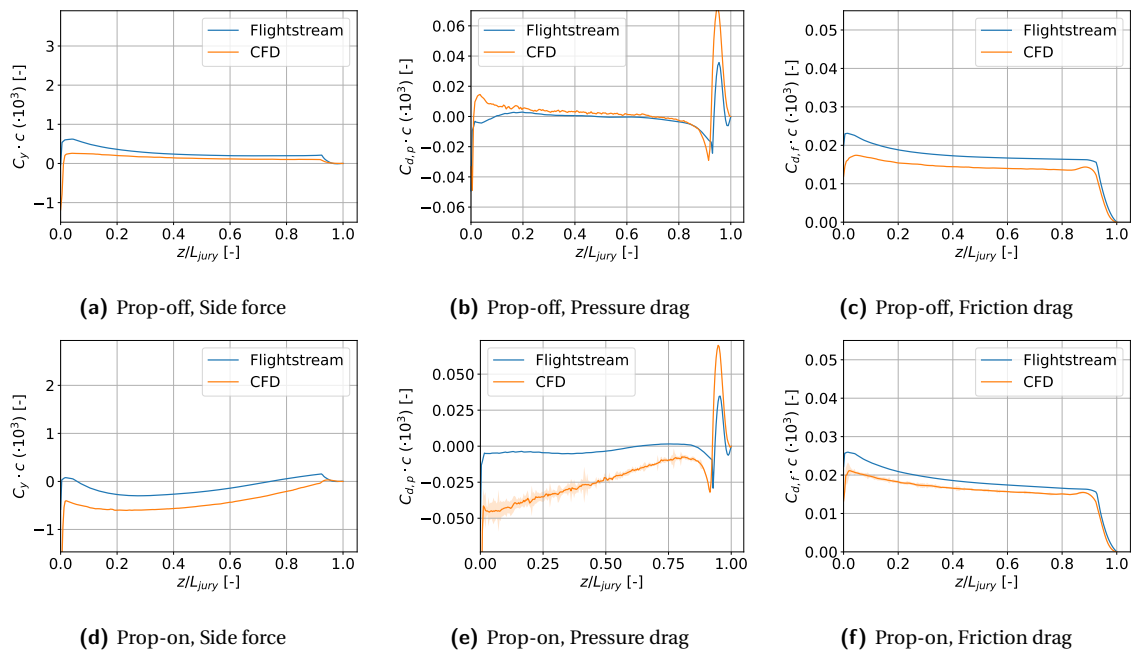


Figure 5.11: Lift and drag distribution of the jury strut of the JSBW configuration, with and without propeller.

As was the case for the wing and main strut, Flightstream is very accurate in the propeller-off case. It overestimates the side force by a factor of almost 2, but the magnitude of the force is small, giving a small absolute error. The propeller-on case is more different, Flightstream underestimates the magnitude of the side force, although the shape of the plot is similar. Surprisingly, the side-force becomes positive (outboard) near the strut-jury strut junction. Given that the propeller rotates inboard up, one would expect the jury strut to be loaded inboard, due to the propeller swirl. This is also what was predicted by the CFD simulation.

As a consequence of the near-zero loading of the jury predicted by Flightstream, the pressure drag is also very low (remembering that no viscous iterations were performed, hence pressure drag equals induced drag). CFD predicted a negative pressure drag over almost the entire jury strut. This is also the case for the Flightstream simulation, but the magnitude is very small. One of the hypothesis put forward at the beginning of this report is that the jury strut would act as a swirl recovery vane. The large difference in side-force and pressure drag makes this difficult to confirm using Flightstream alone, although it makes a conservative estimate.

Finally, the friction drag is predicted very well by Flightstream. Given the similar agreements for the strut and the wing, it is concluded that Flightstream gives a reliable estimate for this. This is somewhat surprising, given that the chordwise distribution of the skin friction drag was not particularly accurate, see [Figure 5.5b](#).



# 6

## RESULTS

In this chapter, the research questions are answered. It is started with a treatment of the induced drag in [section 6.1](#). First the effect of the propeller on the overall drag of the aircraft is considered. It is followed by a breakdown of the contributions the different wing components have to the change in induced drag caused by the propeller. In this configuration induced drag represents about a quarter of the total drag. Hence it is important to consider viscous drag as well, which is done in [section 6.2](#). Regions of flow separation are identified, and the effect of the propeller on their size is treated. Next, the effect of aero-propulsive interactions on friction drag are considered. Not treated in this report are the effects of viscosity on the pressure drag, as the methods used do not allow calculating it. To obtain this component of the drag, wake analysis is required, which is outside the scope of this report. Finally, a short treatment of compressibility and interference effects is given in [section 6.3](#).

### 6.1. INDUCED DRAG

This section focuses on induced drag, and the effect the propeller has on it. The results presented in this section are obtained using a panel method, where the lift and drag are calculated using Kutta-Joukowski. First, the overall effect of the propeller is investigated in [subsection 6.1.1](#). In this section, the lift and induced drag with and without propeller are compared for the different configurations (conventional wing (CW) and strut-braced wing, with (JSBW) and without jury strut (SBW)). Next, the effect of the different wing components on the propeller-induced change in induced drag are quantified. This is started with the main strut, which is done by comparing the conventional wing with the strut-braced wing without jury in [subsection 6.1.2](#). Next, the effect of the jury strut is treated in [subsection 6.1.3](#) by comparing the SBW and JSBW configurations.

#### 6.1.1. OVERALL EFFECT OF THE PROPELLER

The overall effect of the propeller on the lift and induced drag of the different configurations was evaluated. This is summarised in [Table 6.1](#). The total lift of the three configurations is similar for propeller-on and -off conditions, with the strut-braced wings having a slightly larger lift. This is likely due to the additional lifting surfaces. While the jury strut increases the lift of the strut, it also decreases the lift of the main wing, see [Figure 6.1](#). These roughly cancel each other out. In the propeller-off case, the conventional wing has the lowest induced drag. This is surprising, given that Takahashi and Donogan [50] found that a strut-braced wing could achieve higher span efficiencies than conventional wings. Note however that none of the configurations used in this paper are optimised. By optimising the loading distribution, it should be possible to achieve a lower induced drag for all the configurations. This might make the difference between the strut-braced wings and conventional wing either larger or smaller. While it is outside the scope of this report, it would be interesting to study at a later stage.

Table 6.1: Effect of the propeller on the total lift and induced drag of the different configurations. The final three rows give the induced drag when the lift coefficient is corrected to 0.4.

		<b>Prop-off</b>	<b>Prop-on</b>	<b>Difference [%]</b>
$C_L$ [-]	<b>CW</b>	0.402	0.438	9.0%
	<b>SBW</b>	0.420	0.453	7.9%
	<b>JSBW</b>	0.418	0.453	8.3%
$C_{D,i}$ [cts]	<b>CW</b>	40.5	20.5	-49%
	<b>SBW</b>	43.6	21.3	-51%
	<b>JSBW</b>	42.9	21.3	-50%
$C_{D,i_{C_L=0.4}}$ [cts]	<b>CW</b>	40.1	17.0	-58%
	<b>SBW</b>	39.5	16.4	-59%
	<b>JSBW</b>	39.2	16.4	-58%

When considering propeller effects, the case is altered. In all cases, the propeller increased the lift by roughly 8%, and reduced the induced drag significantly. For the conventional wing, the induced drag reduced by 49%, while the strut-braced wings experienced an additional 2% and 1% reduction (without and with jury strut respectively), which is not enough to have a lower induced drag than the conventional wing. Contrary to what was expected in the theory section in the beginning of the report, the jury strut does not lead to an additional decrease in induced drag, reducing the gain by one percent. This is investigated in more detail later on.

To make the comparison more fair, the induced drag should be compared at a constant lift coefficient. If the drag polar is given by Equation 6.1, the change in induced drag for a given change in lift coefficient can be easily calculated by linearising around the lift coefficient resulting from the simulation. This is a simplification, most drag polars do not have minimum drag at zero lift. However, assuming that the lift coefficient corresponding to minimum drag is small, it can still be used. Note also that the propeller-on cases are assumed to have a parabolic drag polar to correct the induced drag, results obtained by Sinnige et al. [41] suggest that this is reasonable. The induced drag for all configurations, corrected to a lift coefficient of 0.4 are given in the bottom part of Table 6.1. Now the two strut-braced wings perform better than the conventional wing both with and without propeller, which is more in line with Takahashi and Donogan [50]. The difference between prop-off and -on increases by almost 10% at constant lift. In unpowered condition, the JSBW configuration performs slightly better than the SBW. With propeller, this advantage disappears.

$$C_D = C_{D,0} + \frac{C_L^2}{\pi A e} \quad (6.1)$$

The lift distributions of the different configurations, with and without propeller are shown in Figure 6.1. The two strut-braced wing configurations have very similar wing lift distributions. While it is almost invisible in the plots, the SBW configuration has a slightly higher wing lift than the JSBW configuration. The jury strut (located at  $2 \cdot y/b = 0.29$ ) causes a small increase in strut lift inboard of the strut-jury strut junction. Since the jury strut is separated from the wing by the nacelle, its influence on it is limited. When comparing with the conventional wing, it can be seen that the strut reduces the lift of the main wing. This may be caused by the velocity the strut induces on the main wing, illustrated in Figure 6.2. Because the strut induces a downwash at  $x = 0.75c$  of the main wing, the circulation of the main wing reduces. This could also explain why the difference between the lift of the (J)SBW and CW configuration gets smaller near the wing root. The strut and wing are spaced farther apart, reducing the influence of the strut.

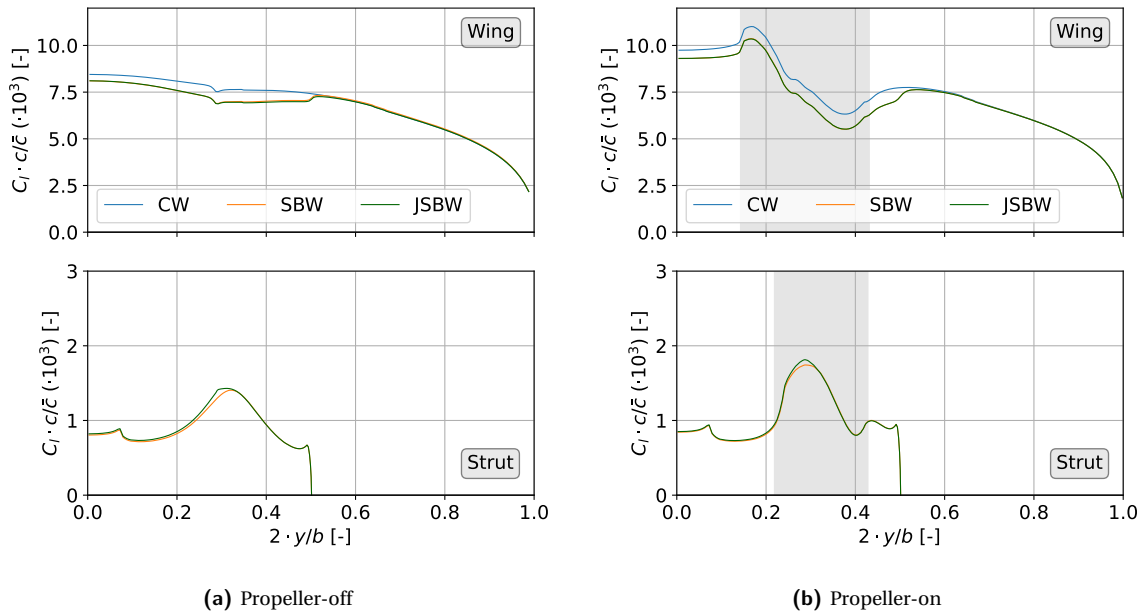


Figure 6.1: Effect of the propeller on the lift distribution of the different configurations. For the two strut-braced wings, the lift distribution on the strut is shown as well. In the propeller-on plot, the portion of the wing submerged in the propeller slipstream is highlighted.

In the propeller-on case, the effect of the propeller on the main wing is clearly visible. The lift increases behind the upgoing blade, and decreases behind the downgoing blade. The effect on the strut is smaller. The lift also increases and decreases behind the up- and downgoing blades, respectively. The propeller also increases the lift just outboard of the slipstream. This cannot be caused by slipstream contraction, which was already proven to be negligible. It is possible that a similar effect as shown in Figure 6.2 is responsible, but with the effect the wing has on the strut. Because of the swirl velocity, the lift on the wing and strut reduces behind the downgoing blade. The portion of the strut just outboard of the slipstream is still under the influence of the vorticity of the main wing portion inside of it. Because the circulation of that part of the wing reduces, its downwash on the strut also reduces. In turn, the bound vorticity of the strut needs to increase to maintain flow tangency, increasing the lift there.

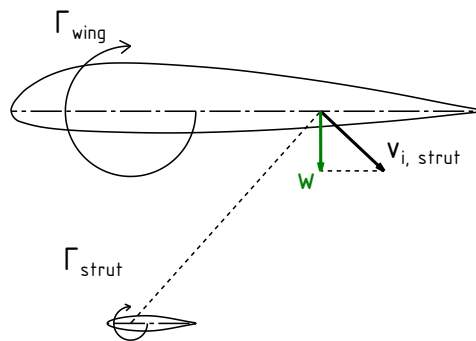


Figure 6.2: Effect of the vorticity of the strut on the wing circulation.

The effect of the propeller on the induced drag distributions is shown in Figure 6.3. Because the induced drag distributions obtained by Kutta-Joukowski gave relatively noisy graphs, they have been filtered using a 4<sup>th</sup> order Butterworth filter, with a cut-off frequency of 30.

Without propeller effects, the induced drag of the wing is fairly constant, except at two locations. At the strut-wing junction ( $2 \cdot y/b = 0.5$ ), the SBW and JSBW configurations exhibit an oscillation in induced drag. Inboard of the junction, it increases, while decreasing outboard of it. This cannot be caused by the change in wing lift at that location (see Figure 6.1a). An increase in wing lift in spanwise direction would shed a

vortex that rotates in the negative  $x$ -direction (inboard up), causing a downwash outboard of the nacelle, and an upwash inboard of it. This is sketched in [Figure 6.4a](#). As a result, the induced drag would decrease inboard, and increase outboard, the exact opposite of what is observed. Instead, the cause is more likely the tip vortex shed by the strut, which rotates in the opposite direction, see [Figure 6.4b](#). The net effect of it is a reduction in wing induced drag for the strut-braced wings. A similar effect is seen at the nacelle-wing junction ( $2 \cdot y/b = 0.29$ ), although the behaviour is much less clear there. It is likely caused by the trailing vorticity of the nacelle, which was added to model flow separation on the base region. As already noted for the lift distributions, the jury strut has no noticeable effect on the wing drag.

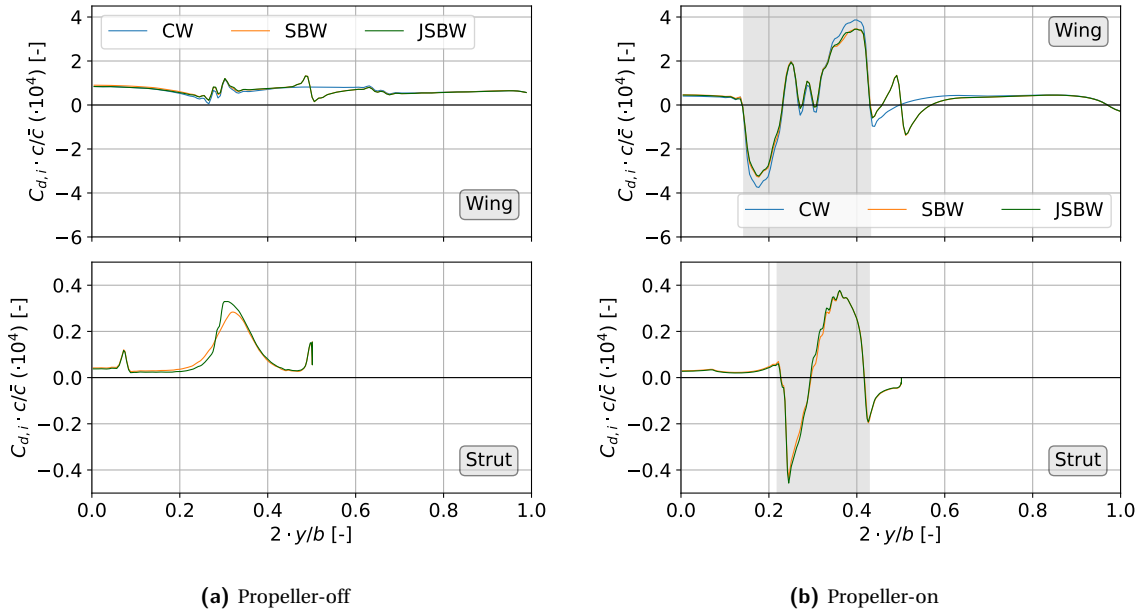


Figure 6.3: Effect of the propeller on the induced drag distribution of the different configurations. The locations where the wing elements are submerged in the slipstream have been highlighted.

The induced drag of the strut without propeller is similar for the JSBW and SBW, except near the strut-jury strut junction ( $\eta = 0.29$ ). There, the jury strut causes an increase in induced drag outboard, and a decrease inboard of the junction.

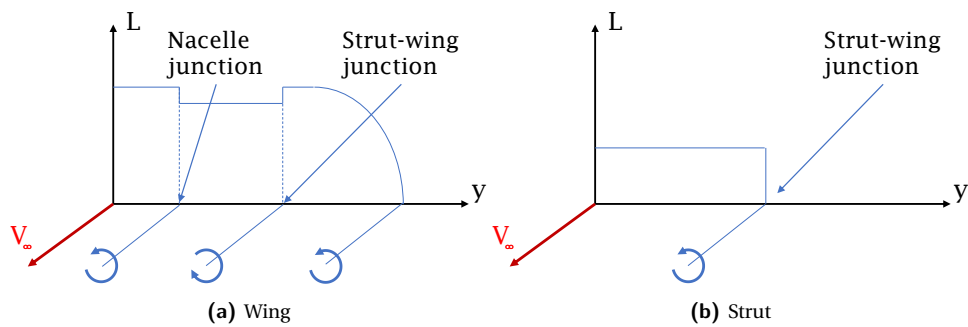


Figure 6.4: Schematic of the lift distribution and shed vorticity of the main wing and strut in propeller-off conditions.

With propeller, the induced drag of the wing changes significantly, see [Figure 6.3b](#). Some trends can be made out. First, the induced drag reduces inboard of the nacelle, and increases outboard. The propeller swirl velocity induces an increase in angle of attack behind the upgoing blade, and decrease behind the downgoing blade. As explained by Veldhuis [56], this tilts the lift vector forward behind the upgoing blade, and aft behind the downgoing blade. The effect is known as swirl recovery. A schematic drawing of it is shown in [Figure 6.5](#), where the swirl velocity is denoted as  $V_\tau$ . For the main wing, the differences between the two strut-braced

wings are minimal, although they behave slightly different than the conventional wing. The conventional wing is influenced more by the propeller, having a larger increase and decrease induced drag behind the down- and upgoing blades. This may again be because the strut reduces the circulation of the main wing, thus damping the propeller-induced effects. In the slipstream (the shaded region in the plot), the conventional wing has an induced drag 1 count lower than the two strut-braced wing configurations. This advantage is offset outboard of the propeller slipstream, where the induced drag of the SBW and JSBW is 1.5 counts lower than for the CW. This is caused by the strut-wing junction, where the tip vortex shed by the strut induces an oscillation in the wing induced drag. Because of the larger lift of the strut near the junction, this vortex is stronger in the propeller-on case.

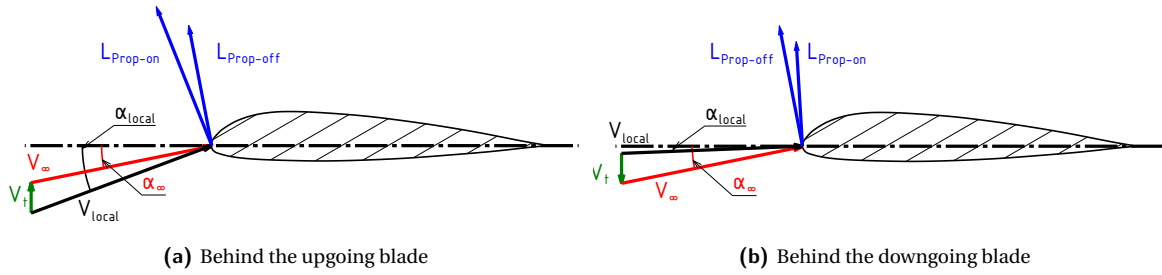


Figure 6.5: Drawing of the swirl recovery mechanism.

Inside the slipstream, the induced drag of the strut is qualitatively similar to that of the main wing, with a reduced and increased induced drag behind the up- and downgoing blades, respectively. Just outboard of the slipstream, the strut has negative induced drag. This may be caused by the decrease in lift on the main wing inside the slipstream, which reduces the downwash on the strut portion outside the slipstream. It is interesting to note that the jury strut has very little effect on the induced drag of the strut, even though they are spaced very closely together.

### 6.1.2. EFFECT OF THE STRUT

The first research question is concerned with the effect the main strut has on the change in induced drag due to the propeller. To answer this research question, the induced drag values will not be corrected to a constant lift coefficient. While the correction may be reasonably accurate for complete wings, it is not certain whether it applies to the drag breakdown for the individual wing elements as well. The contribution of propeller-strut interaction to the induced drag of a strut-braced wing is found by first calculating the contribution of the propeller to the induced drag. This is done by subtracting the induced drag of the configuration with propeller from that without propeller. To isolate the effect of propeller-strut interactions, the propeller effect on induced drag from the strut-braced wing is subtracted from that of the conventional wing. The above procedure is summarised in [Equation 6.2](#).

$$\Delta C_{D,i} = (C_{D,i_{SBWP}} - C_{D,i_{SBW}}) - (C_{D,i_{CWP}} - C_{D,i_{CW}}) \quad (6.2)$$

Applying the equation above, it is found that the strut increases the reduction in induced drag due to the propeller by 2.3 counts. The total reduction in induced drag due to the propeller of the SBW configuration is 22.3 counts, meaning the strut is responsible for 10% of the change. This is rather large, given that the strut only contributes to 6.8% and 4.6% of the total induced drag, for the propeller off and on cases, respectively. This can be derived from [Table 6.2](#). Additionally, the reduction in induced drag of the strut itself due to the propeller is 2 counts. The additional 0.3 counts come from interactions with the main wing. While the strut reduces the swirl recovery for the wing portion inside the propeller slipstream, it sheds a vortex at the strut-wing junction that leads to a net reduction in wing induced drag. These effects were described in more detail in the preceding section.

Table 6.2: Induced drag in counts of different components for the conventional and (jury) strut-braced wing configurations.

		Prop-off	Prop-on	Diff. [%]
CW	wing	40.5	20.5	-49
	strut			
SBW	wing	40.7	20.4	-50
	strut	3.0	1.0	-67
JSBW	wing	39.9	20.5	-49
	strut	3.0	1.0	-67
	jury	0	-0.2	$-\infty$

### 6.1.3. EFFECT OF THE JURY STRUT

The effect of the jury strut on the change in induced drag due to the propeller is smaller than that for the strut. Similar to the previous section it is calculated using Equation 6.3. It is found that the jury strut counteracts the drag reduction due to the propeller by 0.8 counts. Based on the literature review, it was thought that the jury strut would be an effective swirl recovery device. To some extent, this is true. The jury strut itself experiences a thrust component instead of drag, likely caused by swirl recovery. This can be seen in Figure 6.6b, where the strut experiences an induced thrust component over most of its span in the propeller-on case. The propeller-off configuration also has this, but much smaller in magnitude. It is offset by a relatively large peak in induced drag near the strut-jury strut junction. The reduction in induced drag in the powered case is caused by the swirl velocity of the propeller, which increased the angle of sideslip of the jury strut. This caused an inboard force, and tilted the sideforce vector forward. The loading of the jury strut is shown in Figure 6.6a. Note how the direction of the sideforce changed from outboard to inboard when turning on the propeller.

The drag reduction of the jury strut due to swirl recovery is not significant, at 0.2 counts. This means that the negative net effect of the strut on the propeller-induced drag change is caused by its interference with the other wing elements. Indeed, the reduction in induced drag by the propeller is counteracted by 1 count for the wing when adding the jury strut. It does not have any effect on the drag reduction by the main strut.

$$\Delta C_{D,i} = (C_{D,i_{JSBWP}} - C_{D,i_{JSBW}}) - (C_{D,i_{SBWP}} - C_{D,i_{SBW}}) \quad (6.3)$$

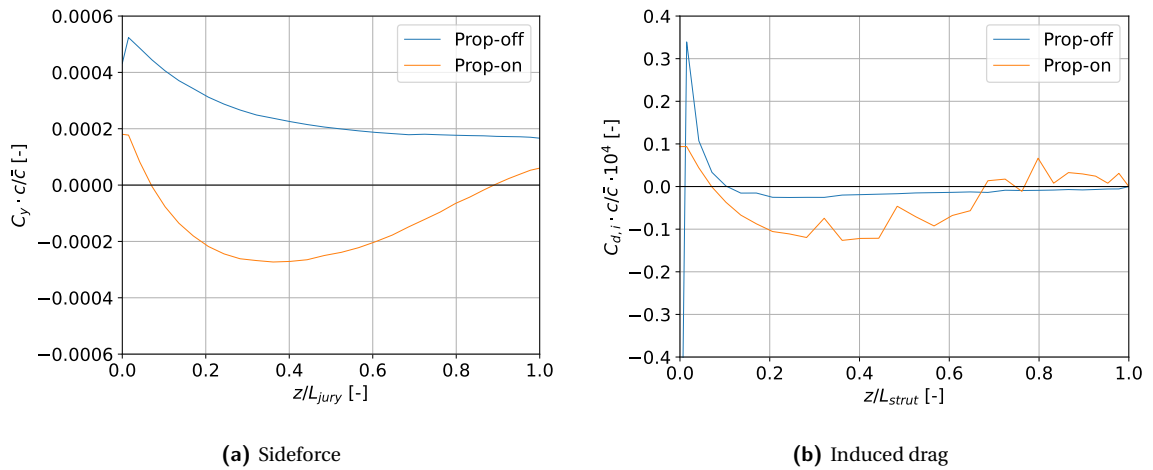


Figure 6.6: Loading distributions on the jury strut

It might be possible to increase the swirl recovery by the jury strut by optimising its loading distribution. An upper bound for the reduction in induced is obtained using the average swirl angle in the slipstream. Using the Flightstream results, this was found to be 2.3 degrees. This is the angle with which the sideforce vector is tilted forward. Maximising the sideforce would also maximise the component of it in the freestream direction, giving induced thrust. Using XFOIL at a Reynolds number of  $1 \cdot 10^6$  (representative for the jury strut in cruise) and an N factor of 9, a maximum lift coefficient of 0.94 was found for the strut airfoil. The component of this lift vector acting in freestream direction under the influence of the swirl velocity would be equivalent to 378

drag counts, with respect to the surface area of the jury strut. Converting this to the reference area of the wing gives a maximum induced thrust of 1.1 counts for the jury strut. The jury strut of the current configuration already had a thrust component of 0.2 counts. The net effect of increasing the jury strut loading would be to further reduce the induced drag of the JSBWP configuration from 21.3 to 20.4 counts. Note that this method does not take into account the increased normal-wash due to the side force on, which would locally reduce the angle of sideslip on the strut. Furthermore, negative influence of it on the wing and strut are ignored, these would further offset the gain in induced drag from the jury. To conclude, the jury strut has a very modest influence on the induced drag reduction by the propeller, even when its loading distribution would be optimised.

## 6.2. VISCOUS EFFECTS

This section deals with viscous effects. For this, the CFD simulation of the JSBWP configuration on the finest mesh (M5) is used, both with and without propeller. First, separation is dealt with in a qualitative way in [subsection 6.2.1](#). Flow separation was only observed at junction regions, the two most important of which are presented. Next, the effect of the propeller on friction drag is treated in [subsection 6.2.2](#). First, the increase in friction drag is obtained from the CFD simulations. It is then attempted whether actuator disk theory is able to predict this value.

### 6.2.1. SEPARATION

Separation was observed in multiple regions of the wing, but only in the context of junction flows. The criterion to detect separation was a negative local skin friction coefficient, indicating flow reversal. Junction regions susceptible to separation include the propeller-spinner connection, the nacelle base region, the nacelle-wing junction, the strut-jury strut junction and the strut-wing junction. As only the latter two are relevant for a strut-braced wing, only these will be treated in this section. A consequence of the Spalart-Allmaras turbulence model is that the boundary layer is turbulent everywhere. This may have resulted in an optimistic estimate of the separated regions, as a turbulent boundary layer is more resistant to separation than a laminar one.

**Strut-Wing Junction** Even though it was identified as a sensitive region by Secco and Martins [39], only minor separation was observed at the wing-strut junction (its location is highlighted in [Figure 6.8](#)). This is possibly because of the relatively low Mach number of the strut-braced wing in this paper, along with the absence of shock waves in the junction region. The only separation identified was at the leading edge of the strut-wing junction, marked in red in [Figure 6.7](#). Separation in this figure is detected based on the wall shear stress; namely where the component in freestream direction is negative. This is likely a consequence of the junction flow as explained by Stanbrook [44]. The boundary layer ahead of the junction separates, which causes a horseshoe vortex wrapped around the root of the strut. The low pressure of the vortex causes it to attach to the surface of the wing or strut, which explains why separation is only observed at the leading edge of the strut. The horseshoe vortices are visualised in [Figure 6.9](#), for the wing with and without propeller. The structure and location of the horse-shoe vortex system is almost unchanged between the two cases. This is remarkable, especially since the pressure field on the inboard part of the junction did change under the influence of the propeller.

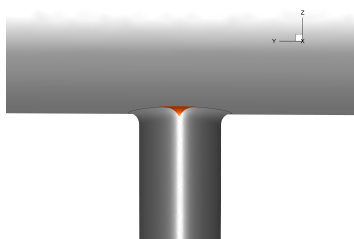


Figure 6.7: Separation at the leading edge of the strut. Areas where the component of the shear stress in freestream direction are negative are marked in red.

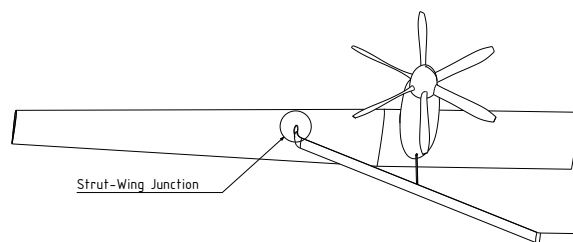


Figure 6.8: Location of the strut-wing junction

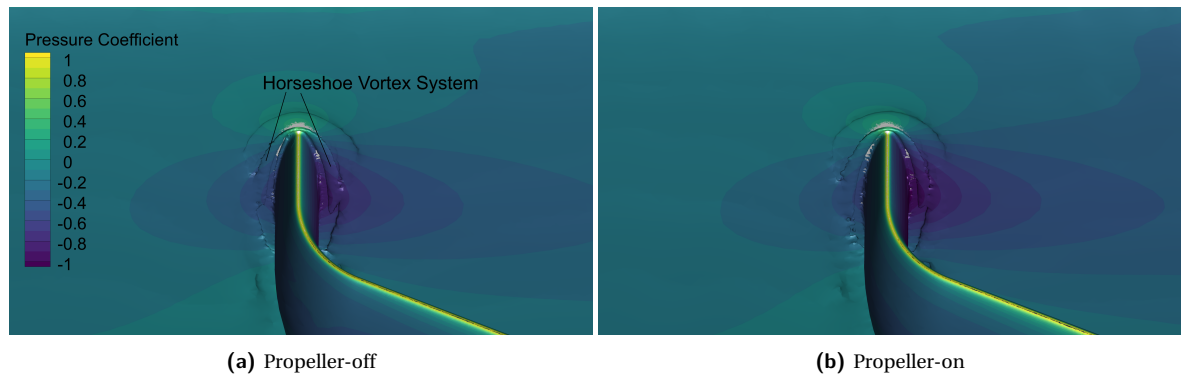


Figure 6.9: Horseshoe vortex system wrapped around the strut-wing junction. The vortices are visualised using iso-surfaces for the Q-criterion, equal to  $1000s^{-2}$ . The location of these figures is indicated in [Figure 6.8](#).

**Strut-Jury Strut Junction** More significant separation is observed at the strut-jury strut junction ([Figure 6.11](#)). In addition to separation at the leading edge of the jury, corner separation is observed at the trailing edge of the jury strut. It only occurs at the outboard part of the jury, due to its sharper angle with the main strut. According to Barber [5], corner separation depends largely on the incoming boundary layer thickness, where a thinner boundary layer will lead to a larger separated region. In the case of the strut-jury strut junction, the boundary layer is much thinner than at the wing-strut junction, where corner separation was not observed. In addition, the jury strut has a smaller chord length, which leads to larger pressure gradients that can cause the boundary layer to separate. The corner separation is present for both the propeller-on and -off case, but the separated region is smaller with the propeller on, as can be seen in [Figure 6.10](#).

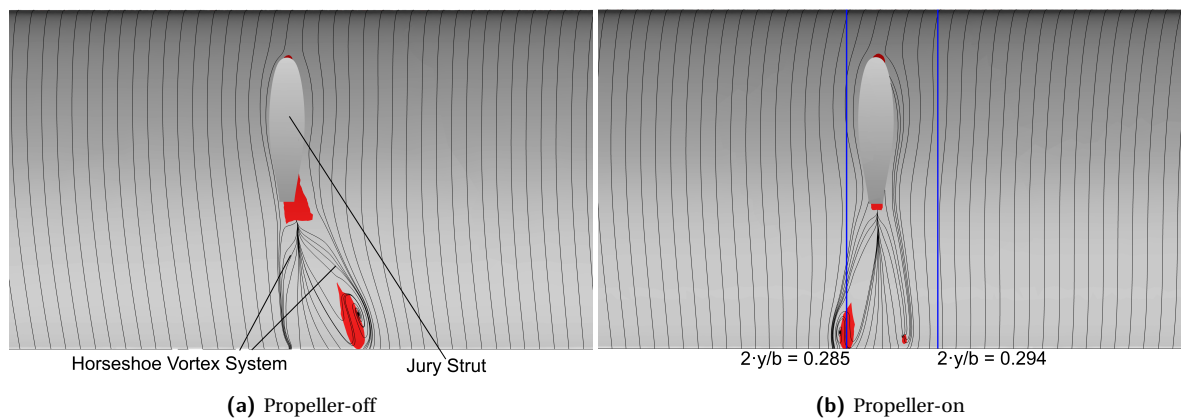


Figure 6.10: Surface shear lines around the strut-jury strut junction. Areas with separation (negative skin friction) are marked in red. The location shown in these figures is highlighted in [Figure 6.11](#).

The smaller region of corner separation in the propeller-on case can be caused by the swirl velocity of the propeller. [Figure 6.10](#) shows the shear lines on the strut around the jury strut junction. In the propeller-off case, the boundary layer travels outboard on the strut. There are two possible reasons for this. First, the large dihedral angle of the strut causes part of the incoming flow to be in the plane of the wing. This component can be calculated according to  $V_T = V_\infty \sin \alpha \sin \Gamma_s$ . Given that the dihedral angle of the strut  $\Gamma_s$  is 24.2 degrees, the tangential component of the freestream is 1.9 m/s, leading to an effective sweep angle of 0.82 degrees. This very moderate angle may not explain the outward travelling of the boundary layer sufficiently. Another explanation could be the lower pressure near the wing-strut junction, which could pull the boundary layer towards it. As a result of the outward movement of the boundary layer, the jury strut is at an angle of attack. This induces a larger adverse pressure gradient on the suction (outboard) side of the jury strut, which causes the already sensitive boundary layer to separate. The swirl velocity induced by the propeller counteracts the outboard flow, and reduces the angle of attack of the jury strut. As a consequence, the separated region at the trailing edge is much smaller, see [Figure 6.10b](#). Also visible in [Figure 6.10](#) is the horseshoe vortex system

resulting from the junction flow. Behind the trailing edge of the jury strut, the shear lines move outwards due to the velocity induced by the primary vortex system. Refer to Figure 2.2 for a schematic drawing of this vortex system.

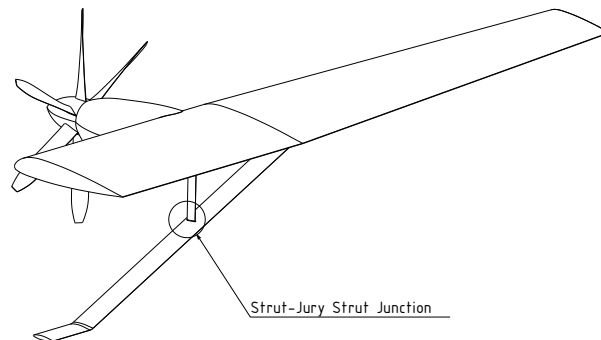


Figure 6.11: Location of the strut-jury strut junction

A second region of flow reversal is present near the trailing edge of the strut. In the propeller-off case, it is located at the outboard side of the jury strut, whereas it is located inboard in the propeller-on case. Initially, it was thought that separation is caused by an adverse pressure gradient on the strut. This was investigated by looking at  $C_p$  plots at both sides of the strut, the locations of which are shown in blue on Figure 6.10b. An adverse pressure gradient may indeed explain the presence of the separated region on the inboard (left) side of the strut in the propeller-on case. In Figure 6.12a, a larger pressure gradient can be seen between  $0.35x/c$  and  $0.6x/c$ . It may have been caused by the increased angle of attack of the strut, and the increased interference with the jury strut, due to the propeller swirl velocity. The larger pressure gradient may well have caused the boundary layer to separate.

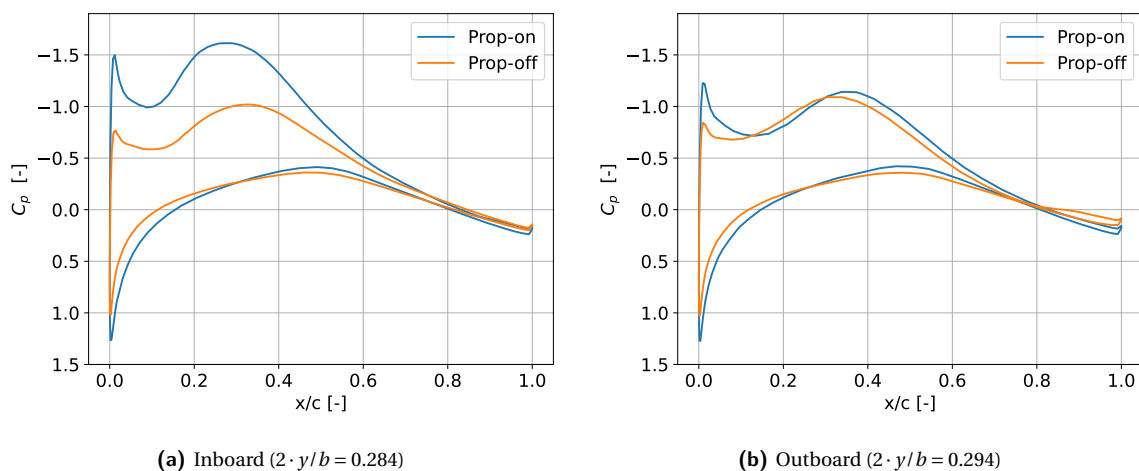


Figure 6.12: Pressure coefficients inboard and outboard of the strut-jury strut junction.

On the other hand, there are no significant differences in pressure gradient between propeller-on and -off cases on the outboard region, see Figure 6.12b. In fact, the propeller-on case exhibits the highest adverse pressure gradient, near the leading edge. A possible explanation could be that the boundary layer is thinner in the propeller-on case, due to the increased slipstream velocity. Using actuator disk theory, this would increase the Reynolds number by 0.6%, which would reduce the boundary layer thickness by 0.12% according to Prandtl's fifth power law ( $\delta/x = 0.37/Re_x^{1/5}$ ). This is negligible, as can be seen in Figure 6.13. It shows the

shape factor, boundary layer thickness and boundary layer profiles on the upper side of the strut. They have been taken at the same location as the  $C_p$  plots of Figure 6.12b. The boundary layer thickness according to Prandtl's fifth power law has been plotted too, it is very accurate until halfway the strut. Until around 70% of the strut chord, the boundary layers in the propeller-on and -off case have very similar velocity profiles and shape factors. This means that they are hardly altered by the increased slipstream velocity of the propeller. Behind 70% of the chord, the shape factor of the propeller-off case starts to increase. According to Castillo et al. [7], a turbulent boundary layer separates around a shape factor of 2.73, which is reached at  $x/c = 0.8$  for the propeller-off case. No separation is present for the prop-on boundary layer. Since there is no significant difference in boundary layer profile before reaching this and the pressure gradient is very similar, there must be another reason for the separation in the unpowered configuration. It is likely that it is caused by the horseshoe vortex system, which is only present at this location in the propeller-off case. Further research into corner flows and vortex breakdown mechanisms may provide more clues about this.

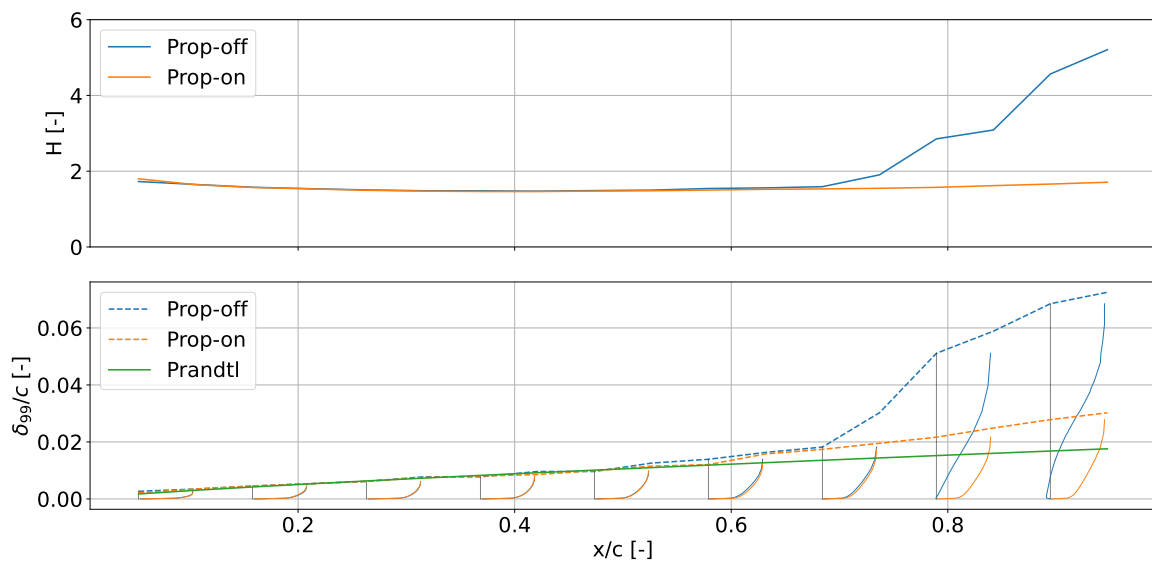


Figure 6.13: Shape factor, boundary layer thickness and velocity profiles near the strut-jury strut junction. Boundary layer profiles where taken along the outboard section shown in blue in Figure 6.10b.

Finally, the results of this section are put in perspective by noting that the location and size of the separated regions near the strut-jury strut junctions varied between the different meshes. Qualitatively, the behaviour of the finest mesh (used for this section) was similar to the second finest mesh, which suggests that the conclusions drawn here are still to some extent valid. Studying this sensitive region with either a finer mesh or a higher fidelity method such as a Large Eddy Simulation (LES) should yield more definite conclusions.

### 6.2.2. PROPELLER EFFECT ON FRICTION

The effect of the propeller on the friction drag is shown in Figure 6.14. As expected, the skin friction increases under the influence of the propeller slipstream. Furthermore, it is proportional to the slipstream velocity, this is evident from the wing skin friction coefficient. The increase in wing friction is higher behind the downgoing blade than behind the upgoing blade. This may be caused by interference between the different elements in the strut-wing-jury strut channel. The Mach number and velocity inside the channel is higher than outside of it, see Figure 6.15. This could have led to a higher skin friction drag in that region.

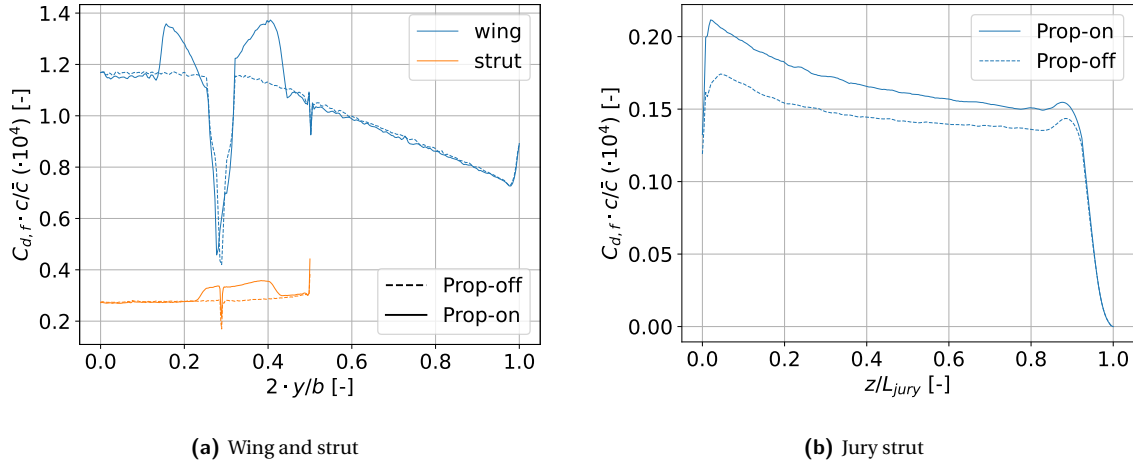


Figure 6.14: Effect of the propeller on the friction drag distribution.

The actual values for the friction drag of the different wing parts are given in Table 6.3. The effect of the propeller is limited. In total, the propeller causes an increase in friction drag smaller than 3%. Recall that the propeller reduced the induced drag by 37.92%, which is much more significant, even though the total induced drag is less than a third of the friction drag. It is also noted that the table only gives the friction drag. Viscous effects also cause a pressure drag component, due to flow separation and decambering. It was concluded earlier that the propeller reduced the size of separated regions, and likely reduces the pressure drag. The effect of the propeller on decambering is harder to assess. The boundary layer profiles plotted in Figure 6.13 suggest that the effect is limited. Assuming that the trailing edge separation is caused by vortex interactions, the boundary layer growth seems largely unaffected by the propeller. Finally, it is added that the results presented here may give an optimistic view of the propeller effects. The Spalart-Allmaras model causes the entire boundary layer to be turbulent, and hence ignored transition. According to Miley et al. [31], the propeller can move the transition point forward and increase the friction drag of the wing. On the other hand, at a Reynolds number of 5 Million, the size of the laminar region will be small.

Table 6.3: Friction drag of the different components of the strut-braced wing, with and without propeller

	Prop-off [cts]	Prop-on [cts]	Diff. [%]
<b>Wing</b>	118.2	120.6	2.0
<b>Strut</b>	16.6	18.0	8.4
<b>Jury Strut</b>	0.02	0.04	100
<b>Nacelle</b>	9.2	9.4	2.2
<b>Total</b>	144.0	148.0	2.8

The increase in friction drag looks proportional to the slipstream velocity behind the propeller. To verify whether this is the case, a simplified model is used to predict the increase in friction drag due to the propeller. It assumes a constant skin friction coefficient, and calculates the propeller slipstream velocity using actuator disk theory. If the increase in skin friction is proportional to the slipstream velocity, this should be able to predict the friction drag increase with some accuracy. In a wing with a propeller, the inflow velocity is no longer constant, so the definition of  $c_f$  is written as in Equation 6.4, where  $V_{in}$  is the local inflow velocity. The wing friction drag coefficient can be calculated according to Equation 6.5.

$$c_f = \frac{\tau}{\frac{1}{2}\rho_\infty V_{in}^2} \quad (6.4)$$

$$C_{D,f} = \frac{1}{\frac{1}{2}\rho_\infty V_\infty^2 S} \iint^{S_w} c_f \frac{1}{2}\rho_\infty V_{in}^2 dS = \frac{1}{S} \iint^{S_w} c_f \frac{V_{in}^2}{V_\infty^2} dS \quad (6.5)$$

The inflow velocity is assumed to be equal to  $V_\infty$  everywhere, except in the propeller slipstream. Using actuator disk theory, the average velocity increase in the slipstream is given by Equation 6.6. Given that the inflow velocity behind the slipstream is given by  $(1+a)V_\infty$  (assuming the wing is positioned closely to the propeller, the slipstream velocity increases to  $(1+2a)V_\infty$  far away), the wing friction drag can be calculated according to Equation 6.7.

$$a = \frac{1}{2} \left( \sqrt{1 + \frac{8T}{\rho_\infty \pi D^2 V_\infty^2}} - 1 \right) \quad (6.6) \quad C_{D,f} = \frac{1}{S} \left( \iint^{S_{sl}} c_f \frac{V_j^2}{V_\infty^2} dS + \frac{1}{S} \iint^{S_{osl}} c_f dS \right) \quad (6.7)$$

Assuming a constant skin friction coefficient and slipstream velocity, this reduces to Equation 6.8. In the case of a wing without propeller, it can be simplified further to Equation 6.9. Using this equation, the average skin friction coefficient for the unpowered aircraft is calculated. Given that the wetted area is  $159.7m^2$ , the skin friction coefficient equals 0.00275. The wetted area inside the slipstream equals  $65.24m^2$ . Plugging this into Equation 6.8 yields an estimate for the skin friction drag of 147 counts for the propeller-powered strut-braced wing.

$$C_{D,f} = \frac{c_f}{S} (S_{sl}(1+a)^2 + S_{nsl}) \quad (6.8) \quad C_{D,f} = \frac{S_w}{S} c_f \quad (6.9)$$

This is somewhat lower than the value of 148 counts found using CFD. The estimated increase in skin friction drag is 3 counts, compared to an increase of 4 predicted by CFD. This is an underestimation by 25%, indicating the increase in skin friction drag is not linearly proportional to the increase in slipstream velocity predicted by actuator disk theory. There are multiple possible causes for this. First, the presence of separation violates the assumption of a constant skin friction coefficient. Second, the velocity in the slipstream does not increase uniformly. Since the skin friction drag increase is proportional to the square of the velocity, the average velocity increase obtained using actuator disk theory introduces another error. Finally, the slipstream development was ignored. Normally, the velocity increases from  $(1+a)V_\infty$  to  $(1+2a)V_\infty$  far away in the propeller slipstream. The velocity at the wing should be something in between the two.

### 6.3. COMPRESSIBLE EFFECTS

Initially, there was some concern with respect to local supersonic flow and shock waves. These could cause flow separation, and increase the drag. Even though the aircraft flies at a relatively low Mach number of 0.42, the flow is accelerated in the propeller slipstream. Furthermore, interference between the different elements of a strut-braced wing can locally lead to high supervelocities. Indeed, when comparing the propeller-on and -off case in Figure 6.15, there are several regions where the local Mach number is increased by the propeller. The increase in Mach number due to the propeller itself is limited. According to actuator disk theory, the average Mach number in the slipstream would be 0.431. In reality, the velocity inside the slipstream reaches higher values. This happens because the flow also has to move around the different wing elements, which may interfere with each other. Furthermore, the propeller swirl velocity locally alters the angle of attack, leading to higher supervelocities. Finally, an actuator disk gives a uniform slipstream velocity. In reality, there is significant variation in slipstream velocity behind the blade in radial direction.

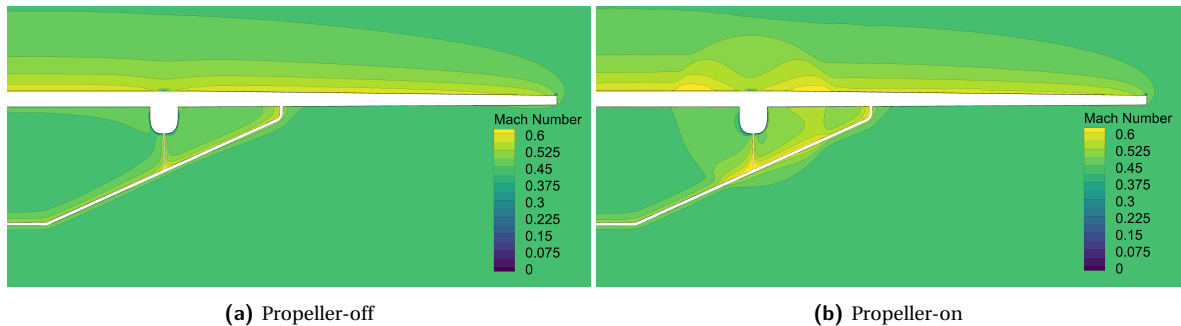


Figure 6.15: Mach contours at a section located at the quarter chord point of the wing.

There are several regions where the propeller slipstream causes high supervelocities. First, on the suction

side of the wing there are two peaks. Since they are present behind both the upgoing and downgoing blades, they are not only caused by the swirl velocity. Supercritical velocities induced by the wing thickness may be a contributing factor. Second, interference between the strut, wing and the propeller slipstream velocity leads to high supercritical velocities near the strut-wing junction, behind the outer part of the propeller disk. If the propeller was spaced more outboard, this may have led to even higher supercritical velocities in the strut-wing junction itself. Finally, the largest increase in Mach number is present at the strut-jury strut connection. The largest change is inboard of the jury strut. Initially, it was expected that the outboard part would be most vulnerable, due to the sharp angle between the strut and jury strut. However, the loading of the strut, caused by the propeller swirl velocity led to high supercritical velocities on the inboard part of the jury. Indeed, a small pocket of supersonic flow was detected at the inboard part of the jury strut, shown in Figure 6.16 (this is a front view of the region highlighted in Figure 6.11). The size of the pocket based on the time-averaged Mach number is relatively small. Along the jury strut, some slices were made to compare  $C_p$  plots, based on the mean flow. On all sections, a sharp pressure peak is present at the leading edge. Only for the section closest to the wall, the critical  $C_p$  is exceeded. Depending on the flight speed and the propeller setting, the pressure peak could increase in size, and possibly result in a shock wave and separation. Carefully shaping the airfoil of the jury strut could reduce the pressure peak, and make it more resistant to supersonic flow.

To avoid separation on the outboard part of the jury strut, as observed in subsection 6.2.1, one might be tempted to put it at a right angle with respect to the strut. This was also recommended by Tétrault et al. [51]. However, in the presence of a propeller this would only increase the supercritical velocities inboard of the jury strut. There must be an optimal strut angle that minimises interference drag.

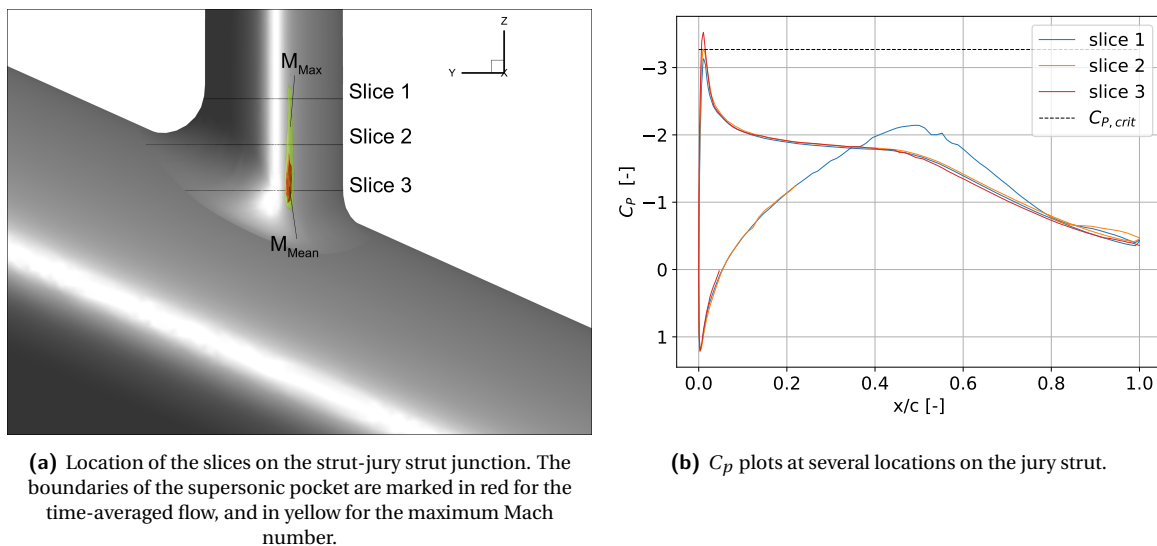


Figure 6.16:  $C_p$  plots and local supersonic flow on the jury strut.

The flowfields shown until now were averaged over time. A propeller induces unsteady loading, which may lead to even higher supercritical velocities. When looking at the maximum Mach number reached during 60 degrees of propeller rotation in Figure 6.16a, the area of supersonic flow grows by a factor of roughly three. Note that this is the maximum mach number of each cell separately. It is possible that not all these cells reach  $M > 1$  simultaneously. For the strut-jury strut junction, the effect of unsteadiness is limited. This is because it is not located behind the tip vortices of the propellers. The large gradients behind the propeller tip vortices cause unsteady oscillations with a large magnitude. This is illustrated in Figure 6.17, where the root mean square (RMS) of the oscillations in Mach number are shown. The iso-surfaces are drawn at an RMS value of 0.02. The oscillations in local Mach number are indeed the largest behind the propeller tip vortices. Downstream of the propeller, the amplitude of the oscillations dies out due to diffusion. Where the propeller tip vortices impinge on the wing and strut leading edge, the presence of the iso-surfaces indicates unsteady flow where the RMS of the Mach number exceeds 0.02. However, no supersonic flow in these regions was found. The strut-jury strut junction is not inside any iso-surface, meaning that the RMS of the Mach number is below 0.02 in that location.

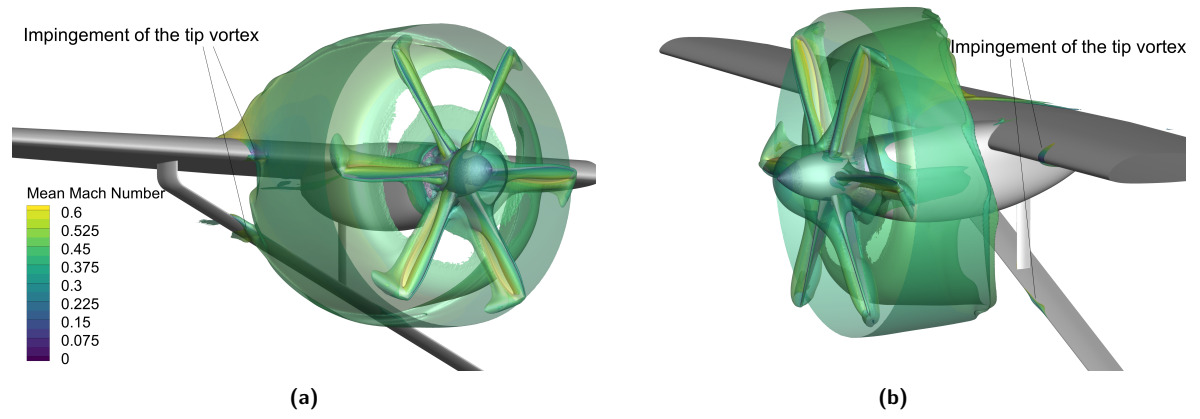


Figure 6.17: Iso-surfaces of the root mean square of the oscillations in Mach number, at a value of 0.02. The iso-surfaces are colored with the mean Mach number.

# 7

## RECOMMENDATIONS AND CONCLUSION

Based on the results of this work, some recommendations to future researchers are given in [section 7.1](#). These highlight parts of this report that may benefit from more detailed consideration, and gives ideas on which further work could be based. The report is wrapped up with the conclusion in [section 7.2](#), where the main findings are summarised.

### 7.1. RECOMMENDATIONS

In future work, there are some areas of that could be improved, or build upon. First, it was already mentioned that the configurations used here were not optimised. This likely resulted in conservative estimates for the induced drag, both with and without propeller. To get an idea of how great the advantage of propeller-powered strut-braced wings can be, the next step would be to optimise for induced drag. This only depends on the loading distribution, so it can be done using a lower fidelity method like VLM or lifting-line theory. Of course, this would also improve the performance of the conventional wing, so the advantage in induced drag for the strut-braced wing might either increase or decrease.

The strut-jury strut junction proved an area with complex flow behaviour. Junction flow with separation at multiple locations, combined with a propeller slipstream leading to local transonic speeds make it interesting for further study. RANS is not very suitable for this kind of flows, because of its difficulty in predicting corner flows. Investigating this region with a higher fidelity method such as LES might shed more light on the phenomena that are at play. Varying the junction geometry by using different (jury) strut airfoils, changing the angle of the jury strut and adding fillets may give clues on how to reduce losses in this area.

Finally, the advantage of a propeller-powered strut-braced wing has been proven for an arbitrary research aircraft. The analysis methodology could now be applied to the design of a real strut-braced wing. The fuel-burn of this aircraft could be compared with the ATR72 to quantify the advantage of a more representative strut-braced wing. This has been done with the help of actuator disk theory by Zinjarde [62], but he found gains in induced drag lower than those in this report. It would be interesting to see how his results hold with a higher fidelity method.

### 7.2. CONCLUSION

This thesis report delved into the aerodynamic performance of a propeller-powered strut-braced wing. It was expected that the integration of a propeller would lead to savings in induced drag larger than those in conventional aircraft. This is mainly because a strut-braced wing has additional lifting surfaces that could recover more swirl from the propeller slipstream. While the expectation was a reduction in induced drag, it is important to verify that this is not offset by an increase in other drag components. For this reason, the effect of the propeller on viscous and compressible aerodynamics were also considered. The treatment of viscous effects was split up into a part about flow separation and another about friction drag. For compressibility, the goal was to verify whether interference between the different wing elements would not lead to local supersonic flow under the influence of a propeller.

Induced drag was investigated using a panel method called Flightstream. Because of the complexity of a SBW aircraft, Flightstream was first validated with CFD using a simplified configuration, representing a propeller mounted above a strut. It was found that this configuration accurately matched the lift and drag distributions predicted by CFD. Next, the full strut-braced wing aircraft, including jury strut was validated. In this case, agreement was very good for the aircraft without propeller, but lost some accuracy when adding propeller effects. These are mostly because Flightstream failed to capture some pressure peaks. Still, it was able to capture trends in the lift and drag distributions well, so it was concluded that a panel method is suitable for problems of this kind.

For the induced drag, first the effect of the propeller on the lift and induced drag of three configurations was considered. These configurations were a conventional wing and a strut-braced wing, one with and one without jury strut. The main effect of the strut was to reduce the lift on the main wing, both in propeller-on and -off cases. Still, combined with the lift on the strut, the strut-braced wing configurations experienced a roughly 4% larger lift than the CW wing at the same angle of attack. The jury strut had a negligible influence on it. When correcting the lift to a constant value, the two strut-braced wing configurations had a slightly lower induced drag (39.2 cts and 39.5 cts with and without jury) than the conventional wing (40.1 cts). Next, the effect of the main strut and jury on the change in induced drag of the propeller was calculated. At constant lift, it was found that the main strut increases the reduction in induced drag caused by the propeller, by 2.3 counts. This is mainly caused by a reduction of induced drag of the jury, and to some extent because it favorably interfered with the wing. For the jury strut, the results were more surprising. Initially it was thought that it would act as a swirl recovery vane, and thus lead to additional savings in induced drag. While the jury itself experienced a thrust component of 0.2 cts under the influence of the propeller, it caused an increase in drag on the wing large enough to cancel out its own thrust. In total, it reduced the gain in induced drag caused by the propeller by 0.8 cts. Of the three configurations that were investigated, the two strut-braced wings had the lowest induced drag when considering propeller effects. The results above were obtained using unoptimised wings. Optimising the loading distributions could for example reduce the unfavorable interference between jury strut and wing.

Flow separation was observed at all junction locations, mainly at the leading edge of intersecting wing elements. The report focused on two locations relevant for a strut-braced wing, namely the strut-wing junction and strut-jury strut junction. The strut-wing junction only showed separation at the strut leading edge, followed by a roll-up of the separated flow into a horse-shoe vortex wrapping around the strut. This flow behaviour was not influenced by the presence of a propeller. The strut-jury strut junction also exhibited leading edge separation, in addition to corner separation at the trailing edge of the jury strut, and separation at the trailing edge of the main strut. The size of the corner separation reduced under the influence of the propeller, mainly because its swirl velocity reduced the pressure gradients on the outboard surface of the jury strut. At the trailing edge of the strut, the separation was influenced by the location of the horse-shoe vortex system and the pressure gradient on the strut. A large adverse pressure gradient caused by the propeller inboard of the jury strut caused separation there. On the outboard region, no difference in pressure gradient was observed. Instead, it seemed as if the presence of the horse-shoe vortex caused a region of separated flow. However, due to the relatively coarse mesh in the region, and the inability of RANS to accurately simulate junction flows no definite conclusions about this regions could be made. In addition, it was verified whether the propeller slipstream would change the boundary layer behaviour, by locally increasing the Reynolds number there. This was not the case, the shape factor of the boundary layer was similar for the prop-on and -off cases, outside of the horseshoe vortex system.

The propeller was observed to increase the friction drag only inside the slipstream, proportional to the local slipstream velocity. The change in friction was in the order of 3%, making it insignificant compared to the savings in induced drag. The increase in friction could to some extent be predicted based on the average skin friction coefficient of the unpowered aircraft and using actuator disk theory to calculate the slipstream velocity. However, this method underestimated the increase in friction drag by 1 count.

Supercritical velocities were increased by the propeller, partially because of the increased slipstream velocity, but also because of a change in angle of attack caused by the swirl velocity. In the propeller-on case, the largest supercritical velocities were found on the inboard part of the strut-jury strut junction. This is somewhat surprising, as the sharpest angle between the two elements is on the outboard. However, the angle of attack induced by the swirl velocity induced large peaks in velocity inboard. Near the leading edge of the jury strut, these reached supersonic speeds. The size of the supersonic pocket was very small, and can probably be avoided by

slightly changing the geometry of the junction. Unsteadiness of the aerodynamic flow slightly increased the size of the supersonic pocket. However, the most significant effect of unsteadiness was behind the propeller tip vortices, where the large velocity gradients caused oscillations in Mach number larger than 0.02. This illustrates the need to consider compressible and to a smaller extent unsteady effect. Still, it is expected that a different junction location or design could have avoided the small supersonic region.

In this report, it has been shown that strut-braced wings are more efficient at recovering swirl from a propeller slipstream, compared to a conventional wing with propeller. They thus have the potential of additional savings in induced drag, on top of the lower induced drag caused by their larger aspect ratio wings. Potential increases in friction and interference drag have been shown to be small. Based on the results of this work, strut-braced wing aircraft could be interesting for the next generation of regional turboprops.



# BIBLIOGRAPHY

- [1] Vivek Ahuja and Roy J. Hartfield. “Predicting the aero loads behind a propeller in the presence of a wing using flightstream™”. In: *15th AIAA Aviation Technology, Integration, and Operations Conference*. Dallas, Texas, June 2015. DOI: [10.2514/6.2015-2734](https://doi.org/10.2514/6.2015-2734). URL: <https://arc.aiaa.org/doi/10.2514/6.2015-2734>.
- [2] Vivek Ahuja, Roy J. Hartfield, and Danilo Ciliberti. “Three-dimensional Viscous Coupling and Flow Separation Enhancements to an Inviscid Surface Vorticity Flow Solver”. In: *AIAA Scitech 2023 Forum*. National Harbor, Maryland, Jan. 2023. DOI: [10.2514/6.2023-2455](https://doi.org/10.2514/6.2023-2455).
- [3] Vivek Ahuja and Brandon L. Litherland. “Comparison of Aerodynamic Analysis Tools Applied to a Propeller-Blown Wing”. In: *AIAA Scitech 2023 Forum*. National Harbor: AIAA, Jan. 2023. DOI: [10.2514/6.2023-1753](https://doi.org/10.2514/6.2023-1753).
- [4] F. Avallone et al. “Aerodynamic and aeroacoustic effects of swirl recovery vanes length”. In: *Journal of Aircraft* 56.6 (2019), pp. 2223–2235. ISSN: 15333868. DOI: [10.2514/1.C035552](https://doi.org/10.2514/1.C035552).
- [5] TJ Barber. “An investigation of strut-wall intersection losses”. In: *16th Aerospace Sciences Meeting*. Huntsville, Alabama: American Institute of Aeronautics and Astronautics (AIAA), 1978. DOI: [10.2514/6.1978-205](https://doi.org/10.2514/6.1978-205). URL: <http://arc.aiaa.org>.
- [6] John V. Becker. *Boundary-Layer Transition on the N.A.C.A. 0012 and 23012 Airfoils in the 8-Foot High-Speed Wind Tunnel, Special Report*. Tech. rep. Langley: NACA, 1940.
- [7] Luciano Castillo, Xia Wang, and William K. George. “Separation criterion for turbulent boundary layers via similarity analysis”. In: *Journal of Fluids Engineering, Transactions of the ASME* 126.3 (May 2004), pp. 297–304. ISSN: 00982202. DOI: [10.1115/1.1758262](https://doi.org/10.1115/1.1758262). URL: <https://dx.doi.org/10.1115/1.1758262>.
- [8] F. M. Catalano. “On the Effects of an Installed Propeller Slipstream on Wing Aerodynamic Characteristics”. In: *Acta Polytechnica* 44.3 (2004). ISSN: 1210-2709. DOI: [10.14311/562](https://doi.org/10.14311/562).
- [9] Shamsheer S. Chauhan and Joaquim R. R. A. Martins. “RANS-Based Aerodynamic Shape Optimization of a Wing Considering Propeller–Wing Interaction”. In: 58.3 (2021), pp. 497–513. DOI: [10.2514/1.C035991](https://doi.org/10.2514/1.C035991). URL: <https://doi.org/10.2514/1.C035991>.
- [10] John T. Conway. “Analytical solutions for the actuator disk with variable radial distribution of load”. In: *Journal of Fluid Mechanics* 297 (1995), pp. 327–355. ISSN: 14697645. DOI: [10.1017/S0022112095003120](https://doi.org/10.1017/S0022112095003120).
- [11] Luciano Demasi et al. “Minimum induced drag conditions for truss-braced wings”. In: *AIAA Journal* 56.12 (2018), pp. 4669–4684. ISSN: 00011452. DOI: [10.2514/1.J057225](https://doi.org/10.2514/1.J057225).
- [12] Christopher K Droney et al. *Subsonic Ultra Green Aircraft Research: Phase III-Mach 0.75 Transonic Truss-Braced Wing Design*. Tech. rep. CR-20205005698. Hampton: NASA, 2020. URL: <https://ntrs.nasa.gov/citations/20205005698>.
- [13] Frank A. Dvorak, Brian Maskew, and Frank A. Woodward. *Investigation of Three-Dimensional Flow Separation on Fuselage Configurations*. Tech. rep. USAAMRDL-TR-77-4. Bellevue, Washington: Analytical methods, Inc., 1977.
- [14] Luis Eca et al. “The Pros and Cons of Wall Functions”. In: *Proceedings of the ASME 2015 34th International Conference on Ocean, Offshore and Arctic Engineering*. Vol. 2. St John’s, Newfoundland: American Society of Mechanical Engineers, 2015.
- [15] L. Eça and M Hoekstra. “Discretization Uncertainty Estimation based on a Least Squares version of the Grid Convergence Index”. In: *Proceedings of the Second Workshop on CFD Uncertainty Analysis*. Lisbon, Oct. 2006.
- [16] Eurocontrol. *Data Snapshot on CO<sub>2</sub> emissions and flight distance*. 2021. URL: <https://www.eurocontrol.int/publication/eurocontrol-data-snapshot-co2-emissions-flight-distance> (visited on 06/13/2022).

- [17] Fabien Gand et al. "Flow dynamics past a simplified wing body junction". In: *Physics of Fluids* 22 (Nov. 2010). ISSN: 10706631. DOI: [10.1063/1.3500697](https://doi.org/10.1063/1.3500697).
- [18] Falk Goetten et al. "A review of guidelines and best practices for subsonic aerodynamic simulations using RANS CFD". In: *11th Asia-Pacific International Symposium of Aerospace Technology* (Dec. 2019), pp. 227–245.
- [19] John F. Gundlach IV et al. "Conceptual design studies of a strut-braced wing transonic transport". In: *Journal of Aircraft* 37.6 (2000), pp. 976–983. ISSN: 00218669. DOI: [10.2514/2.2724](https://doi.org/10.2514/2.2724).
- [20] J L Hess. "Panel Methods in computational fluid dynamics". In: *Annual Rev. Fluid Mech*, 22.1 (1990), pp. 255–274. DOI: <https://doi.org/10.1146/annurev.fl.22.010190.001351>.
- [21] J.L. Hess. *A fully automatic combined potential-flow boundary-layer procedure for calculating viscous effects on the lifts and pressure distributions of arbitrary three-dimensional configurations*. Tech. rep. MDC J7491. Long Beach, California: Douglas aircraft company, Aug. 1977.
- [22] Robert T. Johnson, David P. Witkowski, and John P. Sullivan. "Experimental results of a propeller/wing interaction study". In: *Journal of Aerospace* 100 (1991), pp. 121–130. ISSN: 26883627. DOI: [10.4271/910998](https://doi.org/10.4271/910998). URL: <https://www.jstor.org/stable/44547585>.
- [23] R. T. Johnston and J. P. Sullivan. "Unsteady Wing Surface Pressures in the Wake of a Propeller". In: *30th aerospace Sciences Meeting and Exhibit*. Reno, Nevada, Jan. 1992. DOI: [10.2514/6.1992-277](https://doi.org/10.2514/6.1992-277).
- [24] Michael A. Kegerise et al. *An experimental investigation of a wing-fuselage junction model in the nasa langley 14-by 22-foot subsonic wind tunnel*. Tech. rep. NASA/TM–2019–220286. Langley, Virginia, June 2019. DOI: [10.2514/6.2019-0077](https://doi.org/10.2514/6.2019-0077).
- [25] Andy Ko, William H. Mason, and Bernard Grossman. "Transonic aerodynamics of a wing/pylon/strut juncture". In: Orlando, Florida: American Institute of Aeronautics and Astronautics Inc., June 2003. ISBN: 9781624100925. DOI: [10.2514/6.2003-4062](https://doi.org/10.2514/6.2003-4062). URL: <https://arc-aiaa-org.tudelft.idm.oclc.org/doi/abs/10.2514/6.2003-4062>.
- [26] Ilan Kroo. "Drag due to lift: Concepts for Prediction". In: *Annual Review of Fluid Mechanics* 33 (2001), pp. 587–617. DOI: <https://doi.org/10.1146/annurev.fluid.33.1.587>.
- [27] Ilan Kroo. "Propeller-Wing Integration for Minimum Induced Loss." In: *Journal of Aircraft* 23.7 (1986), pp. 561–565. ISSN: 00218669. DOI: [10.2514/3.45344](https://doi.org/10.2514/3.45344).
- [28] Qingxi Li et al. "Numerical investigation of configurations with optimum swirl recovery for propeller propulsion systems". In: *AIAA Journal* 57 (2019), pp. 1502–1513. ISSN: 00011452. DOI: [10.2514/1.J057704](https://doi.org/10.2514/1.J057704).
- [29] Yiyuan Ma, Stanislav Karpuk, and Ali Elham. "Conceptual design and comparative study of strut-braced wing and twin-fuselage aircraft configurations with ultra-high aspect ratio wings". In: *Aerospace Science and Technology* 121 (2022). ISSN: 12709638. DOI: [10.1016/j.ast.2022.107395](https://doi.org/10.1016/j.ast.2022.107395). URL: <https://doi.org/10.1016/j.ast.2022.107395>.
- [30] M. Maughmer et al. "Experimental investigation of wing/fuselage integration geometries". In: *Journal of Aircraft* 26.8 (1989), pp. 705–711. ISSN: 00218669. DOI: [10.2514/3.45828](https://doi.org/10.2514/3.45828).
- [31] Stan J. Miley, Richard M. Howard, and Bruce J. Holmes. "Wing laminar boundary layer in the presence of a propeller slipstream". In: *Journal of aircraft* 25.7 (May 1988), pp. 606–611. ISSN: 00218669. DOI: [10.2514/3.45630](https://doi.org/10.2514/3.45630). URL: <https://arc.aiaa.org/doi/abs/10.2514/3.45630>.
- [32] J. Morgado et al. "XFOIL vs CFD performance predictions for high lift low Reynolds number airfoils". In: *Aerospace Science and Technology* 52 (May 2016), pp. 207–214. ISSN: 1270-9638. DOI: [10.1016/J.AST.2016.02.031](https://doi.org/10.1016/J.AST.2016.02.031).
- [33] B. Oskam. "Asymptotic convergence of higher-order accurate panel methods". In: *Journal of Aircraft* 23.2 (1986), pp. 126–130. ISSN: 00218669. DOI: [10.2514/3.45278](https://doi.org/10.2514/3.45278). URL: <https://arc.aiaa.org/doi/10.2514/3.45278>.
- [34] P. H. Park. *The effect on block fuel consumption of a strutted versus cantileverwing for a short-haul transport including strut aeroelastic considerations*. Tech. rep. 78-1454. Seattle, Washington: Boeing, 1978. DOI: [10.2514/6.1978-1454](https://doi.org/10.2514/6.1978-1454).

- [35] L. Prandtl. "7. Bericht über Untersuchungen zur ausgebildeten Turbulenz". In: *Zeitschrift für Angewandte Mathematik und Mechanik* 5.2 (Jan. 1925), pp. 136–139. ISSN: 0044-2267. DOI: [10.1002/zamm.19250050212](https://doi.org/10.1002/zamm.19250050212).
- [36] M. H. Rizk. "Propeller Slipstream/Wing Interaction in the Transonic Regime." In: *AIAA 18th Aerospace Sciences Meeting*. Pasadena, California, Jan. 1980. DOI: [10.2514/6.1980-125](https://doi.org/10.2514/6.1980-125).
- [37] P J Roache. "Quantification of Uncertainty in Computational Fluid Dynamics". In: *Annual Review of Fluid Mechanics* 29 (Jan. 1997), pp. 123–160. DOI: <https://doi.org/10.1146/annurev.fluid.29.1.123>.
- [38] Ma Rong, Zhong Bo Wen, and Liu Pei Qing. "Optimization design study of low-Reynolds-number high-lift airfoils for the high-efficiency propeller of low-dynamic vehicles in stratosphere". In: *Science China Technological Sciences* 53.10 (2010), pp. 2792–2807. ISSN: 18691900. DOI: [10.1007/s11431-010-4087-0](https://doi.org/10.1007/s11431-010-4087-0).
- [39] Ney R. Secco and Joaquim R.R.A. Martins. "RANS-based aerodynamic shape optimization of a strut-braced wing with overset meshes". In: *Journal of Aircraft* 56.1 (Sept. 2019), pp. 217–227. ISSN: 15333868. DOI: [10.2514/1.C034934](https://doi.org/10.2514/1.C034934).
- [40] T. Sinnige et al. "Aerodynamic and aeroacoustic performance of a propeller propulsion system with swirl-recovery vanes". In: *Journal of Propulsion and Power* 34.6 (2018), pp. 1376–1390. ISSN: 15333876. DOI: [10.2514/1.B36877](https://doi.org/10.2514/1.B36877).
- [41] T. Sinnige et al. "Wingtip-mounted propellers: Aerodynamic analysis of interaction effects and comparison with conventional layout". In: *Journal of Aircraft* 56.1 (Nov. 2019), pp. 295–312. ISSN: 15333868. DOI: [10.2514/1.C034978](https://doi.org/10.2514/1.C034978).
- [42] Stephen C. Smith and Ilan M. Kroo. "Computation of induced drag for elliptical and crescent-shaped wings". In: *Journal of Aircraft* 30.4 (May 1993), pp. 446–452. ISSN: 00218669. DOI: [10.2514/3.46365](https://doi.org/10.2514/3.46365).
- [43] P. R. Spalart and Allmaras S.R. "A one-equation turbulence model for aerodynamic flows". In: *AIAA 30th Aerospace Sciences Meeting and Exhibit*. 1. Reno, Nevada, 1994, pp. 5–21. DOI: [10.2514/6.1992-439](https://doi.org/10.2514/6.1992-439).
- [44] A. Stanbrook. *Experimental Observation of Vortices in Wing-Body Junctions*. Tech. rep. 3114. London: Aeronautical Research Council, Mar. 1957. URL: <https://reports.aerade.cranfield.ac.uk/handle/1826.2/3683>.
- [45] N.M Standen. *Calculation of integral parameters of a compressible turbulent boundary layer using a concept of mass entrainment*. Tech. rep. 64-14. Montreal: McGill University, 1964.
- [46] W. Stender. *Hurel-Dubois Cargo Projects*. Apr. 1956. URL: <https://airandspace.si.edu/collection-archive-item/aircraft-hurel-dubois-hd31-hd32-hd34-hd54/sova-nasm-1993-0055-ref1237>.
- [47] T. C. A. Stokkermans and L. L. M. Veldhuis. "Propeller Performance at Large Angle of Attack Applicable to Compound Helicopters". In: *AIAA Journal* 59.6 (2021), pp. 2183–2199. ISSN: 0001-1452. DOI: [10.2514/1.J059509](https://doi.org/10.2514/1.J059509).
- [48] T. C.A. Stokkermans et al. "Validation and comparison of RANS propeller modeling methods for tip-mounted applications". In: *AIAA Journal* 57.2 (2019), pp. 566–580. ISSN: 00011452. DOI: [10.2514/1.J057398](https://doi.org/10.2514/1.J057398).
- [49] B. S. Stratford. "The prediction of separation of the turbulent boundary layer". In: *Journal of Fluid Mechanics* 5.1 (1959), pp. 1–16. DOI: [10.1017/S0022112059000015](https://doi.org/10.1017/S0022112059000015).
- [50] Timothy Takahashi and Shane Donovan. "Non Planar Span Loads for Minimum Induced Drag". In: *49th AIAA Aerospace Sciences Meeting including the New Horizons Forum and Aerospace Exposition*. AIAA. Orlando, Florida, Jan. 2011.
- [51] Philippe-Andre Tetrault, Joseph A. Schetz, and Bernard Grossman. "Numerical prediction of interference drag of strut-surface intersection in transonic flow". In: *AIAA Journal* 39.5 (2001), pp. 857–864. ISSN: 0001-1452. DOI: [10.2514/3.14812](https://doi.org/10.2514/3.14812).
- [52] B. Thwaites. "Approximate Calculation of the Laminar Boundary Layer". In: *The aeronautical Quarterly* 1.3 (1949), pp. 145–280. DOI: <https://doi.org/10.1017/S0001925900000184>.

- [53] M. C. Towne et al. "PAN AIR modeling studies". In: *AIAA Applied Aerodynamics Conference*. Danvers, Massachusetts: American Institute of Aeronautics and Astronautics (AIAA), July 1983. DOI: [10.2514/6.1983-1830](https://doi.org/10.2514/6.1983-1830). URL: <http://arc.aiaa.org>.
- [54] W Valarezo. "Calculation of isolated and installed multiple rotor flows using a surface panel method". In: *AIAA 7th Applied Aerodynamics Conference*. Seattle, Washington: American Institute of Aeronautics and Astronautics, 1989. DOI: <https://doi.org/10.2514/3.46054>.
- [55] L.L.M. Veldhuis. "Optimization of tractor propeller/wing configurations". In: *Proceedings of the Institution of Mechanical Engineers* 209 (3 1995), pp. 215–226. DOI: [https://doi.org/10.1243/PIME\\_PROC\\_1995\\_209\\_292\\_02](https://doi.org/10.1243/PIME_PROC_1995_209_292_02).
- [56] L.L.M. Veldhuis. "Review of Propeller-Wing Aerodynamic Interference". In: *24th International Congress of the Aeronautical Sciences*. Yokohama, Japan, 2004.
- [57] L.L.M. Veldhuis et al. "Analysis of swirl recovery vanes for increased propulsive efficiency in tractor propeller aircraft". In: *30th Congress of the International Council of the Aeronautical Sciences, ICAS 2016* (2016).
- [58] Roelof Vos and Saeed Farokhi. *Introduction to Transonic Aerodynamics*. Vol. 110. Springer, 2015. ISBN: 9401797463. URL: <https://link.springer.com/book/10.1007/978-94-017-9747-4>.
- [59] H. B. Wang et al. "Influence analysis of propeller location parameters on wings using a panel/viscous vortex particle hybrid method". In: *Aeronautical Journal* 122.1247 (2018), pp. 21–41. ISSN: 00019240. DOI: [10.1017/aer.2017.109](https://doi.org/10.1017/aer.2017.109).
- [60] Dave P Witkowski, Alex K. H. Lee, and John P Sullivan. "Aerodynamic Interaction Between Propellers and Wings". In: *Journal of Aircraft* 29.9 (Sept. 1989), pp. 829–836. DOI: <https://doi.org/10.2514/3.45848>.
- [61] Zhi Yang, Andrew C. Kirby, and Dimitri J. Mavriplis. "Comparison of Propeller-Wing Interaction Simulation using Different Levels of Fidelity". In: *AIAA SciTech Forum 2022*. San Diego, California, 2022. ISBN: 9781624106316. DOI: <https://doi.org/10.2514/6.2022-1678>.
- [62] Pranav Zinjarde. *Aerodynamic Design Integration of Strut Braced Wings Aerodynamic Design Integration of Strut Braced Wings*. Tech. rep. Delft, the Netherlands: Delft University of Technology, 2023, p. 88. URL: <http://resolver.tudelft.nl/uuid:b7b28c9c-6da8-42e3-90ce-99e4d524f1f0>.